Neutron scattering studies of materials near the magnetic phase transition

Warren, Paul

Neutron Scattering Studies of Materials Near the Magnetic Phase Transition

Paul Warren

Ph.D. Thesis, University of Durham, September 1990,

Abstract

Metals on the verge or just in the weakly magnetic state offer a unique testing ground for current theories of itinerant magnetism.

Three investigations of such systems using neutron scattering are outlined in this work.

$TiBe_2$ is of interest since the random substitution of copper at Be atom sites expands the lattice allowing one to cross the threshold from an incipient to a weakly magnetic state. Small angle neutron scattering studies of spin density fluctuations in $TiBe_{1.5}Cu_{0.5}$ have shown that a single phenomonological model is sufficient to describe the collected integrated intensities above and below the magnetic phase transition temperature. Observations below the transition temperature may be attributed to scattering from damped spin waves.

Polarised neutron diffraction studies of a single crystal of $ZrFe_2$ are in contradiction with reported band structure calculations of a strong ferrimagnetic ground state. The magnetic distribution in real space around the Fe ions is highly spherical and the form factor closely follows that of free Fe ions in reciprocal space.

A small angle neutron scattering investigation of the helical spin wave density wave in MnSi below the magnetic phase transition and spin density fluctuations in the paramagnetic regime under hydrostatic pressure has been performed.

Preface

The work detailed in this thesis was carried out at the Department of Physics at the University of Durham and at the Institut Laue Langevin, Grenoble in France. The substance of the thesis is entirely original except where specified and has not been submitted for any other degree, diploma or other qualification.

Many people have been of invaluable help during the period of work. I would like to give special thanks to my supervisor Nick Bernhoeft for his assistance and contagious enthusiasm for the subject.

The small angle neutron scattering experiments reported in this work have been performed in association with Don McKenzie Paul of the University of Warwick and Liz Lindley formally of the I.L.L., a thankyou goes to both for introducing me to the ways of experimental neutron scattering.

I should like to thank Bruce Forsyth of the Rutherford Appleton Laboratories and Gary McIntre formerly of the I.L.L. for their expertise and help in unravelling the complexities of polarised neutron diffraction and their assistance with the data analysis of chapter 7.

A special thanks goes to Sarah Thompson for her assistance, expertise and insomnia, without whom the bulk magnet measurements

may never have been taken.

Further I would like to thank the technical staff of the University of Durham for their skill in production of the cold crucible crystal grower.

Finally acknowledgement goes to fellow students and postdoctors with whom many invaluable discussions have been had: Martin Delap, James Allen, Simon Cockerton, Stephen Hayden, Sarah Thompson and David Lambrick.

Contents

CHAPTER 1

Introduction

This thesis contains experimental details of three different neutron scattering investigations. The first gives measurements of the magnetic scattering spectrum of an alloy upon $TiBe_2$ with small amounts of copper substituted at beryllium sites. The second experiment has been designed to shed light on the dispute over the magnetic nature of the binary alloy $ZrFe_2$ using polarised neutron diffraction investigations to ascertain its magnetic moment distribution in real space. For this purpose single crystals of $ZrFe_2$ have been prepared using a specially designed and built cold crucible rig with radio frequency induction heating. The third experiment was a small angle neutron scattering study of the helical magnetic system MnSi. A high quality polycrystalline sample was grown from the melt to investigate the renormalisation of its dynamical magnetic properties with the variation of pressure.

The studied materials are thought to lie within the category of itinerant ferrromagnets. That is the electrons with which the magnetic moments of the systems are associated are free to move within the crystals of the material. This behaviour stems from the 3d transition metal nature of the bandstructure.

Magnetism occurs in many elements and compounds. A general description of the mechanism, on a microscopic scale, that causes magnetism must be based upon the quantum mechanical nature of the systems. The moment associated with an electron may arise from two distinct sources, the angular momentum of the electron due to its spin and that occurring from its motion around the nucleus. In systems whose magnetism may be associated with the electrons of the 3d shell the orbital angular momentum is normally to a large extent quenched.

Bulk magnetism arises from an inbalance in the number of up and down spins of electrons described by the magnetic quantum number. Through Hund's rules it is clear that only unpaired electrons may contribute. In ionic crystals where the valence electrons are all paired no magnetic ordering can occur.

In metals any resulting magnetic ordering is associated with either the conduction electrons or deep lying unpaired electrons. The 3d energy levels of the transition elements lie at the Fermi surface allowing electrons to move freely through the metal. However it is a requirement of 3d metal itinerant magnetism that these electrons, that all posses the same spin on an atomic level, remain closely associated with the atom of origin. In the extreme case of an electron gas it has been shown in an early calculation that ferromagnetism cannot exist[1].

The magnetism of the transition elements and their alloys is in complete contrast to that of the rare earth alloys and their

alloys. In an insulator the unpaired electrons lie well below the conduction band and the resulting magnetic ordering originates from the unpaired electrons in atomic orbitals. The unpaired electrons in the 4f shell of rare earth elements that result in magnetic ordering lie in deep energy levels.

On an atomic level it is the requirement of quantum mechanics that any unpaired electrons should have the same spin number, implying the existence of local magnetic ordering even if the whole crystal has no resultant moment. The requirement of quantum mechanics infers the existence of the paramagnetic state in which a response may occur on a local level to align spins over more than a single atomic position.

If the material in its ground state shows magnetic ordering, in the absence of an external magnetic field, over a large number of atoms (the domain) the material is said to be either ferromagnetic, antiferromagnetic or ferrimagnetic depending upon the ordering exhibited.

1.1 The Theory of Magnetism

For many years the theory of magnetism has posed problems. Although there exist numerous empirical relationships to describe the bulk behaviour of magnetic materials no theory exists that can adequately describe the properties of all magnetic materials. This inability to produce an all encompassing theory stems from the many bodied nature and resulting complexity of interactions

within the systems.

Two complementary but contrasting lines of thought exist as to the origin of magnetic ordering. Whilst both have their origin in the realisation that magnetism stems from the repulsive coulomb interactions between electrons and the quantum mechanical requirements of the Pauli exclusion principle neither can claim to describe all but a few extreme systems. However they provide a physical insight into magnetic ordering mechanisms and an indication of the way forward.

1.2 The Heisenberg Model of Magnetism

The Heisenberg or localised model of magnetism describes the origin of magnetic ordering through interatomic exchange interactions which tend to align neighbouring electrons at atomic sites either parallel or antiparallel. These exchange interactions are dominant over the ordinary dipole interactions between spin moments.

The basic Heisenberg model can only describe an integral number of spins per atom whilst the moment is fixed in magnitude but is free to vary in orientation. It has been used with some success to describe magnetism in insulating materials and certain rare earth metals.

The existence of systems with non-integral spins per atom (i.e. transition metals and weak magnetic alloys $ZrZn_2$[2] and

$ScIn_3$[3]) has been approached theoretically by the generalised Heisenberg models of Horwitz[4] and Van Vleck[5] where spins are continually redistributed at different sites.

1.3 The Itinerant Theory of Magnetism

The itinerant model of magnetism is based upon the knowledge that conduction electrons are able to move within a metal crystal. In complete contrast to the Heisenberg model where electrons are localised in real space this approach preaches localisation in k space and is the origin of band models of magnetism.

The first major contribution to the field of itinerant magnetism was made by Stoner[6,7] and Slater[8]. Their independent work went beyond that of Bloch[9] who discussed the possible existence of ferromagnetism in an electron gas and Wigner[10] who showed that correlations between electrons in a electron gas act to suppress any magnetic ordering. Both Stoner and Slater models consider the effects of intra atomic interactions only in the limit of the tight binding model.

These models describe the effect of excitations of an electron above the Fermi surface to produce an electron hole pair. The interaction between electron spins of conduction electrons is simply replaced by an effective or mean field.

The major disadvantage of these simple models is their inability to reproduce the observed thermal properties. They fail

to predict the observed Curie Weiss behaviour of the magnetic susceptibility and the calculated Curie temperature T_c is in general far greater than that observed.

The importance of the interaction between the excited electrons and holes was first considered by Slater[11] in his theory of bound collective modes in ferromagnetic insulators. This was extended to ferromagnetic metals[12] and developed in terms of the dynamical Hartree-Fock approximation (or random phase approximation R.P.A.) by Herring[13]. The introduction of electron correlations results in the shift of the theoretical Stoner response to lower frequencies resulting in the appearance of collective spin wave modes at large wavelengths. At large wavevectors the collective excitations enter the single particle or Stoner continuum where they are damped.

The random phase approximation takes no account of the effect of the resulting spin fluctuations upon the Stoner equilibrium state and the theory again fails at finite temperatures.

The next step in the model of itinerant magnetism was made by Murato and Doniach[14] and further enhanced by Moriya and Kawabata[15]. By considering to first order the effects of finite q modes upon the equilibrium state in a self consistent manner they were able to predict both the Curie Weiss behaviour and a reduction in T_c from that calculated using R.P.A.. This theory is known as the self consistent renormalisation theory (S.C.R.).

The S.C.R. theory of Murato and Doniach considers the local magnetisation as a scalar quantity. This reduces the description of the fluctuations upon the system to those that vary in magnitude only that is to say longitudinal fluctuations This means that the effect of transverse fluctuations i.e. spin waves upon the renormalised state which are the major contribution to the ferromagnetic state were ignored.

This problem was surmounted in the theories of Moriya and Kawabata[15]. Both their modern theory and that of Lonzarich and Taillefer[16] initially consider the effects of both longitudinal and transverse fluctuations upon the system. The approach adopted by Moriya reduces the model below T_c to a self consistent calculation based upon transverse fluctuations only, whereas the Lonzarich description includes a longitudinal contribution in the equation of state. The Lonzarich model includes only leading terms to the transverse fluctuations and a natural temperature dependent cut off wavevector for thermally excited modes is used in an effort to account for the systems quantum dynamics.

1.4 Investigation Outline

The part of this thesis concentrating on the investigation of Cu induced ferromagnetism in $TiBe_2$, through the alloying of Cu, has been performed using small angle neutron scattering upon a polycrystalline sample over a broad temperature range spanning the magnetic phase transition. The addition of copper into the

lattice results in a transition from a paramagnetic to a ferromagnetic state. The purpose of this work is to show that a simple model based upon the adjustment of two independent microscopic parameters can be used to describe the observed behaviour.

In the second part of this work the magnetic structure of $ZrFe_2$ is under investigation. $ZrFe_2$ is thought to be an itinerant ferrimagnet. Using polarised neutron diffraction techniques its true nature has been established. For this purpose a single crystal of the material has been grown, thought to be the first of its kind. Investigations using polycrystalline samples have been and remain ambiguous in their conclusions the use of a single crystal provides greater clarity.

CHAPTER 2

Small Angle Neutron Scattering Studies of $TiBe_{1.5}Cu_{0.5}$

2.1 Small Angle Scattering

Observations of magnetic excitations in the $TiBe_{1.5}Cu_{.5}$ system has been performed using the small angle scattering instrument D11 at the Institut Laue Langevin(I.L.L).. The spectrometer was chosen for this experimental study because of its high angular resolution, high incident neutron flux and its ability to detect low momentum transfer scattering events (low q). No specific energy resolution is available on D11 and collected data is simply a measure of neutron scattering intensity against scattering angle (θ, where elastic $q=q_0=k_i \sin\theta$). The observed scattering intensities are directly proportional to the integrated differential cross section convolved with the machines inherent angular resolution.

In undertaking such an experiment the aim is to compare experimental data to a theoretical description in order to determine one or more unknown parameters. This is generally achieved by convolving the machine resolution with the calculated response rather than deconvolving it from the observed data.

2.2 Experimental Details

A schematic diagram of D11 is shown in figure 2.1.

The incident neutrons at the sample are produced at a cold source and are monochromated by a helical slot velocity selector providing a tuneable monochromated wavelength range from 4.5Å to 20Å with a full width half maximum of 9%. For this work a wavelength of 8Å was chosen in order to eliminate the detection of Bragg scattering events (Bragg cutoff=$2a_0/\sqrt{3}$=6.98Å. a_0=6.45Å, is the unit cell lattice parameter of $TiBe_{1.5}Cu_{0.5}$).

The effects of multiple scattering by the sample upon the collected intensities is very difficult to predict and in principle may be present. In practice these have been neglected. This is valid when (i) the sample is small so that multiple scattering probability is low (ii) the sample absorption cross-section is large compared to the scattering cross-section and (iii) less than about 10% of the incident beam is scattered.

The detection of neutrons on D11 is carried out by a 2-dimensional multiwire BF_3 proportional chamber that consists of an array of 64 x 64, 1 x 1 cm^2 elements. After the detection of an individual neutron each element has a dead time during which no further neutrons may be detected ($\approx 10^{-5}$s). If the incident intensity becomes too great saturation may result. Saturation of an individual cell also effects the neighbouring detector cells.

Figure 2.1 A schematic diagram of the D11 small angle scattering spectrometer. The distance between the neutron guide tube and the sample is equal to the sample-detector distance, both may be varied up to 40m. The liquid Helium cryostat can be used to create sample environments down to 1.2K.

Figure 2.1

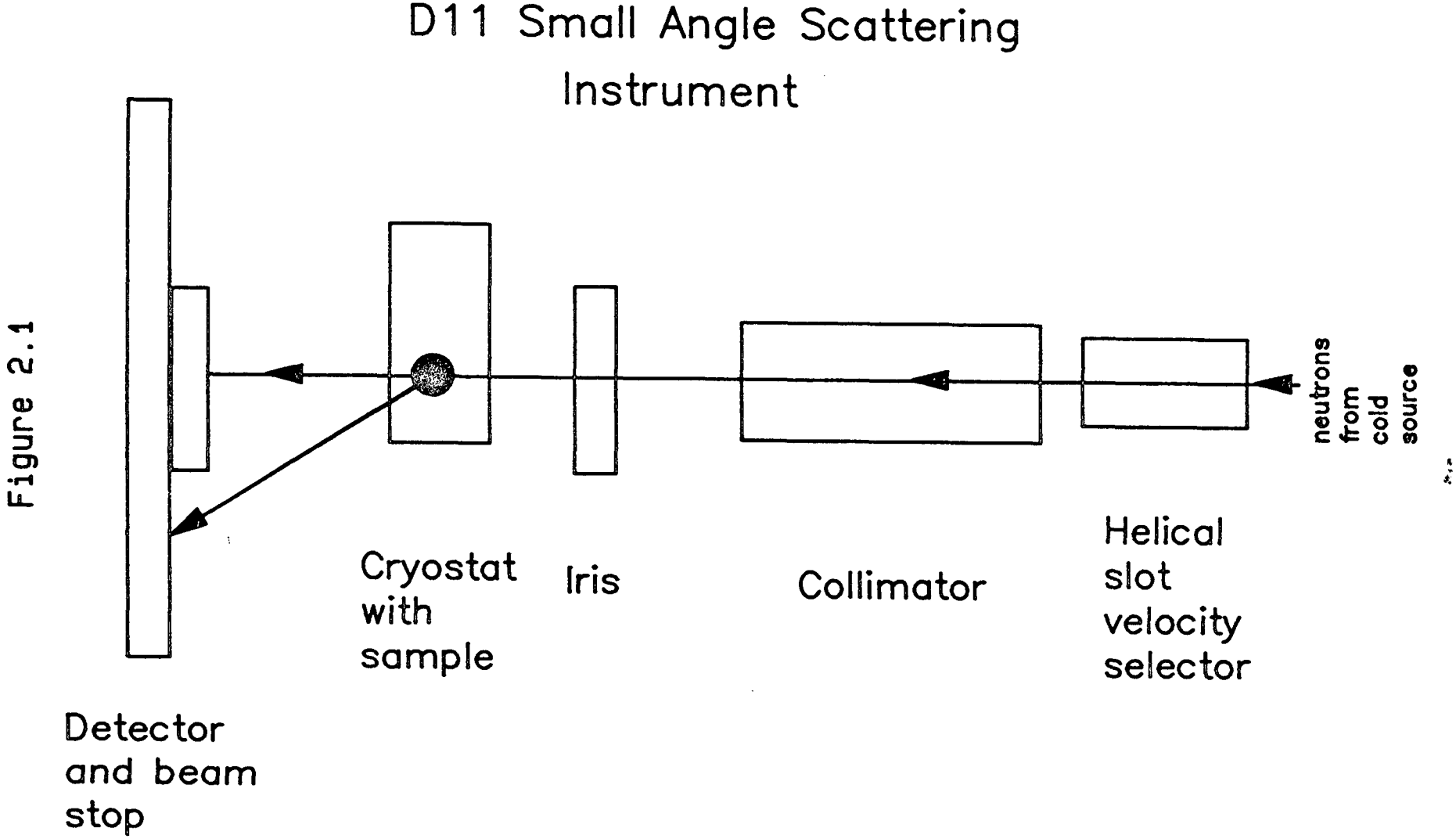
D11 Small Angle Scattering Instrument
neutrons from cold source
Helical slot velocity selector
Collimator
Iris
Cryostat with sample
Detector and beam stop

When this occurs it becomes necessary to either attenuate the beam or mask out the affected cells.

A large proportion of the incident beam is transmitted without scattering. The detector cells at very low angles to the incident beam thus become saturated. For this purpose a neutron opaque beam stop is placed directly in front of the affected cells. A modification to the beam stop has been made with the addition of five small holes cut parallel to the incident beam direction. This modification allows a small percentage of the transmitted beam to be analysed permitting the continuous monitoring of the sample transmission as a function of time and sample environment.

The sample is positioned midway between the end of the guide tube and the detector, this provides maximum angular resolution. The sample detector distance may be varied from 2.5m to 40m permitting measurements of q down to 10^{-3}Å. Whilst the resolution is increased with sample detector separation (r) the incident flux decreases rapidly and the solid angle decreases as $1/r^2$. For the experiments detailed in this work the sample detector distance was set to either 2.5m or 5m and measurements were taken over periods of 10 to 15 minutes, the actual time spent counting being governed by a preset value of a low efficiency (1%) fission chamber placed close to the sample between the guide tube and the sample.

2.3 The Inelastic Neutron Scattering Cross Section

In any neutron scattering experiment the partial differential cross section is sought. This is a function of both energy and momentum transfer from the neutron to the sample.

If the incident neutrons, in the most general case, have intensity I_o(neutrons/unit time/unit area) and energy E_o and the scattered neutrons intensity I(neutrons/unit time) and energy E at a position defined by the angles θ and ϕ then the partial differential cross section may be determined[17].

$$\frac{\Delta^2\sigma}{\Delta\Omega\Delta E} = \frac{I(\theta,\phi,E,E')}{I_o} \quad \frac{1}{\Delta\Omega\Delta E} \qquad 2.1$$

The quantities $\Delta\Omega$ and ΔE are the resolution of solid angle and energy transfer respectively and are functions peculiar to the chosen instrument.

On the D11 spectrometer there is no energy resolution and the collected intensities are the integrated response over energy, in this case the determined quantity is the differential cross section.

$$\frac{\Delta\sigma}{\Delta\Omega} = \frac{I}{I_o\Delta\Omega} \qquad 2.2$$

This is true for scattering of a single neutron by a target consisting of a single scattering centre and analysed with a perfect detector in the absence of any background signal. In reality there are many incident neutrons, many scattering centres, imperfect detectors, background signals and bandwidths to the incident neutrons and neutron scattering angles. For the accurate analysis of the collected intensities these must be taken into consideration. Further the incident neutron beam intensity I_0 must be accurately known. This parameter may be determined in two ways (i) by knowing the machine monitor count and its efficiency or (ii) by calibration to a material with a well known neutron cross section eg. vanadium.

2.4 Angular Resolution

In a real small angle scattering experiment the detected signal is that produced by a finite source, scattered from a sample with spatial extent and detected at a cell with finite area. The resultant detected intensity is a combination of scattering events with an angular spread defined by the machine geometry (see figure 2.2). If the distribution in angular spread is defined by the function $P(\theta-\theta_o)$, where θ_o is the angle subtended by the detector cell and the incident neutron flight path from the sample centre. Assuming isotropy in ϕ, then the observed cross section is given by

Figure 2.2 The theoretical scattering angle distribution is calculated from all possible scattering events arriving at the detector cells. The total experimental scattering intensity at $q_{el}(=q_0)$ is the addition of many cells at a fixed distance from the detector centre.

Figure 2.3 The calculated normalised probability distribution centered at an angle of θ=0.011 radians, where θ is the angle between the detector cell-sample centre vector and the wavevector **k**.

Figure 2.2

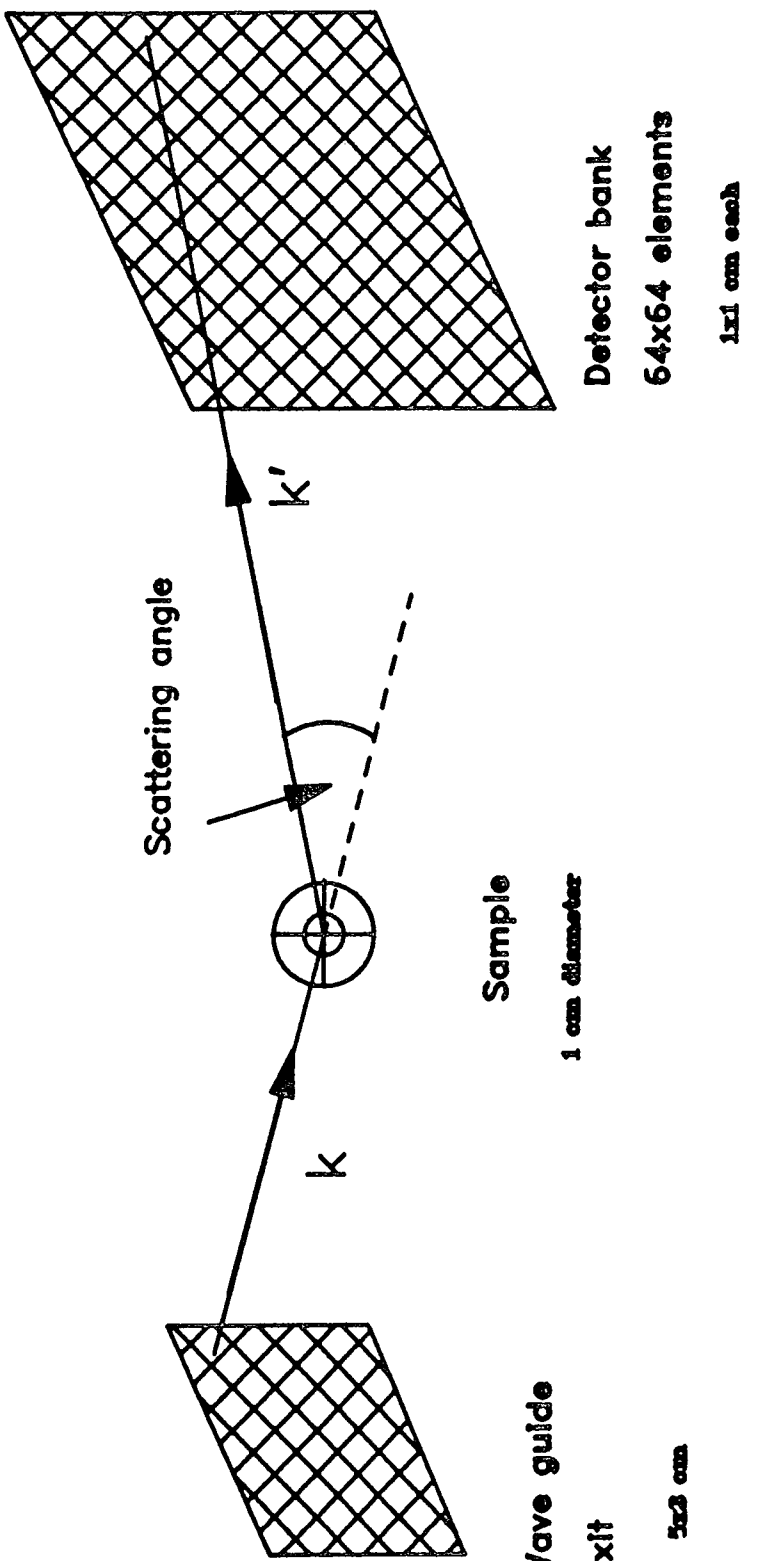
Detector bank
64x64 elements
1x1 cm each
k'
Scattering angle
Sample
1 cm diameter
k
Wave guide
exit
3x3 cm

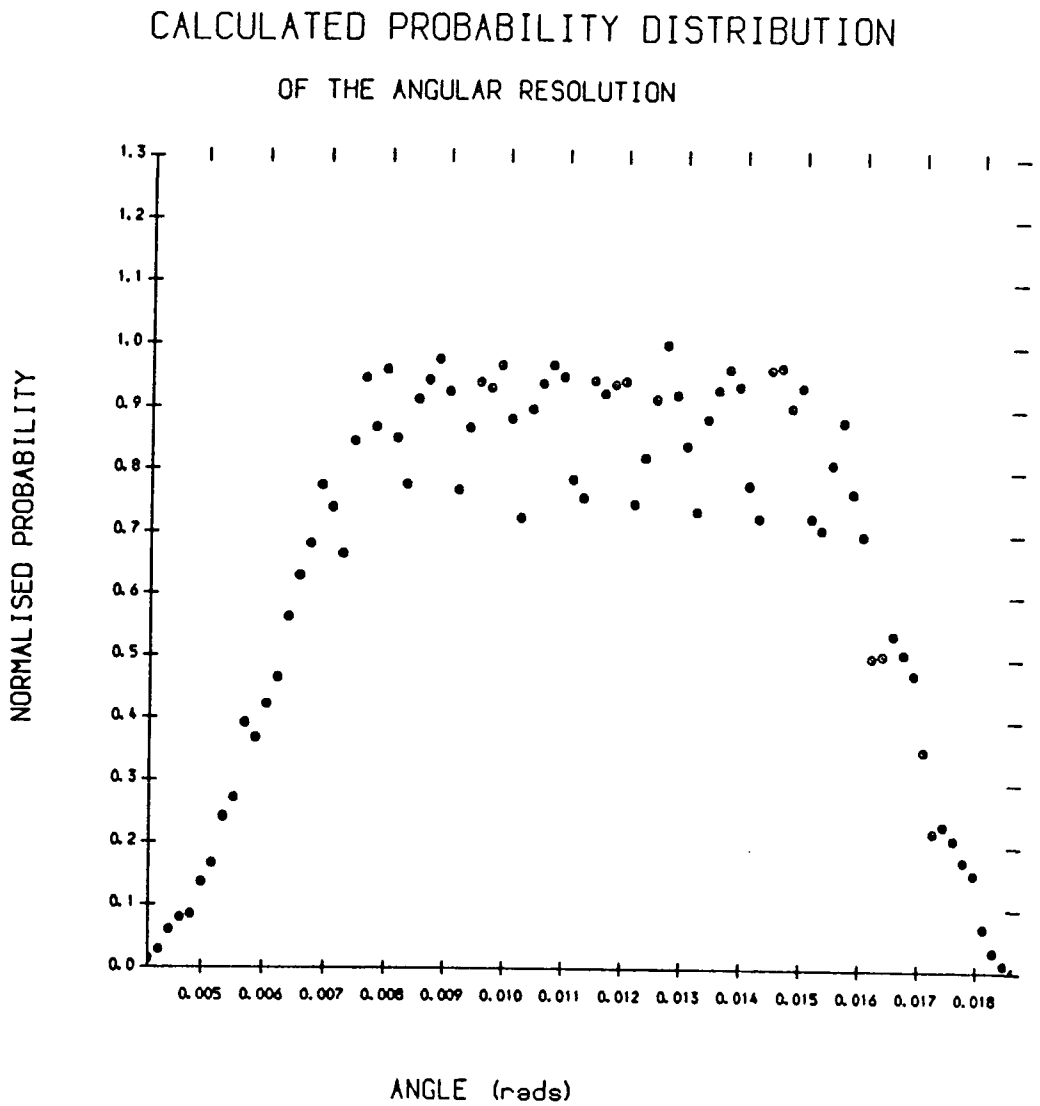
CALCULATED PROBABILITY DISTRIBUTION
OF THE ANGULAR RESOLUTION
NORMALISED PROBABILITY
1.3
1.2
1.1
1.0
0.9
0.8
0.7
0.6
0.5
0.4
0.3
0.2
0.1
0.0
0.005 0.006 0.007 0.008 0.009 0.010 0.011 0.012 0.013 0.014 0.015 0.016 0.017 0.018
ANGLE (rads)

Figure 2.3

$$\frac{\Delta\sigma}{\Delta\Omega} = \frac{\int_{\theta=\theta_{min}}^{\theta=\theta_{max}} P(\theta-\theta_o)\ 2\pi\sin\theta\ \frac{d\sigma(\theta)}{d\Omega}\ d\theta}{\int_{\theta=\theta_{min}}^{\theta=\theta_{max}} P(\theta-\theta_o)\ 2\pi\sin\theta\ d\theta} \qquad 2.3$$

Where θ_{min} and θ_{max} are the minimum and maximum possible scattering angles for scattering events detectable by the detector cell positioned a distance $d\tan\theta$ from the detector bank centre. d is the sample to detector distance (either 2.5 or 5m). θ is the angle between the incident and exit neutron wavevectors k and k'.

The functional form of $P(\theta-\theta_o)$ has been modelled using a computer program. The source and detector have been considered by subdivision into equal areas whilst the sample has been subdivided into equal volume elements. For each element of the source, sample and detector the scattering angle has been calculated and the result binned to provide an angle dependent probability function. The symmetry of the instrument eases this computation. The result is close to a Lorentzian line shape centred at $\theta=\theta_0$, however there are distinct maximum and minimum limits outside which there is no probability of observing a scattering response and the distribution has a flat top (figure 2.3).

2.5 The Theoretical Neutron Scattering Cross Section

The theoretical cross section for scattering is defined in general in the limit of the first Born approximation as[18].

$$\frac{d^2\sigma}{d\Omega dE'} = \frac{k'}{k}\left[\frac{m}{2\pi\hbar}\right]^2 \sum_{\lambda\sigma} P_\lambda P_\sigma \sum_{\lambda'\sigma'} \langle k'_{\sigma'\lambda'}|V|k_{\sigma\lambda}\rangle^2 \, \delta(\hbar\omega+E_\lambda-E_{\lambda'}) \qquad 2.4$$

Where k' and k are the scattered and incident wavevectors respectively. λ and λ' define the initial and final states of the system whilst P_λ and P_σ are the probabilities that the states λ and σ, the neutron spin states of the system, exist. The potential V includes both nuclear and magnetic components.

The state of the system both directly prior and after a neutron scattering event includes information on the nuclei, their spin and position as well as details of electron spin orientation for a system exhibiting magnetic ordering.

The delta function is included to represent the fact that energy is conserved during all scattering processes. For magnetic scattering of a non polarised neutron beam in the absence of nuclear scattering the magnetic part of equation 2.4 can be reduced , for diffuse scattering including only spin-spin magnetic scattering, to:

$$\frac{d^2\sigma}{d\Omega dE'} = \left[\frac{\gamma e^2}{m_e c^2}\right]^2 \frac{V}{N}\frac{k'}{k}\sum_{\alpha\beta}(\delta_{\alpha\beta}-\hat{k}_\alpha\hat{k}_\beta)\,\frac{1}{2\pi\hbar}$$

$$\times \int_{-\infty}^{\infty} dt\ e^{i\omega t} \langle s_\alpha(q,t) s_\beta(-q,0) \rangle \qquad 2.5$$

The correlation function $\langle s_\alpha(q,t) s_\beta(-q,0) \rangle$ is the expectation value of the time dependent Fourier transform of the spin density s(r,t), α and β describe the cartesian co-ordinates i,j,k, $(\gamma e^2/m_e c^2)^2 = 4\sigma_0$ where σ_0 is the neutron cross section (72.65 mbarns) and (N/V) is the number of atoms per unit volume in the sample. $s_\mu(k)$ are the Fourier transforms of the spin density of the entire sample :

$$s(k) = \sum_i e^{ik.R_i}\ s_i \qquad 2.6$$

The unpaired electrons at a given site form a total spin s_n by Hund's rules. It follows from the Wigner-Eckart theorem that[19]:

$$s(k) = \sum_i e^{ik.n}\ f(k)\ s_n \qquad 2.7$$

In a localised system for elastic scattering f(k) is referred to as the magnetic form factor. The inelastic form factor is unknown, however we are working in a limit where the the elastic f(k) may be safely used. In an itinerant system f(k) becomes increasingly difficult to interpret since by definition it describes the Fourier transform of the normalised spin density at a given lattice site. This apparent contradiction was first approached by Izuyama, Kim and Kubo[20] who showed that the localised form factors may be used validly for itinerant systems

under the condition of 3d atomic orbitals in the tight binding approximation. This is the approximation adopted in this work.

The form factors of the 3d atomic orbitals fall off very slowly in the region of low q and in general is taken as unity in the limit of this work[21].

The scattering function defining the small angle scattering cross section is defined through the response function S(q).

$$S(q) = \int d\omega\, S(q,\omega) \qquad 2.8$$

The angular and energy dependent scattering function is related to the imaginary part of the generalised susceptibility through the fluctuation dissipation theorem[18].

$$S(q,\omega) = \{1+n(\omega)\} \frac{N\hbar}{(g\mu_B)^2} X''(q,w) = \qquad 2.9$$

$$\frac{V}{N} \int_{-\infty}^{\infty} dt\, e^{i\omega t} \langle s_\alpha(q,t) s_\beta(-q,0) \rangle$$

Where $\{n(\omega)+1\}$ is the Bose Einstein thermal population function which is $n(\omega)+1$ for scattering events where the neutron loses energy and $n(\omega) = \frac{1}{(1-\exp(-\hbar\omega/k_B T))}$ for events where the neutron gains energy.

In the ferromagnetic state a general definition of the partial differential cross section may be obtained in terms of the imaginary part of the dynamical susceptibility $X''(q,\omega)$ in the transverse and longitudinal directions. If the local direction of magnetisation is in the z direction then (from equation 2.5)

$$\frac{d^2\sigma}{d\Omega dE'_{\perp}}_{inel} = \frac{k'}{k} 4\sigma_0 \frac{V}{N\pi(g\mu_B)^2} (1+\hat{k}_z^2) \{1+n(\omega)\} X''_{\perp}(q,\omega) \quad 2.10$$

$$\frac{d^2\sigma}{d\Omega dE'_{\parallel}}_{inel} = \frac{k}{k'} 4\sigma_0 \frac{V}{N\pi(g\mu_B)^2} (1-\hat{k}_z^2) \{1+n(\omega)\} X''_{\parallel}(q,\omega) \quad 2.11$$

In the absence of an applied magnetic field (i.e. in an isotropic q state) and averaging over several magnetic domains the following are true

$$k_x^2 + k_y^2 + k_z^2 = 1 \quad 2.12$$

$$k_x^2 = k_y^2 = k_z^2 \quad 2.13$$

thus $$k_z^2 = 1/3 \quad 2.14$$

The Debye Waller factor has not been introduced into these equations. This defines the effect upon the scattering owing to thermal vibrations of the atoms about their equilibrium positions. At low q and low temperatures this has little effect on the

observed magnetic scattering intensities and its value e^{-2W} may be taken as unity where 2W is merely the square of the dot product of the mean displacement of the nucleus with the scattering wavevector.

In the paramagnetic regime all directions are equivalent as there is no direction of magnetisation. In this case again k_z^2 =1/3 and the longitudinal and transverse contributions to the differential cross section become indistinguishable. In the ferromagnetic regime the scattering cross section is dominated by the spin wave contribution that is by the transverse component.

2.6 Modeling the Dynamical Susceptibility

The aim of this work is to describe the observed scattering data for which a good model of $X''(q,\omega)$ is essential. No analytical solution exists for the system $TiBe_{1.5}Cu_{0.5}$ under investigation due to its extreme complexity. The solution would depend on all interactions experienced by the electrons in the system in all q,ω space and require a detailed knowledge of the system quantum mechanical band structure and variations with physical conditions.

For this reason a simple phenomenological model is used that may be a valid approximation in the long wavelength and low frequency domain. This differs from the early approach used by Izuyama, Kim and Kubo[20] and that of Moriya in that it is not limited by the constraints of a single parabolic band description

or the tight binding limit. The description used within the same framework by Lonzarich and Taillefer[16] has proved successful in accounting for observations both from neutron scattering and de-Haas Van Alphen studies of weak itinerant ferromagnets Ni_3Al[22,23,24], MnSi[25] and the strongly enhanced paramagnet Ni_3Ga[26].

2.7 The Generalised Susceptibility in the Tight Binding Limit

The generalised susceptibility for a single parabolic tight binding model is generally developed from the expansion of Lindhard functions with the incorporation of interactions using the generalised mean field approximation[19,20].

$$X_0(q,\omega) = \frac{1}{N} \lim_{\xi \to 0} \sum_{k} \frac{f_k - f_{k+q}}{\epsilon_{k+q} - \epsilon_k - \hbar\omega - i\xi} \qquad 2.15$$

Where ξ is a small positive number, f_i are the fermi occupation numbers, ϵ is the electron energy level and

$$X^{-1}(q,\omega) = X_0^{-1}(q,\omega) - I(q,\omega) \qquad 2.16$$

Where $I(q,\omega)$ is the interaction tensor.

In the static, long wavelength limit $\omega \Rightarrow 0$, $q \Rightarrow 0$, $X(q,\omega)$ is the measured bulk susceptibility and the above equation reduces to the Stoner relationship relating the molecular field enhanced

static susceptibility X_s to the Pauli susceptibility X_{so} calculated in terms of the bare electron band mass.

$$\lim_{\substack{w\to 0 \\ q\to 0}} X_0''(q,\omega) = 0 \qquad 2.17$$

$$\lim_{\substack{w\to 0 \\ q\to 0}} X_0'(q,\omega) = \rho\epsilon_f \qquad 2.18$$

$$\text{Then } X(q,\omega) = X_s = \frac{X_{so}}{1-I} \qquad 2.19$$

1/1-I is the Stoner enhancement factor.

In the random phase approximation

$$X(q,\omega) = \frac{X_0(q,\omega)}{1-IX_0(q,\omega)} \qquad 2.20$$

Where I is a function of q and ω for all q,ω.

Figure 2.4 show contours of the imaginary part of the transverse generalised susceptibility in the ferromagnetic state in k,ω space determined with the inclusion of electron correlations. When electron correlations are added and the Stoner enhancement factor is sufficiently large a collective spin wave mode appears at small k corresponding to highly correlated electron-hole excitations. Away from low q,ω the collective modes enter the Stoner continuum (single particle excitations) and are damped by decaying into Stoner excitations.

Figure 2.4 Contour plot of the imaginary part of the transverse generalised susceptibility in the ferromagnetic state. The spin wave branch lies below the Stoner edge, scattering events occurring outside this regime are damped by the Stoner continuum.

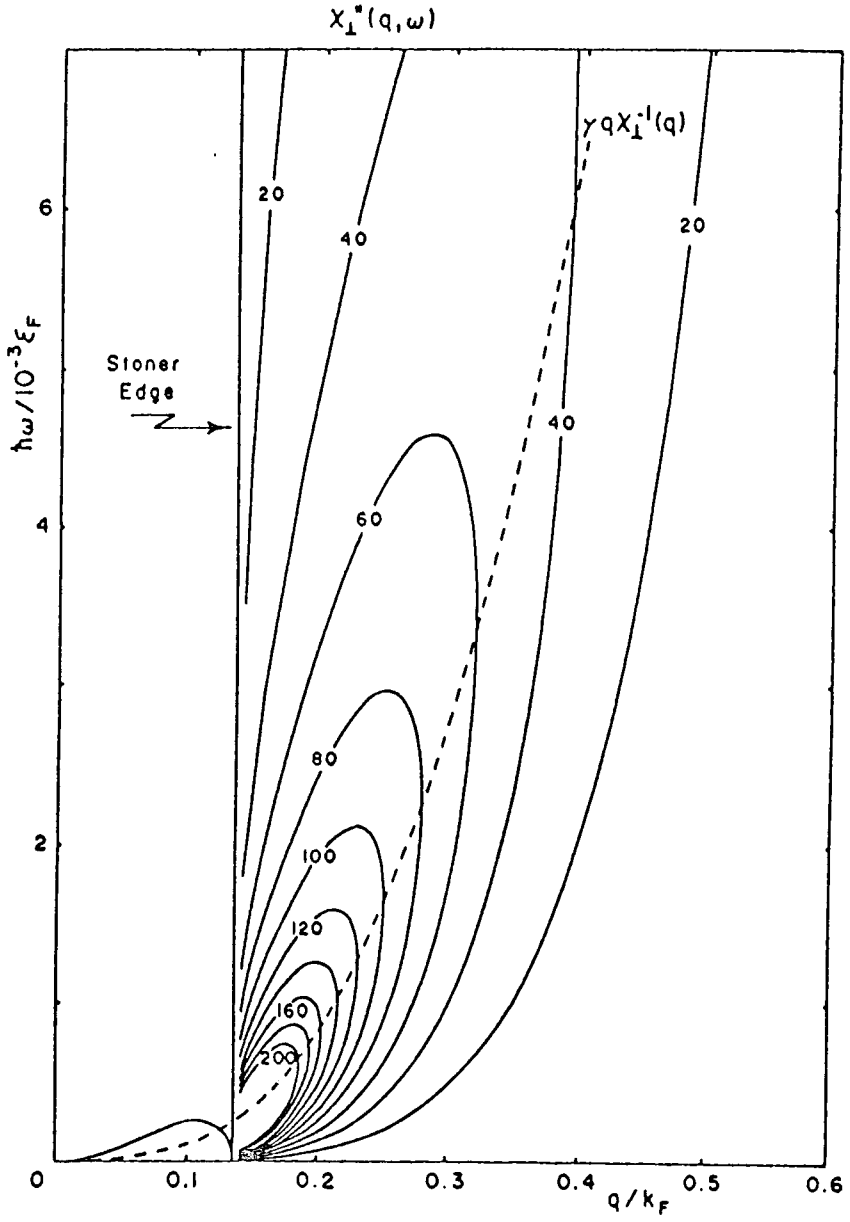
$\chi_\perp''(q,\omega)$
$\gamma q \chi_\perp^{-1}(q)$
Stoner Edge
20
40
60
80
100
120
160
200
20
40
$\hbar\omega/10^{-3}\epsilon_F$
q/k_F
0
0.1
0.2
0.3
0.4
0.5
0.6
2
4
6

Figure 2.4

The effect of spin fluctuations on the thermodynamic properties of this class of material is important in the low energy, long wavelength regime. It is essential to consider the effects of feedback of magnetic fluctuations upon the dynamic susceptibility in a self consistent manner. (known as Self Consistent Renormalisation S.C.R.).

This has been approached in the work by Moriya[27] who considered a renormalisation process independent of q and ω whilst demanding consistency between the calculated susceptibility and that given by the equation of state in the zero frequency limit. An additional contribution $\lambda(q,\omega)$ is introduced into the model to describe the effects of highly temperature dependent mode-mode coupling. In general $\lambda(q,\omega)$ is approximated to $\lambda(0,0)$.

$$X(q,\omega) = \frac{X_0(q,\omega)}{1-IX_0(q,\omega)+\lambda(0,0)} \qquad 2.21$$

The imaginary part of the susceptibility governing the neutron scattering response is given by:

$$X''(q,\omega) = \frac{(1+\lambda(0,0))\ X_0''(q,\omega)}{[1-IX_0'(q,\omega)+\lambda]^2+[IX_0''(q,\omega)]^2} \qquad 2.22$$

2.8 The Magnetic Regimes

In weak itinerant ferromagnetic materials three distinct scattering regimes exist (i) $T << T_c$ (ii) $T \approx T_c$ and (iii) $T > T_c$. In the region where $T \approx T_c$ or the critical scattering regime the total scattering cross section becomes very large and correlations persist over large distances and long time scales. The analysis of such scattering is beyond the scope of this work.

(i) $T << T_c$ - The spin wave regime

When long range ferromagnetic ordering exists the inelastic neutron scattering cross section is dominated by spin wave excitations at low q,ω, that is by the transverse component of the generalised susceptibility. For undamped spin waves in itinerant ferromagnets the imaginary part of the susceptibility can be shown to be represented by[18]:

$$X''_{\perp}(q,\omega) = \frac{1}{2} \pi \omega X_{\perp}(q) [\delta(\hbar\omega-\hbar\omega(q)) + \delta(\hbar\omega+\hbar\omega(q))] \qquad 2.23$$

Where for small q the spin waves have quadratic dispersion ie. $\hbar\omega \approx Dq^2$. D is referred to as the spin wave stiffness. This is true only in the absence of internal anisotropy. D may be related to the fundamental parameter c used in the description of the magnetic nature of the material[16].

$$D = 2\mu_B c_{\perp} M \qquad 2.24$$

Where $c_{\perp} = c_{\parallel} = c = \dfrac{\partial^2 \ln X}{\partial q^2}$ and $X^{-1}(q) \cong cq^2$ below T_c, in the limit where the spontaneous magnetisation M is small.

In addition to c three other basic parameters are required to provide a complete description of the magnetic nature of these systems using the chosen phenomenological description. These are a,b and γ. a and b may be determined from the magnetic field dependence of the magnetisation in the T=0 limit (see chapter 4) whilst γ can be found from neutron scattering.

For a detailed explanation of these parameters, the way in which a,b and c are related to a Ginzburg Landau expansion of the free energy of the system and how γ is related to the fluctuation relaxation period the paper by Lonzarich and Taillefer[16] should be referred to.

The spin wave stiffness (D) is temperature dependent to lowest order, one anticipates the stiffness to scale as the magnetisation (M) with a temperature dependency which may be empirically expressed as:

$$\frac{D(T)}{D(0)} = \frac{M(T,0)}{M(0,0)} = \left(1-\left(\frac{T}{T_c}\right)^2\right)^{1/2} \qquad 2.25$$

This functional form and its applicability has been studied in the investigations of $TiBe_{1.5}Cu_{0.5}$ and discussion is provided

later as to its applicability.

(iii) $T > T_c$ - The paramagnetic regime

At temperatures above T_c the thermal energy is sufficient to break long range magnetic ordering. Despite the absence of any long range order the motions of close spins are still strongly coupled. In this regime the transverse and longitudinal susceptibilities loose their identity and the observed diffuse response corresponds to over damped non propagating fluctuations. $X''(q,\omega)$ may be modeled in the following phenomenological form:

$$X''(q,\omega) = \frac{\omega\, X(q)\, \Gamma(q)}{\omega^2 + \Gamma(q)^2} \qquad 2.26$$

with a relaxation frequency

$$\Gamma(q) = \gamma\, q\, X^{-1}(q) \qquad 2.27$$

Further we may expand

$$X^{-1}(q) = X^{-1} + cq^2 + \ldots \qquad 2.28$$

Where in our model c may be related to the spin wave damping constant below T_c (equation 2.24).

In the light of previous successes of the qualitative self consistent renormalised random phase approximation model of

Lonzarich and Taillefer[16] in providing an interpretation of the observed low q,ω characteristics in both enhanced paramagnets and weak ferromagnets the model has been applied to observations of $TiBe_{1.5}Cu_{0.5}$ observed neutron small angle scattering intensities.

Poor fits between experimental data and calculated responses however resulted in the search for an alternative model. It has been shown in the case of the well known itinerant ferromagnet $ZrZn_2$[28] that a more advanced description based upon damping of spin wave modes is necessary to describe the observed neutron scattering. The model of damping chosen in this work differs from that used for $ZrZn_2$, which was based upon a description of a single dynamical variable[29] by considering two dynamically coupled variables corresponding to the transverse components of the magnetisation vector.

The discussions of the chosen model begins with an account of applications of the S.C.R. R.P.A. model to the collected data and a brief description of this model within the quasistatic limit is provided. The quasistatic limit model is often used in preference as a starting point for the fitting of a restricted amount of data points since it reduces the description to one depending upon a single independent parameter.

2.9 Modeling the Data

If the incident neutron has wavevector k and is scattered from a single point particle resulting in an exit wavevector k'

then only specific events in q,ω space can occur within the confines of the chosen model.

In general if the momentum transfer is $\hbar q = \hbar(k'-k)$ and the energy change (with respect to the neutron) is $\hbar\omega = 2.072(k^2-k'^2)$ (in units of mev and Å) then the locus of trajectory in q,ω space is defined for scattering occurring with a scattering angle θ by:

$$q^2 = k^2\left[2 - \frac{\hbar\omega}{E_i} - 2\cos\theta\left(1 - \frac{\hbar\omega}{E_i}\right)^2\right] \qquad 2.29$$

Where E_i is the incident neutron energy and the neutron energy transfer $\hbar\omega = (\hbar^2/2m)[k^2-k'^2]$.

The dispersion of undamped spin waves with spin wave stiffness D is given by $\hbar\omega = Dq^2 + E_g$ where E_g is the energy gap owing to crystal anisotropy.

Where these two curves intersect in q,ω space a scattering event may occur (figure 2.5).

If θ is less than the critical scattering angle θ_c where the two curves become tangential, four scattering events are possible, two for neutron energy gain and two for loss, for each individual scattering angle

When the spin waves are damped the line $\hbar\omega = Dq^2 + E_g$ defines the pole position of the distribution that has finite width (along

Figure 2.5 The trajectories in q,ω space corresponding to detector angles of 1-6^{0}. The dotted line represents the spin wave dispersion for $\hbar\omega=D(T)q^{2}+E_{g}$ with $E_{g}=0$ and $D=60mev\AA^{2}$ and the critical angle lies at approximately 2 degrees. The energy and momentum transfers have been scaled to the neutron incident energy and momentum. If the resolution function where of a delta function type response then the only region accessible for the detection of neutrons is at angles below 2 degrees for scattering from undamped spin waves.

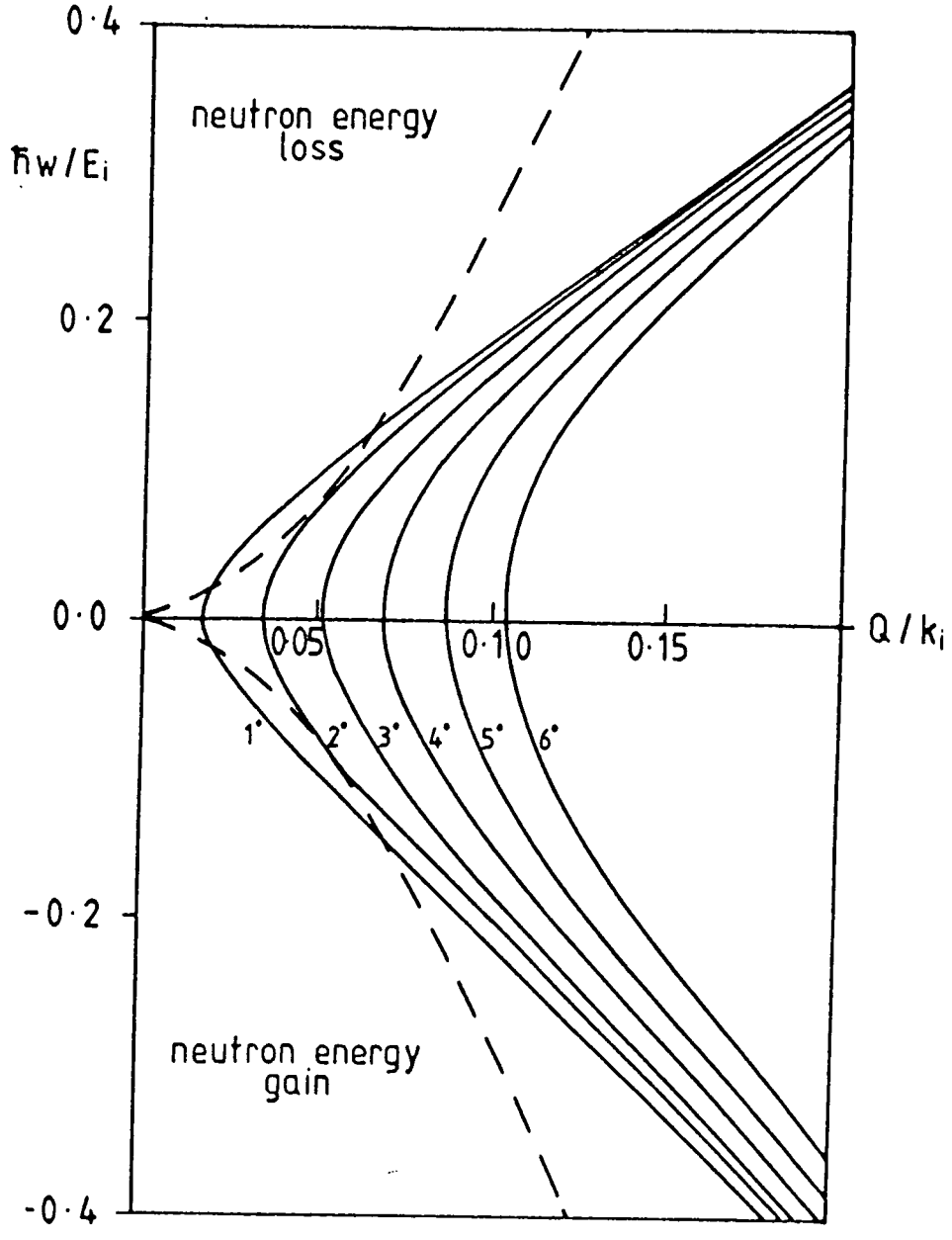
0·4
neutron energy
loss
ħw/Eᵢ
0·2
0·0
0·05
0·10
0·15
Q / kᵢ
1°
2°
3°
4°
5°
6°
-0·2
neutron energy
gain
-0·4

Figure 2.5

a constant q direction). Scattering events may occur in all q,ω space with a probability defined by the functional form of the damped spin wave dynamic generalised susceptibility and the position of the intersection with the constant θ trajectory.

2.10 Within the Quasistatic Limit

When the neutron velocity is much greater than the phase velocity of the system fluctuations the theoretical small angle scattering cross section may be considered in the quasistatic limit. In this case the fluctuations as viewed by the neutron are essentially stationary.

Within the limits defined by small θ (small angle scattering $\theta \leq 5^{\circ}$) and energy $\frac{\hbar\omega}{E_i} << 1$ then q^2 (equation 2.29) may be expanded in terms of θ and $\frac{\hbar\omega}{E_i}$, to second order :

$$q^2 = k^2 \left(\theta^2 + \frac{(\hbar\omega)^2}{(2E_i)^2} \right) \qquad 2.30$$

In the quasistatic limit the quadratic dependence on energy is ignored and q is therefore equal to elastic q_{el}.

$$q \approx k\theta = q_{el} \qquad 2.31$$

For energies much less than typical thermal energies the population factor $n(\omega) = (1 - e^{-\hbar\omega/k_B T})^{-1}$ is large and may be

approximated to $k_B T/\hbar\omega$.

Additionally within this limit since $k \cong k'$ the scattering cross section reduces to the form:(see appendix A)

$$\frac{d\sigma}{d\Omega} = \int_{-\infty}^{\infty} \frac{d^2\sigma(q,\omega)}{d\Omega dE'} dE' = \text{constant } T\ X(q) \qquad 2.32$$

Where $X(q)$ is the static wavevector dependent susceptibility and may be expressed in the ferromagnetic regime as the sum of the longitudinal and transverse components.

$$X(q_o) = \frac{2}{3} X_{\perp}(q_o) + \frac{1}{3} X_{\parallel}(q_o) \qquad 2.33$$

The longitudinal contribution is modelled below T_c as a diffuse response centred at $\omega=0$ with the same form as the line shape used to describe the paramagnetic susceptibility and is generally found to be small, until close to $T \approx T_c$ and may be safely omitted during the simulation of experimental data.

The quasistatic limit provides a model that has restrictions in application to a limited region in q,ω space. Often only three or four experimental observations taken on the D11 small angle neutron scattering instrument meet the requirements for a given temperature scan. It has been included here for completeness as an initial step often taken in the analysis of the collected data.

2.11 The S.C.R. R.P.A. Model

Analysis of the ferromagnetic transverse collective modes was attempted using the response form developed from simple S.C.R. R.P.A. theory. The response line shape of the model is given by:

$$f(q,\omega) = \frac{1}{2} \left(\delta(\hbar\omega - \hbar\omega(q)) + \delta(\hbar\omega + \hbar\omega(q)) \right) \qquad 2.34$$

Where $\hbar\omega(q) = Dq^2 + E_g$, E_g is the spin wave energy gap arising from sample anisotropy and the generalised dynamical susceptibility may be expressed as:

$$X''(q,\omega) = -\pi\, \omega\, X(q)\, f(q,\omega) \qquad 2.35$$

from the Kramers-Kronig relationships.[19]

To model the experimental data the theoretical response is integrated along a constant θ trajectory for the entire energy spectrum. This corresponds to a skewed path in ω,q space that requires an energy dependent correction factor for the area under the integral (Jacobian of integration) to the differential cross section.

The differential cross section for a single scattering event may be written in the S.C.R. model for both neutron energy gain and loss events as:

$$\frac{d\sigma}{d\Omega} = \text{constant} \int_{\substack{\text{constant} \\ \text{theta}}} \{n(\hbar\omega)+1\}\ \delta(\hbar\omega \pm \hbar\omega(q))\ d\omega \qquad 2.36$$

By setting $\hbar\omega \pm \hbar\omega(q) = z$

$$\frac{d\sigma}{d\Omega} = \int \frac{dz\ n(\hbar\omega(z))}{\left| 1 \pm \frac{\partial\omega(q)}{\partial q}\frac{\partial q}{\partial\omega} \right|} \qquad 2.37$$

and knowing that

$$\left| 1 \pm \frac{\partial\omega(q)}{\partial q}\frac{\partial q}{\partial\omega} \right|^{-1} = J \quad \text{the Jacobian of integration} \qquad 2.38$$

and $$\frac{\hbar\partial\omega(q)}{\partial q} = 2Dq \qquad 2.39$$

using the first order approximation

$$q^2 = k^2 \left(\theta^2 + \frac{(\hbar\omega)^2}{16k^4} \right) \qquad 2.40$$

and differentiating

$$q\frac{\partial q}{\hbar\partial\omega} = \frac{\hbar\omega}{16k^2} \qquad 2.41$$

by letting $a=\omega/4k^2$ and solving $2a\sin\theta_c = a^2 + \theta_c^2$ for a, since

$$J = 1 \pm \frac{a}{\sin\theta_c} \qquad 2.43$$

Where θ_c is the critical angle where the neutron flight path and the spin wave dispersion become tangential i.e. $\frac{\partial\omega(q)}{\partial q}\frac{\partial q}{\partial\omega}=1$, the Jacobians of integration become infinite. θ_c is also the angle above which no undamped spin wave scattering is observable in the absence of any internal anisotropy and is given by $\sin\theta_c = \frac{\hbar^2}{2mD}$ for both neutron energy gain and loss.

The Jacobian of integration may be shown under these conditions to be equal to:(see appendix A)

$$|J| = (1-\theta^2/\theta_c^2)^{-0.5} \qquad 2.42$$

Using this formulation the expressions for neutron energy gain and loss reduce to identical forms

$$|J| = |J^{\pm}_{loss}| = |J^{\pm}_{gain}| \qquad 2.44$$

Where $J^{\pm}_{loss}$ and $J^{\pm}_{gain}$ represent the Jacobians of integration for the four possible solutions of the quadratic equation describing the intersection of the spin wave dispersion curve with the constant θ trajectory.

Considering both neutron energy gain and loss events the complete expression for the cross section becomes:

$$\frac{d\sigma}{d\Omega} = \text{constant} \sum_{i=\pm} [\, n(\hbar\omega_l^i+1)J(\hbar\omega_l^i) + n(\hbar\omega_g^i)J(\hbar\omega_g^i) \,] \qquad 2.45$$

Where $hw_{g,l}^{\pm}$ represent the four solutions of the quadratic equation describing the intersection of the spin wave dispersion and the neutron flight path in q,ω space for both neutron energy gain (g) and loss (l) events.

If internal anisotropy exists within the scattering system and the energy gap is finite then the critical angle of scatter for small angle scattering is given by:

$$\sin\theta_c = \left(\frac{4}{D^2} - \frac{2E_g}{Dk^2} \right)^{0.5} \qquad 2.47$$

and the Jacobians of integration become

$$|J_{loss}^{\pm}| = \left| -1 + \frac{1}{\sin\theta_c} \left(-1 + \frac{\cos\theta}{\left(1 - \frac{\hbar\omega\pm_{loss}}{E_i} \right)^{0.5}} \right) \right| \qquad 2.48$$

$$|J_{gain}^{\pm}| = \left| 1 + \frac{1}{\sin\theta_c} \left(-1 + \frac{\cos\theta}{\left(1 + \frac{\hbar\omega\pm_{gain}}{E_i} \right)^{0.5}} \right) \right| \qquad 2.49$$

and in general

$$\omega^{\pm}_{gain} = \frac{2E_i}{(\sin\theta_c - 1)^2}\left[\left[(\sin\theta_c - 1)\left(\frac{Eg}{2E_i\sin\theta_c}+1\right) + \cos^2\theta\right] \pm\cos\theta\left[\sin^2\theta_c - \sin^2\theta - \frac{Eg}{E_i\sin\theta_c}(1-\sin\theta_c)^{0.5}\right]^{0.5}\right] \quad 2.50$$

and

$$\omega^{\pm}_{loss} = \frac{2E_i}{(\sin\theta_c + 1)^2}\left[\left[(\sin\theta_c + 1)\left(\frac{Eg}{2E_i\sin\theta_c}+1\right) - \cos^2\theta\right] \pm\cos\theta\left[\sin^2\theta_c - \sin^2\theta - \frac{Eg}{E_i\sin\theta_c}(1+\sin\theta_c)^{0.5}\right]^{0.5}\right] \quad 2.51$$

It is clear from the definitions of the Jacobians of integration that as θ approaches θ_c the integral becomes infinite. To establish whether or not this is an artifact of the chosen model or a real feature an analytical solution has been sought in the $E_g \cong 0$ and $\theta \cong \theta_c$ limit.

A simple solution is obtained in the high temperature limit.

$$\frac{d\sigma}{d\Omega} = \frac{16}{3\pi}\frac{\sigma o}{(g\mu_B)^2}\frac{N}{V}\frac{k'}{k}k_B T \ln\left(\frac{\tan\left(\frac{1}{2}\sin^{-1}(\theta_2/\theta_c)\right)}{\tan\left(\frac{1}{2}\sin^{-1}(\theta_1/\theta_c)\right)}\right) \quad 2.52$$

This solution does not diverge and includes both energy gain and loss events. A computer program has been written in order to

apply these models with a switch over from the numerical to the analytical solution as the critical angle is approached to avoid the singularity in equation 2.51. In addition the program models the real spectrum by including all scattering events weighted by $P(\theta-\theta_0)$.

No analytical solution has been found for $E_g \neq 0$ in the $\theta \approx \theta_c$ limit.

The observed scattering cross section at a given detector angle θ is represented by:

$$\frac{\Delta\sigma}{\Delta\Omega} = \frac{\sum_{\theta_1=\theta_{min}}^{\theta_2=\theta_{max}} P_i(\theta-\theta_i) \int 2\pi\sin\theta \frac{d\sigma(\theta)}{d\Omega} d\theta}{\sum_{\theta_1=\theta_{min}}^{\theta_2=\theta_{max}} P_i(\theta-\theta_i) \int 2\pi\sin\theta \, d\theta} \qquad 2.53$$

P_i is the probability function of the angular resolution. $\theta_{min/max}$ are the limits of the angular scattering for the scattering angle θ_i defined by the instrument geometry.

2.12 The Damped Coupled Model of Collective Fluctuations

Due to a lack of refinement between the δ function type response and the experimental data a more general solution has been sought. To this end an elementary phenomenological model has

been used which reduces smoothly to a diffuse response in the limit that the spin wave pole energy collapses to zero (ie. $>T_c$). This model is based upon the vector nature of the magnetisation density fluctuations in the ferromagnetic phase. A detailed discussion and theoretical determination of this type of distribution is give by Forster[30] and a more basic discussion based on coupled harmonic oscillators is provided in appendix B. The imaginary part of the dynamic susceptibility under the conditions of an isotropic ferromagnet, total spin conservation and ignoring any lattice structure effects is given by:

$$X''_{\perp}(q,\omega) = X_{\perp}(q)\,\omega\,\frac{\Gamma(q)\,(\,\omega^2+\omega_0^2+\Gamma^2(q)\,)}{(\omega^2-\omega_0^2-\Gamma^2(q))^2+4\Gamma^2(q)\omega^2} \qquad 2.54$$

Where $X_{\perp}^{-1}(q) = cq^2+X_{\perp}^{-1}$ and $\Gamma(q) = \gamma q\chi_{\perp}^{-1}(q)$

$\hbar\omega_0(q)$ is the spin wave energy at the pole equal to Dq^2+E_g. $X_{\perp}^{-1}$ is zero in the absence of anisotropy or external magnetic fields and c is the same as discussed previously.

The choice of the form of $\Gamma(q)$ is governed by the RPA theory[20] and observations that γ is temperature and wavevector independent for the data . Ignoring the longitudinal component of the generalised susceptibility which is at least an order of magnitude smaller than the transverse component contribution the cross section is given by:

$$\frac{d^2\sigma}{d\Omega dE} = \frac{4\sigma o}{\pi(g\mu_B)^2} \frac{V}{N} \sum_{k} \{n(\omega)+1\} \left[\frac{4}{3} X''_{\perp}(q,\omega)\right] \qquad 2.55$$

CHAPTER 3

Sample Preparation

Single crystals of $ZrFe_2$ and polycrystalline ingots of MnSi have been prepared. The production of high purity samples is essential for neutron scattering investigations.

For this purpose a cold crucible technique has been employed to grow samples by melting together their constituent elements. The metal grower has been designed and built specifically to meet the requirements of neutron scattering samples. A significant proportion of the total effort reported in this thesis has been spent in the design and production of the cold crucible and the subsequent growth of the specimens.

3.1 The Cold Crucible

The cold crucible technique of metal growth essentially consists of a horizontal copper boat through which cooling water is continuously passed. The constituent elements sit on the boat and are fused together using radio frequency induction heating. The use of RF induction enables samples to be mixed thoroughly in the melt by the motion of eddy currents.

The copper boat is suspended from one end, attached to a

stainless steel chamber, inside a silica glass cavity that may be either evacuated or filled with a highly pure inert gas atmosphere. All gas and vacuum lines are attached to the stainless steel chamber with ultra high vacuum couplings and valves. The design details are shown in figure 3.1.

The cold crucible method of crystal growth allows samples to be heated to temperatures in excess of 1600°C whilst the sample receives very little contamination from the cooled copper boat. The technique has several advantages over alternative methods of sample preparation such as the hot crucible and electric furnace systems. Not least of which is the ability to view the entire sample at all times during any chosen heat, melt, cool cycles. In addition crystal enhancement techniques such as Bridgman cooling and zone refinement may be employed[31]. The major disadvantage is that large heat gradients exist at the sample boat interface. Such discontinuities are not conducive to the growth of large crystals. This problem is negated if as is sometimes the case the internal sample convection currents are large. This source of potential anisotropy and its consequences to the crystal domain structure of the cast ingot should be borne in mind when attempting to cut orientated single crystals from the bulk, preferential choice being given to specimens at the top of the sample.

3.2 Temperature Measurements

The sample temperature is monitored at all times using an

Figure 3.1 The horizontal cold boat crucible rig for the mixing and growth of metallic samples. The samples are heated directly by radio frequency induction. The crucible is totally enclosed in a sealed environment.

COLD CRUCIBLE

Figure 3.1

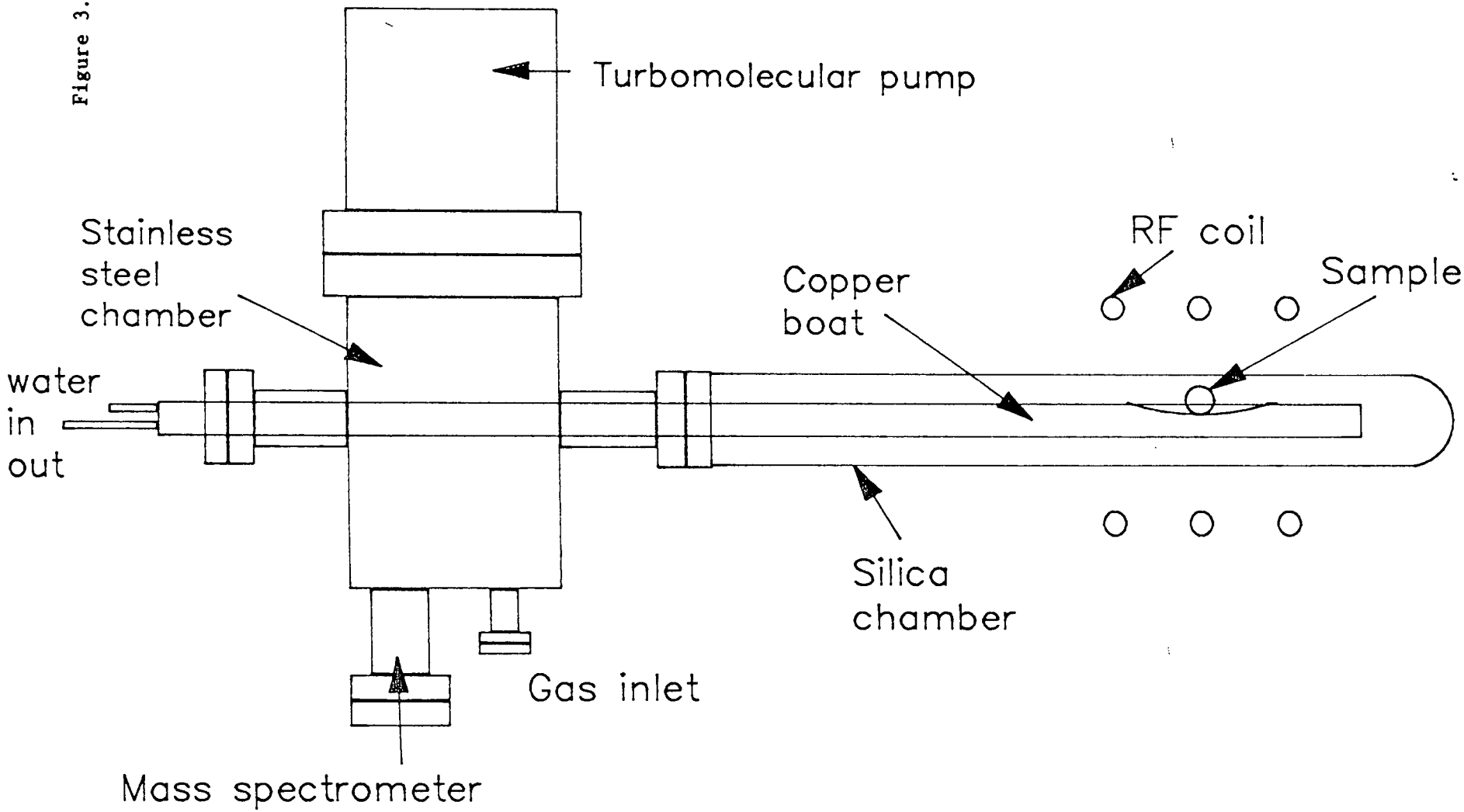

optical pyrometer. The pyrometer is first calibrated against pure metals for which sample emissivity, absorption and melting points are well known. For this purpose pure iron and zirconium were used.

There are two potential inaccuracies involved in measuring the temperatures of binary metal systems using this system. The first is a consequence of binary metal systems for which emissivity and unique melting points are not well established. The second is associated with the matching of emission colour to the hot glowing wire in the pyrometer using the naked eye. The exact reproducibility of sample growth conditions is therefore restricted. It has been estimated that any single temperature reading is accurate to around $\pm 20^{0}C$ if no metal deposits on the inside of the silica glass cavity, due to sample evaporation, obscure the view of the heated sample.

3.3 The Atmosphere of Growth

To meet the specifications for sample quality ($\leq$100ppm impurity level) the growth chamber and its atmosphere purity are of great significance. The chamber has been designed to obtain vacuum better than 10^{-7}mbar or retain an inert gas atmosphere at levels greater than atmospheric pressure. The vacuum can comfortably be obtained on the system without recourse to lengthy bake out procedures that are employed for highly hygroscopic samples. An inert gas atmosphere of either Helium or Argon is available with $\approx$1ppm impurities when necessary, however this

impurity level corresponds to only a medium vacuum of 10^{-3} mbar, preference being given to an evacuated chamber when ever practical.

The growth of $ZrFe_2$ necessitated the use of a gas atmosphere due iron's high vapour pressure ($1787^{o}C$ v.p. of 1mmHg). Without an over pressure, differential evaporation occurs and an off stoichiometric product results. Whilst helium gas can be obtained in a purer form than argon simply by using the boiled off gas from liquid helium it conducts heat away from the sample some four times faster than argon. The limited RF power (25KW continuous use) and the gas over pressure limit due to chamber construction meant that argon gas was chosen as the chamber atmosphere.

The argon obtained in a highly purified form was further purified by passage through a B.O.C. rare gas purifier to reduce quantities of hydrogen, oxygen, CO, CO_2 and hydrocarbons to below 1ppm. The removal of hydrogen and hydrocarbon impurities from the growth atmosphere is highly desirable when preparing samples for neutron scattering owing to the large incoherent hydrogen cross section that can obscure detail. Zr and Mn are excellent atmospheric getters and readily absorb oxygen as an impurity necessitating the greatest care to reduce oxygen levels to a minimum.

The system was flushed a minimum of 10 times before finally sealing in order to remove adhered impurities on the chamber walls

and the copper boat.

To further ensure atmospheric purity a piece of Zr was initially heated independently to getter the atmosphere prior to melting the sample constituent elements.

The growth of MnSi from its elements presented further hurdles. Again one of the components has a large vapour pressure (Mn $\approx$ 1mmHg at 1000^{0}C) making the use of an argon gas atmosphere essential. In addition silicon cannot be heated by RF induction because of its nonmetallic nature. Mn was therefore placed on top of the Si and melted into it. The resultant system is metallic and in addition may be heated in a vacuum, unlike $ZrFe_2$ that still evaporates differentially. The melting of Mn into Si is performed as quickly as possible to reduce Mn evaporation. MnSi is a line compound, that is the phase diagram (figure 3.2) has no width to the line joining the melting point to the room temperature points for the 50:50 composition. The use of zone refining to improve sample quality is thus an available option and in addition may be performed under vacuum.

3.4 The Atmosphere Quality

If all impurities are assumed to originate from the in leaking of atmospheric gases an upper bound for this type of contamination to the metal sample may be calculated.

The pumping rate of the turbomolecular pump used to obtain a

Figure 3.2 Mn-Si phase diagram taken from Shrunk 1969 -Constitution of Binary Alloys (second supp.), New York:McGraw-Hill page 507.

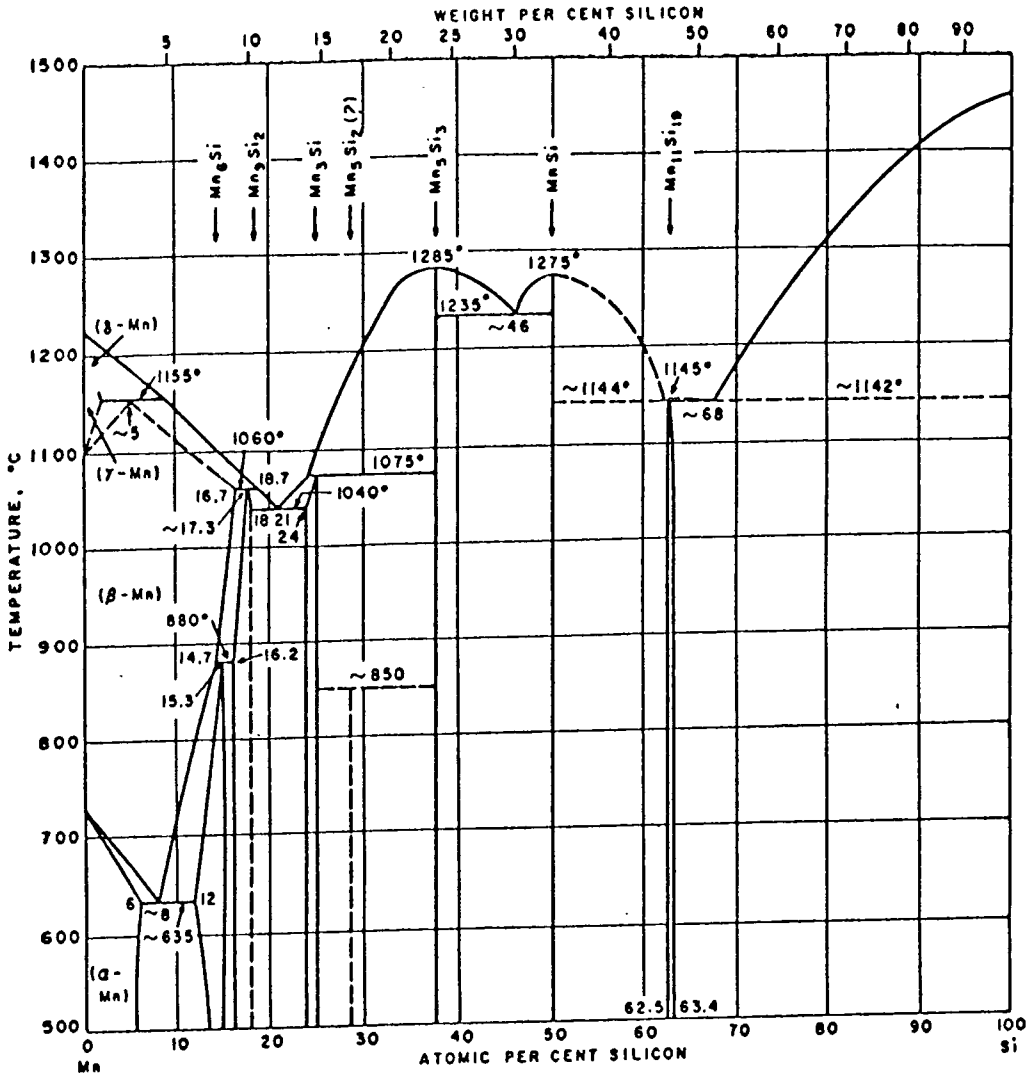
WEIGHT PER CENT SILICON
5 10 15 20 25 30 40 50 60 70 80 90
1500
1400
1300
1200
1100
1000
900
800
700
600
500
TEMPERATURE, °C
Mn6Si
Mn5Si2
Mn3Si
Mn5Si2 (?)
Mn5Si3
MnSi
Mn11Si19
1285°
1275°
1235°
~46
(δ-Mn)
1155°
~1144°
1145°
~1142°
~68
~5
1060°
1075°
(γ-Mn)
18.7
16.7
1040°
~17.3
18 21
24
(β-Mn)
880°
14.7
16.2
~850
15.3
6
~8
12
~635
(α-Mn)
62.5
63.4
0
Mn
10 20 30 40 50 60 70 80 90
100
Si
ATOMIC PER CENT SILICON

Figure 3.2

system vacuum of 10^{-7}mbar is 150l/s. The system chamber has a volume close to 2l. The leak rate assuming all residual pressure is caused by the in leaking of atmospheric gases is calculated as $1.5x10^{-5}$mbar/l. This assumption is not entirely accurate, no account being given to chamber out gassing. However a contamination level based upon this naive model for a 0.1mole sample that interacts with all system gas impurities over a growth cycle of 5 days of less than 100ppm of oxygen is predicted.

Light gases are not pumped as efficiently as oxygen and may result in higher contamination. With an over pressure of argon in leaking is significantly reduced and the above prediction is very much an upper limit of potential contamination.

3.5 The Preparation and Growth of Materials

For the studies carried out in this thesis two distinct material types have been prepared. For determination of the magnetic density distribution using polarised neutron scattering (Chapter 4) a single crystal of $ZrFe_2$ was required whilst for the study of MnSi under pressure using small angle scattering a polycrystalline sample was used. (Other samples used in this work have been generously supplied by other groups). For the growth of MnSi the zone refining material enhancement technique was employed. This promotes order and purity in the specimen.

3.6 Preparation of $ZrFe_2$

Zr and Fe were obtained from Johnson Matthey in specpure form. These were first etched to the correct masses using $HF:HNO_3:H_2O$ 5:45:50 for Zr and $C_2H_5OH:HNO_3$ 90:10 for Fe. Both samples were then washed thoroughly in distilled water before placing on the cleaned copper boat. The copper boat was prepared by cleaning with water, emery cloth and diamond paste before washing in soapy water and finally cleaning in distilled water.

The boat was then sealed and flushed a minimum of 10 times with argon, pumping out between cycles using a backing pump. The system was ultimately left at 10 psi over pressure of argon. From the phase diagram of $ZrFe_2$ it can be seen that much emphasis must be placed on the growth of a stoichiometric sample. The system is not a line compound (Figure 3.3) and as such the zone refining technique, although able to remove impurities will also result in a probably off stoichiometric alloy. Thus a simplified method was used without purity enhancement methods.

The constituents were melted together at 1650°C and mixed thoroughly using the natural stirring property of R.F. induction heating. Because of differential evaporation the elevated temperature of the molten mixing state was held for a relatively short period. The use of R.F. induction heating proved ideal as

Figure 3.3 Zr-Fe phase diagram. Notice the $ZrFe_2$ phase is not a line compound. Moffatt W.G. , 1984, The Handbook of Binary Phase Diagrams Volume 1, Genium Publishing.

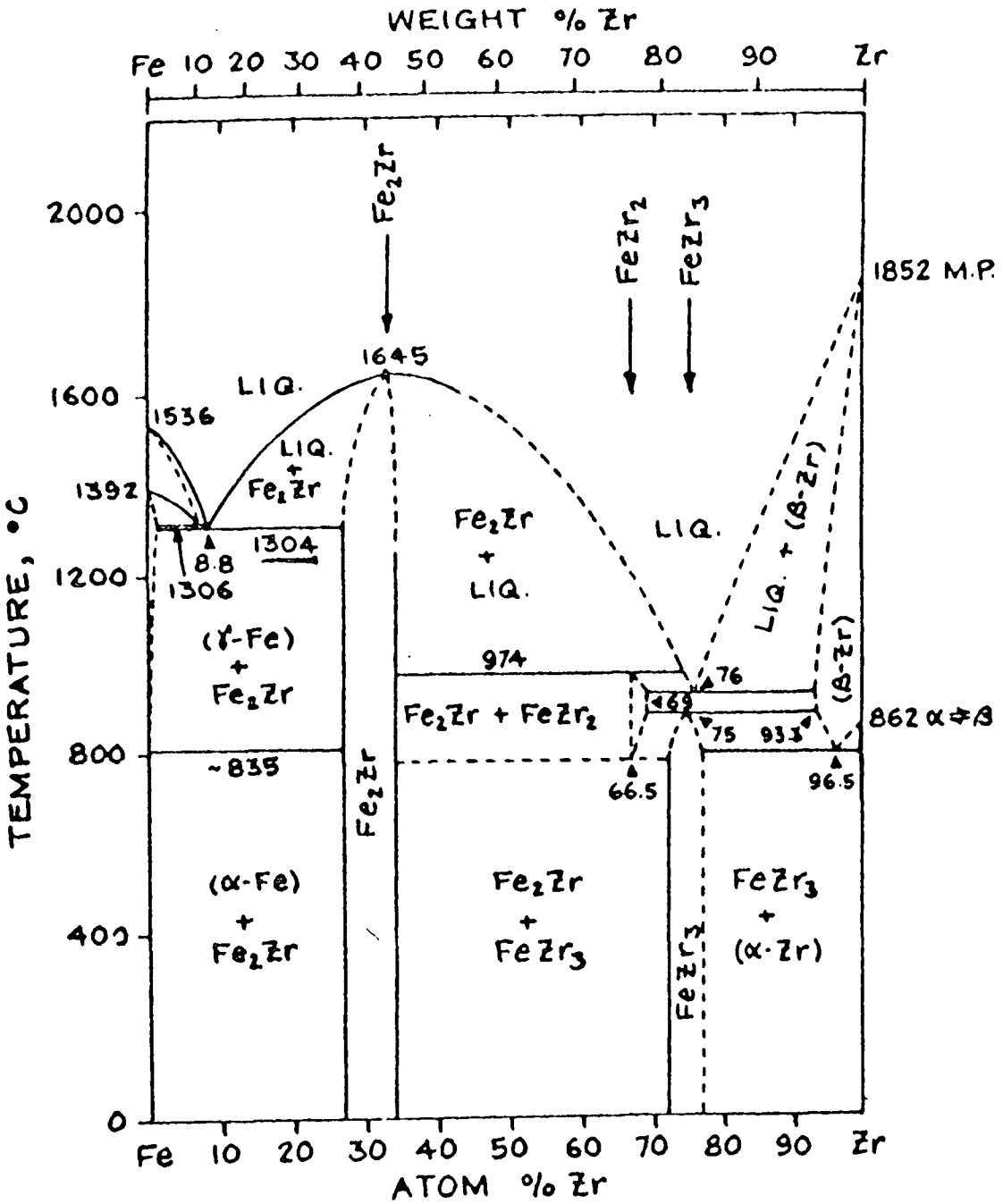
WEIGHT % Zr
Fe 10 20 30 40 50 60 70 80 90 Zr
2000
1600
1200
800
400
0
TEMPERATURE, °C
Fe₂Zr
FeZr₂
FeZr₃
1852 M.P.
1645
LIQ.
1536
LIQ. + Fe₂Zr
1392
1304
8.8
1306
(γ-Fe) + Fe₂Zr
~835
(α-Fe) + Fe₂Zr
Fe₂Zr + LIQ.
LIQ.
LIQ. + (β-Zr)
974
76
69
Fe₂Zr + FeZr₂
75
933
862 α⇌β
66.5
96.5
Fe₂Zr
Fe₂Zr + FeZr₃
FeZr₃
FeZr₃ + (α-Zr)
(β-Zr)
Fe 10 20 30 40 50 60 70 80 90 Zr
ATOM % Zr

Figure 3.3

the natural electromagnetic stirring capability meant that there was no need to wait for natural diffusion processes to occur which may have taken an extended period.

The charge was then left at 1500^{0}C for 3 days to anneal before cooling over a 24 hour period. These conditions were chosen after much observation and many such growth cycles.

Using this method 3 single crystals of $ZrFe_2$ were prepared with dimensions of the order of 2.5mm x .75mm x .5mm.

3.7 Details of Crystal Growth of $ZrFe_2$

The constituents were brought to 1650°C over a period of 15 minutes to allow for natural intermediate phases to occur with minimum stress.

Problems arose with the charge held at around 700°C. A reaction occurred capable of cracking the partially reacted metals and causing pieces to be removed from the bulk of the material. This was put down to one of two possibilities. The first cause may have been a result of an exothermic reaction of the two constituents whilst the second may have been a product of electromagnetic repulsion of boat and sample seen to occur at a set power level of the R.F. coils. Whatever the cause this problem was alleviated by the use of a carefully chosen R.F. coil initially to heat the constituents and by bringing the charge quickly through 700°C to about 950°C before bringing gradually to

a molten state.

The metals were then left to homogenise for 5 minutes at 1650°C before cooling to 1500°C. After 3 days of annealing and a slow cool the resultant polycrystalline ingot was cut along its length using spark erosion, polished and etched using ferric chloride solution. The etch proved excellent in revealing grain contrast.

Using the Laue back reflection X-ray technique large crystals observed from the surface were orientated so that the $[1\bar{1}0]$ direction was vertical, before cutting out again using a spark machine. The crystals were finally polished to produce a clean sample for neutron scattering.

In using this technique for the removal of crystals from the bulk material one can never be sure that the final cut is a single crystal as required. It may have voids or internal inclusions of the same or different phase. The neutron scattering experiments, detailed later in this work, reveal the samples obtained in this manner to have excellent characteristics and to be single crystals.

Further to this a measure of the residual resistance ratio can provide an indication of the level of purity and order disorder in the system. That is the ratio of resistances at 4.2K and room temperature ($RRR=\rho(293K)/\rho(4.2K)$). From Matthesian's law it is known that the scattering of conduction electrons from

impurities is temperature independent whilst scattering from phonon modes fall to zero at low temperatures. An indication of the impurity level of the sample may be inferred from the measurement.

The RRR cannot give an absolute indication of the impurity concentration within a specimen and must be compared to similar measurements taken on much studied materials. Similar systems which are also not line compounds such as Ni_3Ga and $ZrZn_2$ have RRRs of between 40 and 100 for the best quality samples ever produced whilst MnSi shows rather higher values of upto 230[36] owing to an anomaly in the resitivity as a function of temperature[87].

Since $ZrFe_2$ has a simple cubic structure similar to those of $ZrZn_2$ and Ni_3Ga a value of the RRR of around 90 obtained for the crystals gives strong evidence of a high quality product. The variation of $\rho(273K)/\rho(T)$ with temperature is shown in figure 3.4.

3.8 Annealing

The annealing stage of growth is of great importance. When samples are cooled through their melting point either as a whole, as in the case of $ZrFe_2$, or partially as in zone refining large order disorder occurs due to the stresses caused by the change of state. To promote the growth of a more highly ordered system and large single crystals the system is brought to a temperature just below the melting point of the bulk and left for an extended

Figure 3.4 The resistivity ratio $\rho(273K)/\rho(T)$ as a function of temperature (T) for a specimen of $ZrFe_2$ grown for neutron scattering investigation using the cold crucible technique. The measurements have been taken using a four point contact technique using custom built apparatus.

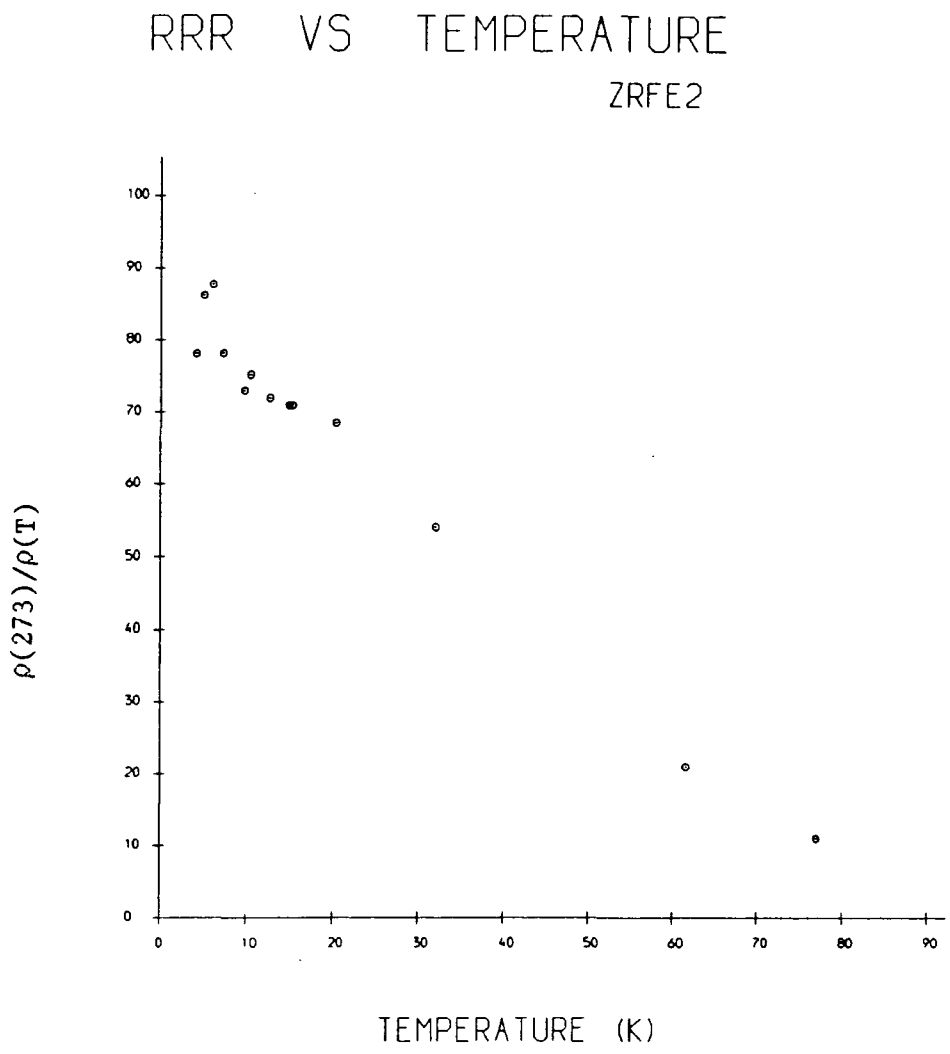
RRR VS TEMPERATURE
ZRFE2
ρ(273)/ρ(T)
100
90
80
70
60
50
40
30
20
10
0
0
10
20
30
40
50
60
70
80
90
TEMPERATURE (K)

Figure 3.4

period for growth to occur with a minimum of stress.

By heating the samples in a more homogeneous environment greater promotion of growth may be possible. The cold crucible provided a highly successful annealing environment in this work. The cold crucible may give rise to composition gradients as a result of the large temperature gradients if diffusion constants of the charge are not large enough to compensate. By the use of either a hot crucible or electric furnace greater homogeneity may be possible leading to the growth of larger single crystals.

3.9 Preparation of a MnSi Polycrystalline Sample

A polycrystalline sample was grown of the heli-magnetic material MnSi to study spin waves under pressure at low temperatures using small angle scattering on the D11 instrument at the I.L.L..

Whilst preparing the pure elements for growth great care was taken with the Mn which oxidizes very easily in air leading to great amounts of impurity in the final product. To reduce this potentially severe problem several precautions were observed. The Mn was only allowed to come into brief contact with the atmosphere whilst weighing (ideally this stage should be carried out in a glove box) and placing the sample on the cold crucible. At all other times the Mn was either kept under vacuum or in an inert gas atmosphere.

The Mn and Si were obtained from Johnson Matthey with purities quoted as 99.998% and 99.9999% respectively. The Mn was first etched in a dilute solution of HNO_3 and methanol and the Si in a mixture of HNO_3:glacial acetic acid:HF and bromide (50:30:30:0.6) before being thoroughly washing in distilled water. The constituents were weighed to within 50ppm of stoichiometric composition before removal to the cold crucible.

3.10 Zone Refining

During the growth of binary metal systems many potential problems are encountered with both the melt and solid. One problem occurring both in mixed and elemental growth crystal growth is inclusion of impurities found in the supplied raw material and, for single crystals, internal structure imperfections such as voids.

When attempting the growth of intermetallic systems additional problems arise. The levels of imperfection generally increases and the production of a highly stoichiometric sample become relevant. Inhomogeneities in the sample may occur due to incomplete mixing with disorder of the lattice resulting. Examples of this include the interstitial interchange of sites and a lack of long range order.

Several of these problems may be alleviated by the use of zone refinement. This method is used primarily to produce a cast ingot with a concentration gradient of major elements in the

system. In essence the technique moves excesses of one or more of the elements along the ingot leaving a highly stoichiometric 'good end' and a low quality 'bad end' by the unidirectional movement of a solid liquid interface.

The phase diagram for the Mn-Si (diagram 3.3) system shows that MnSi is a line compound. That is that the product MnSi forms from the melt with no uncertainty in composition. This implies that the solubility of extra atoms into solid MnSi is very small. However no such thing as an ideal line compound exists i.e. some width is always present on the cooling line and this results in some extra unwanted atoms dissolving into the solid phase.

When considering the zone refining technique it is usual to define the equilibrium coefficient K as the ratio of the concentration of the extra atoms in the solid to those in the liquid phases when solid and liquid are in thermodynamic equilibrium. This concept is important when discussing the merits of the zone refining technique.

For the MnSi alloy it can be observed from the phase diagram that the system is formed at the maximum between two eutectic points. This implies that $K<<1$ for either Mn or Si excess in MnSi. This is the general requirement for the unidirectional refinement techniques such as Bridgman[32], Czochralski[33] and zone refining to be effective.

To carry out the process of zone refining it must be possible

to heat a section about 10th of the ingot length above its melting point at any one time. Starting from one end this zone of melt is then moved slowly (1cm in 10 mins) along its length.

This process may be repeated with the movement of the interface always in the same direction along the sample. If one considers the first such pass along the length of the cast ingot a near stoichiometric phase is resultant in solid form and as the liquid solid interface moves so does the liquid excess that contains the in balance of either one or other of the material along with any impurities. This occurs due to the low solubility of this liquid material into the MnSi solid phase which is defined by the width of the line on the phase diagram joining the molten and room temperature equi-compositional states of the alloy. Each pass of the zone along the length of the ingot produces an increase in sample quality at the good end. The concentration gradient of impurities (c_s) after one pass of the zone is a function the initial uniform concentration (c_0) the effective distribution coefficient (K), the ratio m (total ingot length/heated zone length and the heated zone length (l)[34]. .

$$\frac{c_s}{c_0} = \{1-(1-K)\ \exp(-Km/l)\} \qquad 3.1$$

For a single pass the process is less efficient than the Bridgman cooling technique however on repeated application the zone refining technique yields a lower level of impurities over most of the ingot. Figure 3.5 shows the concentration

Figure 3.5 Approximate zone refining distribution curves for a system with k<1, an ingot length L=m x l and after n zone passes[34]. From Herrington E.F.G.- Zone Melting of organic Compounds 1963, Blackwell Scientific Publications.

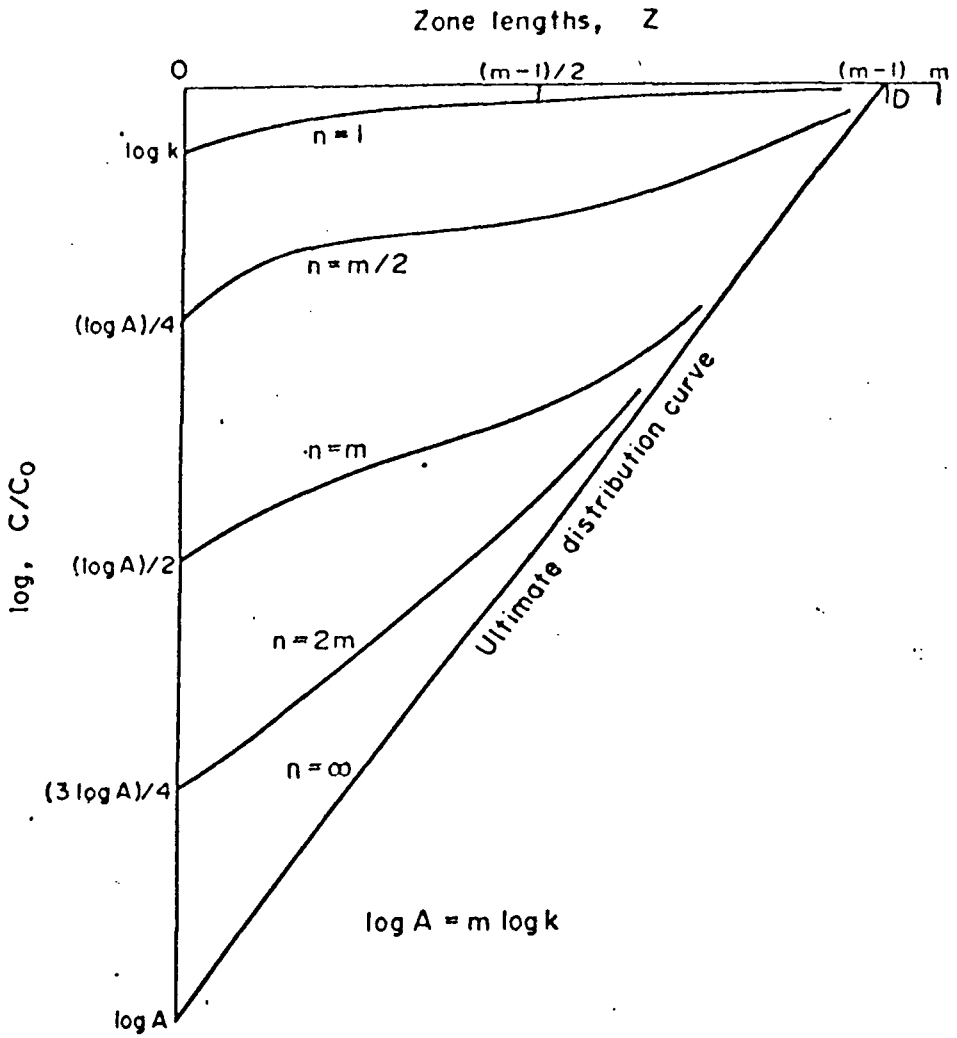

Number of passes n	Ultimate lowest concentration $\log c/c_0$
∞	$\log A$
$2m$	$(3 \log A)/4$
$m\ (= L/l)$	$(\log A)/2$
$m/2$	$(\log A)/4$
1	$\log k$

Figure 3.5

distribution variation with the number of passes and 1.

3.11 Final Stages Of Sample Preparation

Once zone refining was completed the metal ingot of MnSi was annealed for 2 days before removing. Three sections were then cut from the good end using a spark erosion machine. The zone refining technique results in the production of highly pure samples with no or little long range ordering due to the rapid quenching of sections of the ingot as the heating zone passes across it in addition large temperature gradients inherent in the cold boat method result in dislocations due to stress. Each cut section in turn was then submitted to mechanical stress using silver steel cylinders to clamp the samples in a vice. This technique was employed to reduce the crystal sizes still further as a fine polycrystalline sample was required for the small angle neutron scatting experiments. These samples where then annealed for 24 hours at 800°C to promote a small degree of order and to reduce residual stresses.

Before the final annealing stage slivers of the sample were cut from the ingot. These slithers were etched to clean and then used to determine the residual resistance ratio. A value of 80 was obtained from these measurements. This compares favourably with samples used for other neutron scattering experiments[35], however this is unfavourable compared to RRR measured by L. Taillefer[36] on large single crystals of 230. This difference is thought to be due largely to the difference in sample morphology.

To further increase the sample quality purification of the starting products would be necessary. The Mn in particular shows high levels of non metallic impurities. The final zoned ingot was green at the 'bad end' indicating a high level of sulphur impurity. The Mn would have to be zone refined before combination with the silicon to improve thus situation. Further improvements could be made to the zone refining process by the use of a finer R.F. coil to produce a more uniform compact area of melt.

CHAPTER 4

Bulk Magnetisation Measurements

Bulk magnetisation measurements on $TiBe_{1.5}Cu_{0.5}$ and $ZrFe_2$ have been carried out using a vibrating sample magnetometer (VSM).

The measurements have been performed to obtain the value of $X^{-1}(T)$ in the low field limit above the Curie Temperature and $X_{\parallel}^{-1}(T)$ below. The form of the function $X^{-1}(T)$ is necessary to the complete description of the model analysis for the small angle scattering investigations of $TiBe_{1.5}Cu_{0.5}$ in the paramagnetic regime whilst $X_{\parallel}^{-1}(T)$ enables longitudinal fluctuations to be included in the theoretical response in the ferromagnetic phase. In addition the values of the magnetic moments per atom in a zero (B=0) field at 0K have been found by extrapolation of finite field and temperature measurements. The zero field magnetisation scales the small angle scattering theoretical cross section below the Curie temperature to enable comparison to the collected data whilst for the polarised diffraction experiments on $ZrFe_2$ it provides a value of the q=0 magnetic structure factor f(000) that governs the low q shape of the form factor. Literature values have not been used in the present work as they may be sample dependent.

4.1 The Magnetic Equation of State

It is generally known that the observed magnetic properties of structurally ordered materials may be represented both in the ferromagnetic and paramagnetic phases by[37,16].

$$B = A(T)\, M(T,B) + bM^3(T,B) \qquad 4.1$$

$$A = a + b \left| 3 \langle m_{\parallel}^2 \rangle + 2 \langle m_{\perp}^2 \rangle \right| + \ldots \qquad 4.2$$

Where $\langle m_{\parallel}^2 \rangle$ & $\langle m_{\perp}^2 \rangle$ are the thermal variances of the local magnetisation parallel and perpendicular to the average magnetisation M respectively. a and b are the basic parameters introduced in chapter 2 required to complement c and γ in providing a complete phenomenological description of scattering from magnetic fluctuations in weak itinerant ferromagnets.

A>0 in the paramagnetic regime and A<0 in the ferromagnetic phase.

In the ferromagnetic regime the bulk susceptibility components may be described by:

$$X_{\parallel}^{-1} = \frac{\partial B}{\partial M} = A + M\left(\frac{\partial A}{\partial M}\right) + 3bM^2 \qquad 4.3$$

$$X_{\perp}^{-1} = \frac{B}{M} = A + BM^2 \qquad 4.4$$

Whilst in the zero field limit

$$X_{\perp}^{1} = 0 = A + BM^{2} \qquad 4.5$$

and thus $A=-bM^{2}$

The longitudinal bulk susceptibility, in the limit $\left(\frac{\partial A}{\partial M}\right) \cong 0$ becomes

$$X_{\parallel}^{-1} = -2A \qquad 4.6$$

The value A can be found from bulk magnetisation experimental data by plotting the measured values of M^2 against B/M and extrapolating the straight line to the $M^2=0$ axis. Plots of M^2 against B/M are known as Arrot plots. Above T_c, $X^{-1} = A$.

The value of M(q=0,T=0) and thus the moment per atom is obtained from hysteresis curves (M against B) as the extrapolated large B field M response to the B=0 axis and corrected for finite temperature using $M(0,T) = M(0,0)\ (1-(T/T_c)^2)^{0.5}$. This technique is employed since the observed value of M(0,0) on the hysteresis curve is dependent upon the domain structure of the sample. In a small external field the domains begin to align, total alignment being achieved at a finite field B_s. In an ideal situation one would wish to study a single domain crystal. However this is not possible and the required measurement must be obtained by extrapolation of the acquired data above the field at which

alignment into a single domain occurs.

The study of $ZrFe_2$ using the VSM has been performed with a multi domain single crystal aligned with the magnetic field perpendicular to the $[1\bar{1}0]$ direction. This alignment has been chosen since it corresponds to the chosen orientation of the crystal in the cryomagnet on the polarised neutron diffractometer that produces a significant number of distinguishable reflections. This orientation also corresponds to an easy direction of $ZrFe_2$. The studied crystal has been cut to give a high aspect ratio in favour of this direction.

The $TiBe_{1.5}Cu_{0.5}$ sample was provided in the form of non uniform granules, small specimens have been selected for measurement that approximate to spherical samples or that have a high aspect ratios.

4.2 The Vibrating Sample Magnetometer

The vibrating sample magnetometer used in this work has been described in detail by Hoon and Wilcock[38].

In brief the VSM measures the magnetic moment of a sample at q=0. It achieves this by oscillating the sample at a constant frequency in a uniform magnetic field. Any change in the field external to the sample owing to the sample motion is picked up using the fixed coils placed in the magnetic field. As a direct result of Lenz's law the emf induced in the pickup coils is

proportional to the rate of change of flux at the coils caused by the vibrating sample. This results in the production of an A.C. voltage in the pickup coils that is directly proportional to the magnetic moment of the sample and its vibrational amplitude.

The pickup coil geometry is arranged in such a way that the sample is always within the saddle point of the detection and wired together to eliminate detection of mechanical oscillations that occur at the same frequency as the induced signal. The resulting signal is enhanced by the use of a phase sensitive detector to achieve a high ratio of signal to noise. The reference signal supplied to the phase sensitive detector comes from an induction signal of a pickup coil with a permanent magnet attached to the motor shaft (see figure 4.1).

The sample vibrates in the vertical plane inside a cryostat. The sample rod, driven by a electric motor and a double crank mechanism is located centrally inside the cryostat by the use of a PTFE bush. The whole assembly including the cryostat is located centrally in a plane perpendicular to the collinear arrangement of field and detection coils.

The sample rod is constructed from 7mm borosilicate glass which is wholly inside the cryostat. It is connected to the drive shaft by a custom built double diaphragm isolation attachment. The sample is attached to the PTFE holder that is itself attached to the glass rod using PTFE tape.

Figure 4.1 Schematic diagram of the vibrating sample magnetometer used in the study of sample bulk magnetism (q=0).

Figure 4.1

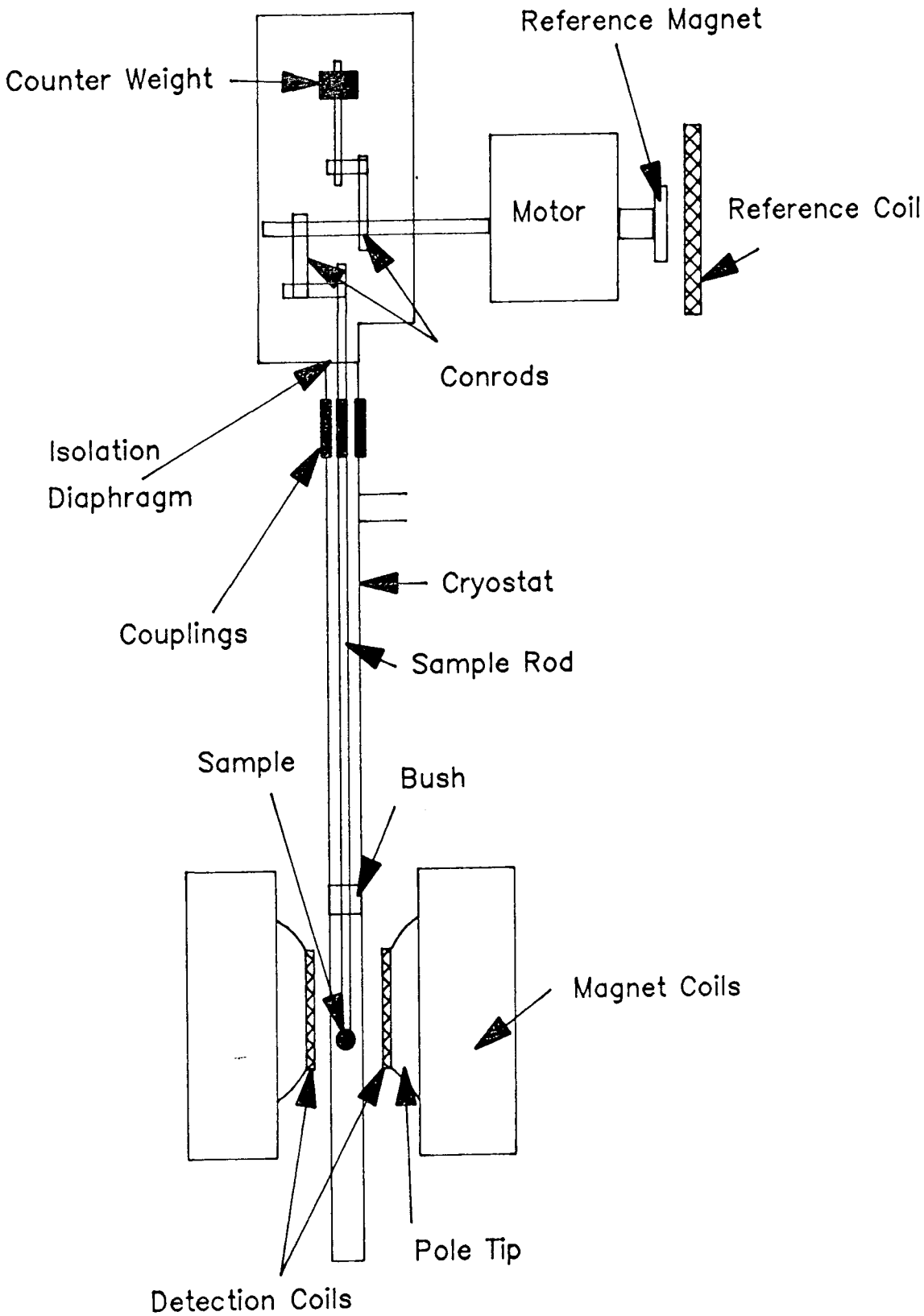
Reference Magnet
Counter Weight
Motor
Reference Coil
Conrods
Isolation
Diaphragm
Cryostat
Couplings
Sample Rod
Sample
Bush
Magnet Coils
Pole Tip
Detection Coils

The cryostat is a conventional Oxford Instrument CF1200 continuous flow type operating in the temperature range 4.2-200K. The temperature controller uses a gold 0.07 iron chromel thermocouple attached to the heater block on the base of the sample space and is accurate to 0.5K. This was calibrated against a Rh-Fe resistor, placed at the base of the sample space, with a reported[39] accuracy of 0.1K before data collection.

The applied external field produced by a conventional two pole magnet is cycled under computer control to fields of ±1.1 Tesla and monitored by a Hall effect gauss meter mounted adjacent to the cryostat in the magnet pole gap.

4.3 Calibration

An absolute measure of the magnetisation of the sample is made by calibrating the observed response of the VSM pickup voltage against a sample with a well known value of saturation magnetisation. For this purpose a spherical polycrystalline Nickel sample was used. The spherical shape of the calibration sample meant that the demagnetisation field was easy to calculate and corrected for.

By setting the external magnetic field to 1.1 Tesla and measuring the Ni response with temperature it has been documented that the shielding owing to the cryostat copper insert and heating block increases significantly below about 60K[39]. Measurements taken at low temperatures and calibrated against a room

temperature Ni standard have been accordingly corrected. The observed temperature dependent response for a nickel sample is shown in figure 4.2.

4.4 VSM Background Signal

The sample holder, made from PTFE, has a diamagnetic response to an external magnetic field. This behaviour has been removed from the sample measurements by the removal of an empty sample holder response with the magnetic field B. The actual deducted background is that of a least squares fit to a straight line of the observed weak diamagnetic response.

4.5 Demagnetisation

All magnetic samples in an external magnetic field B_{app} experience a reduced internal field B_0 as a result of a demagnetising field. The effect is produced by an apparent surface pole distribution on the sample. The extent of the demagnetising field depends upon the sample shape and the magnetisation M of the sample. This is usually modeled using the demagnetisation factor D, where:

$$B_0 = B_{app} - \mu_0 DM \qquad 4.7$$

D may be calculated exactly for magnetically uniform ellipsoids and approximately for other uniform shapes. When M is small as in the case of $TiBe_{1.5}Cu_{0.5}$ the external and internal

Figure 4.2a The induced voltage in the pickup coils of the VSM for a nickel sample against temerature used as a calibration response

Figure 4.2b The hysteresis curve for the pure sample of nickel (RRR=2000) at 4.2K. Errors in the calibrated and corrected magnetisation have been quoted as under 5%[39].

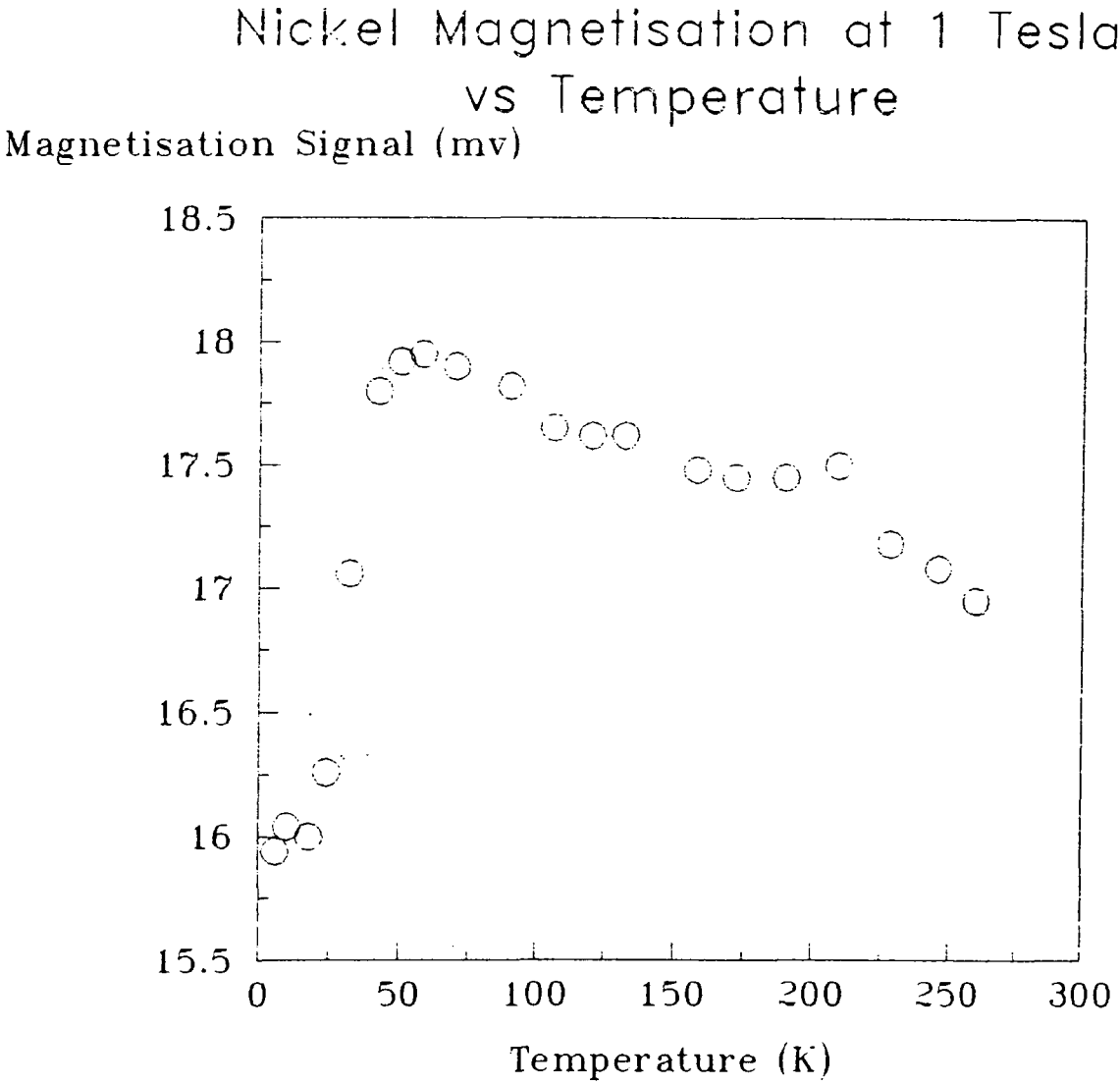
Nickel Magnetisation at 1 Tesla
vs Temperature
Magnetisation Signal (mv)
18.5
18
17.5
17
16.5
16
15.5
0
50
100
150
200
250
300
Temperature (K)

Figure 4.2a

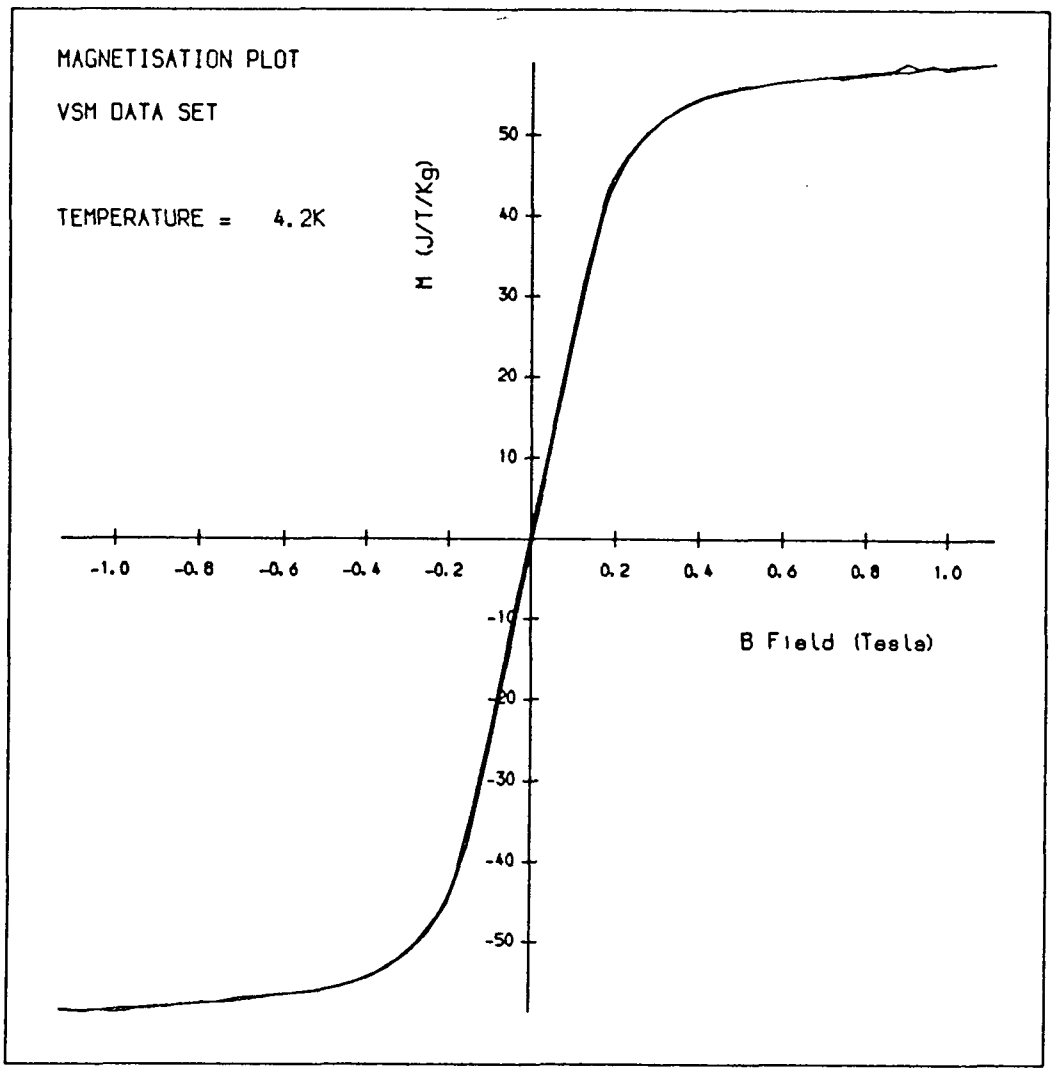
MAGNETISATION PLOT
VSM DATA SET
TEMPERATURE = 4.2K
M (J/T/Kg)
50
40
30
20
10
-10
-20
-30
-40
-50
-1.0
-0.8
-0.6
-0.4
-0.2
0.2
0.4
0.6
0.8
1.0
B Field (Tesla)

Figure 4.2b

fields are similar and the correction may be duly neglected.

For measurements where M is large the internal field is significantly different from the applied external field. This is the case for the $ZrFe_2$ sample. However the nature of the experiment requires the determination of M(0,T) for a single domain specimen, if the sample is saturated or close to saturation such that the magnetisation changes little for a change in field the effect of demagnetisation upon the measurement of M(0,T) is nulled.

4.6 Results

The $TiBe_{1.5}Cu_{0.5}$ system exhibits a paramagnetic response above a temperature of ≈28K and a bulk ferromagnetic state below this temperature. Hysteresis curves of magnetisation against magnetic field are shown for the system at temperatures of 4.2, 16.9,27.5,29.1 and 35K in figures 4.3. The data has been reploted in the form of an Arrot plot and is shown in figure 4.4. From the straight line relationships the bulk susceptibility has been calculated as described previously. The change of X^{-1} with temperature above T_c and $X_{\parallel}^{-1}$ below is shown in figure 4.5.

A hysteresis curve for $ZrFe_2$ is shown in figure 4.6 for the system at 140K. The measured zero field moments in Bohr magnetons and measured magnetic transitions are shown.

	M(0,0)	T_c
$ZrFe_2$	$3.26(15)\mu_B$ per formula unit	*
$TiBe_{1.5}Cu_{0.5}$	$0.22(1)\mu_B$ per formula unit	27.5K

* - T_c above room temperature.

Figure 4.3 The magnetic response (M(B,q=0)) of $TiBe_{1.5}Cu_{0.5}$ at (a) 4.2K, (b) 16.9K, (c) 27.5K, (d) 29.1K (e) 35K. Uncertainty in M is under 5%, less than 1% for B and ±0.5K in temperature.

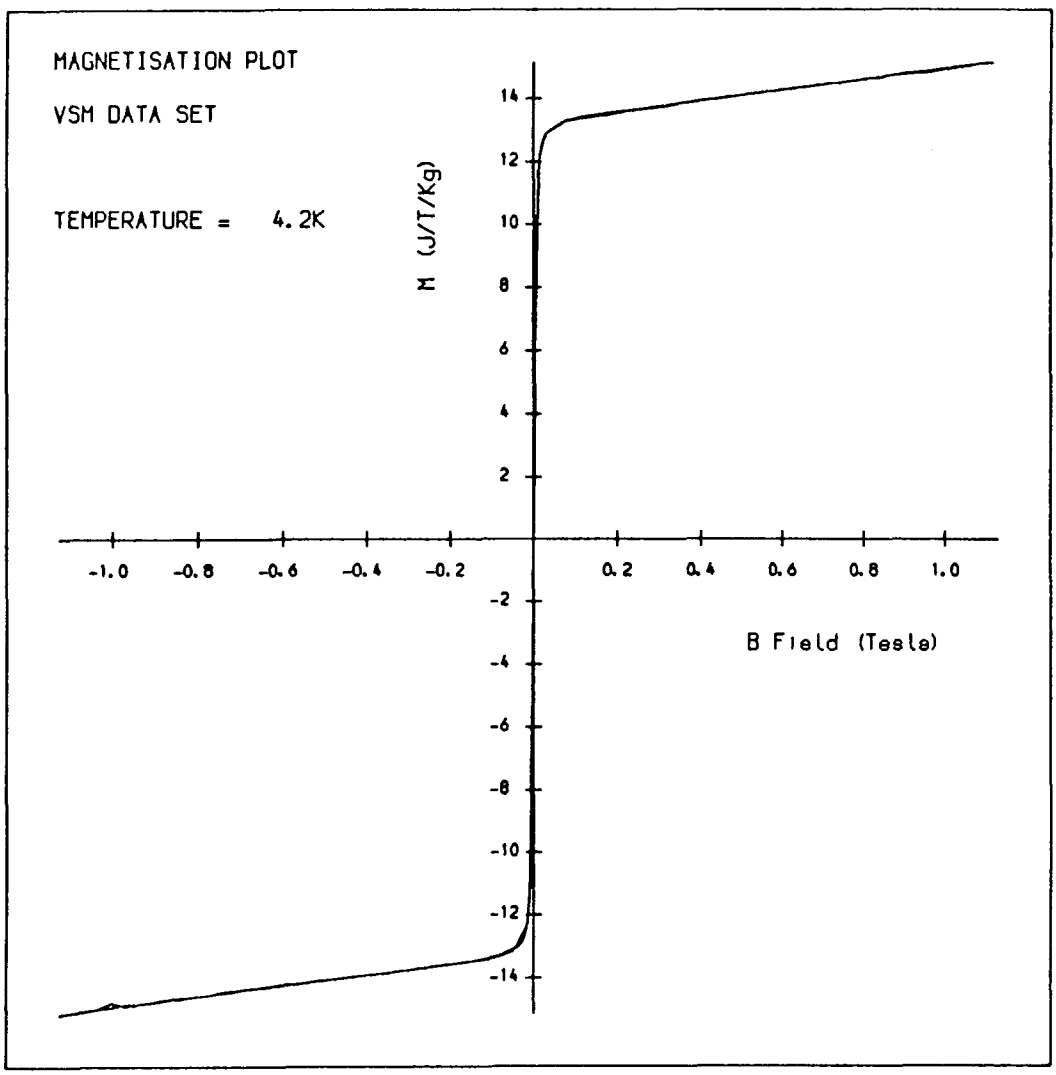
MAGNETISATION PLOT
VSM DATA SET
TEMPERATURE = 4.2K
M (J/T/Kg)
14
12
10
8
6
4
2
-2
-4
-6
-8
-10
-12
-14
-1.0
-0.8
-0.6
-0.4
-0.2
0.2
0.4
0.6
0.8
1.0
B Field (Tesla)

Figure 4.3a

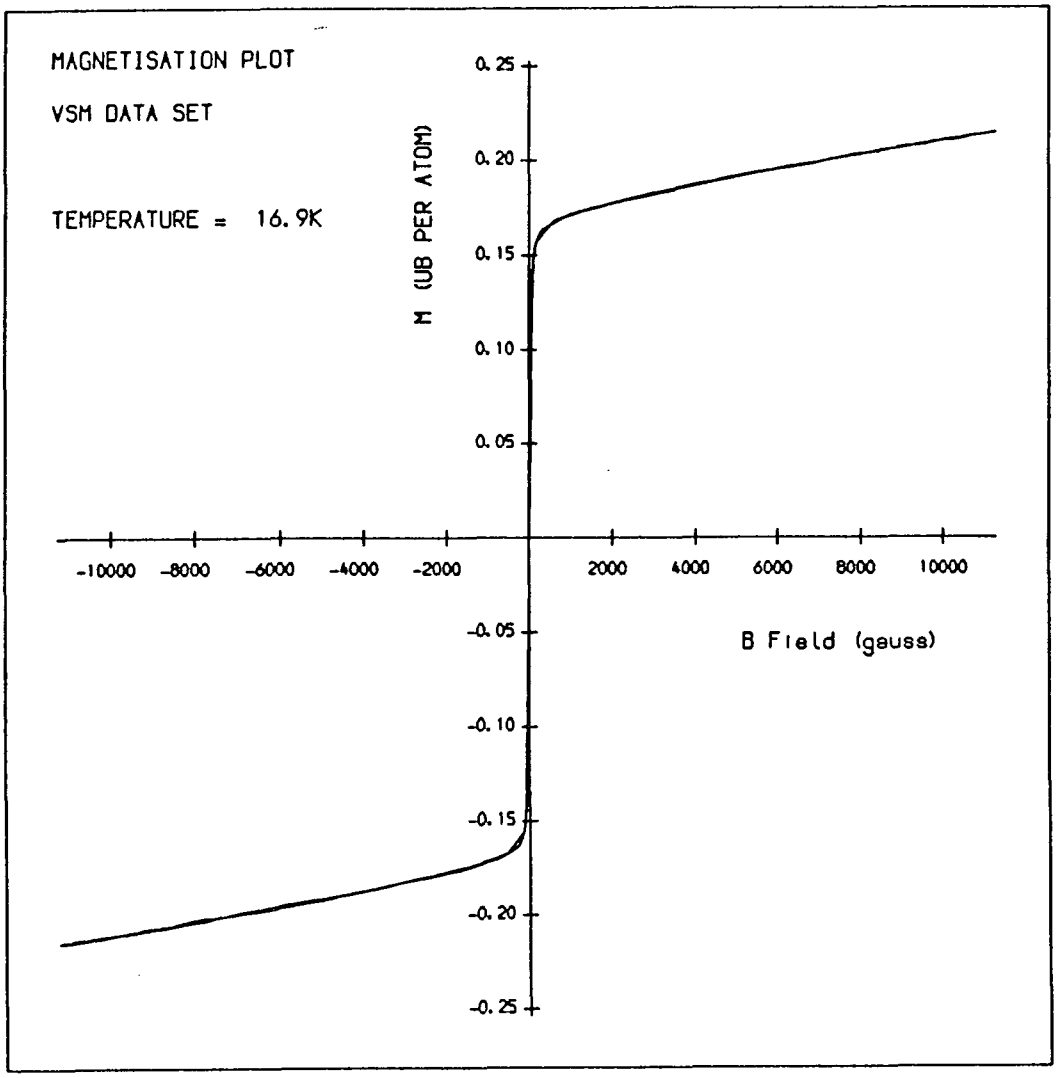
MAGNETISATION PLOT
VSM DATA SET
TEMPERATURE = 16.9K
M (UB PER ATOM)
0.25
0.20
0.15
0.10
0.05
-0.05
-0.10
-0.15
-0.20
-0.25
-10000
-8000
-6000
-4000
-2000
2000
4000
6000
8000
10000
B Field (gauss)

Figure 4.3b

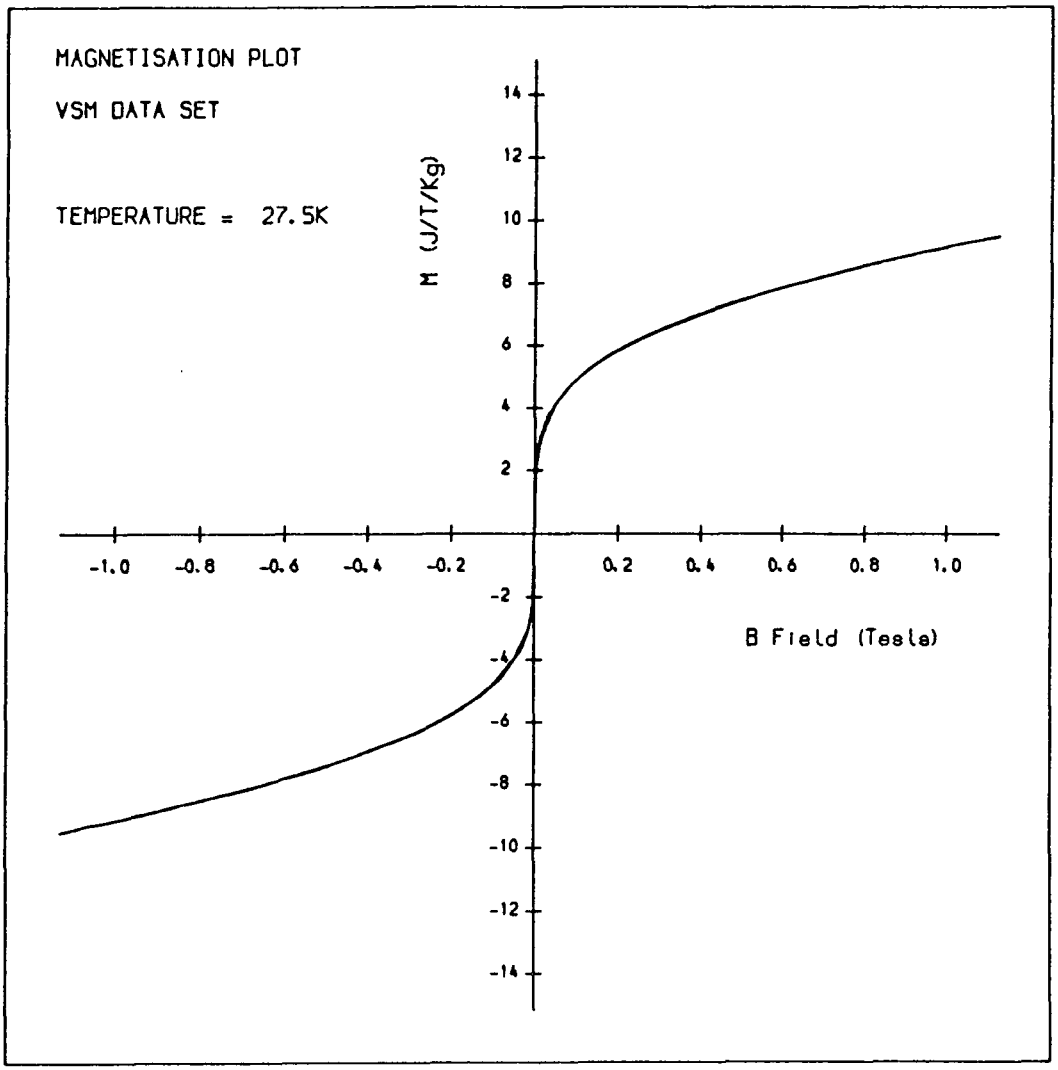
MAGNETISATION PLOT
VSM DATA SET
TEMPERATURE = 27.5K
M (J/T/Kg)
14
12
10
8
6
4
2
-2
-4
-6
-8
-10
-12
-14
-1.0
-0.8
-0.6
-0.4
-0.2
0.2
0.4
0.6
0.8
1.0
B Field (Tesla)

Figure 4.3c

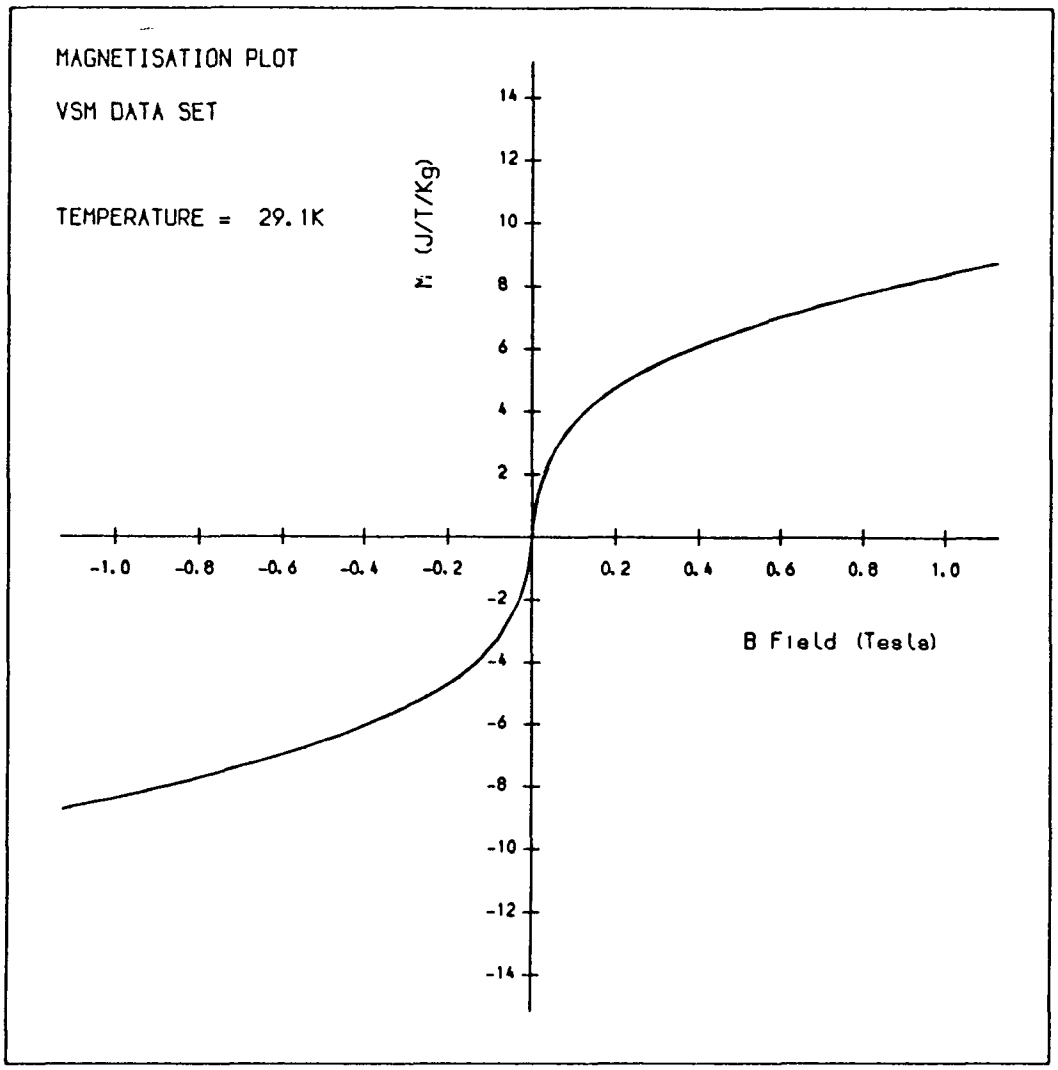
MAGNETISATION PLOT
VSM DATA SET
TEMPERATURE = 29.1K
M (J/T/Kg)
14
12
10
8
6
4
2
-2
-4
-6
-8
-10
-12
-14
-1.0
-0.8
-0.6
-0.4
-0.2
0.2
0.4
0.6
0.8
1.0
B Field (Tesla)

Figure 4.3d

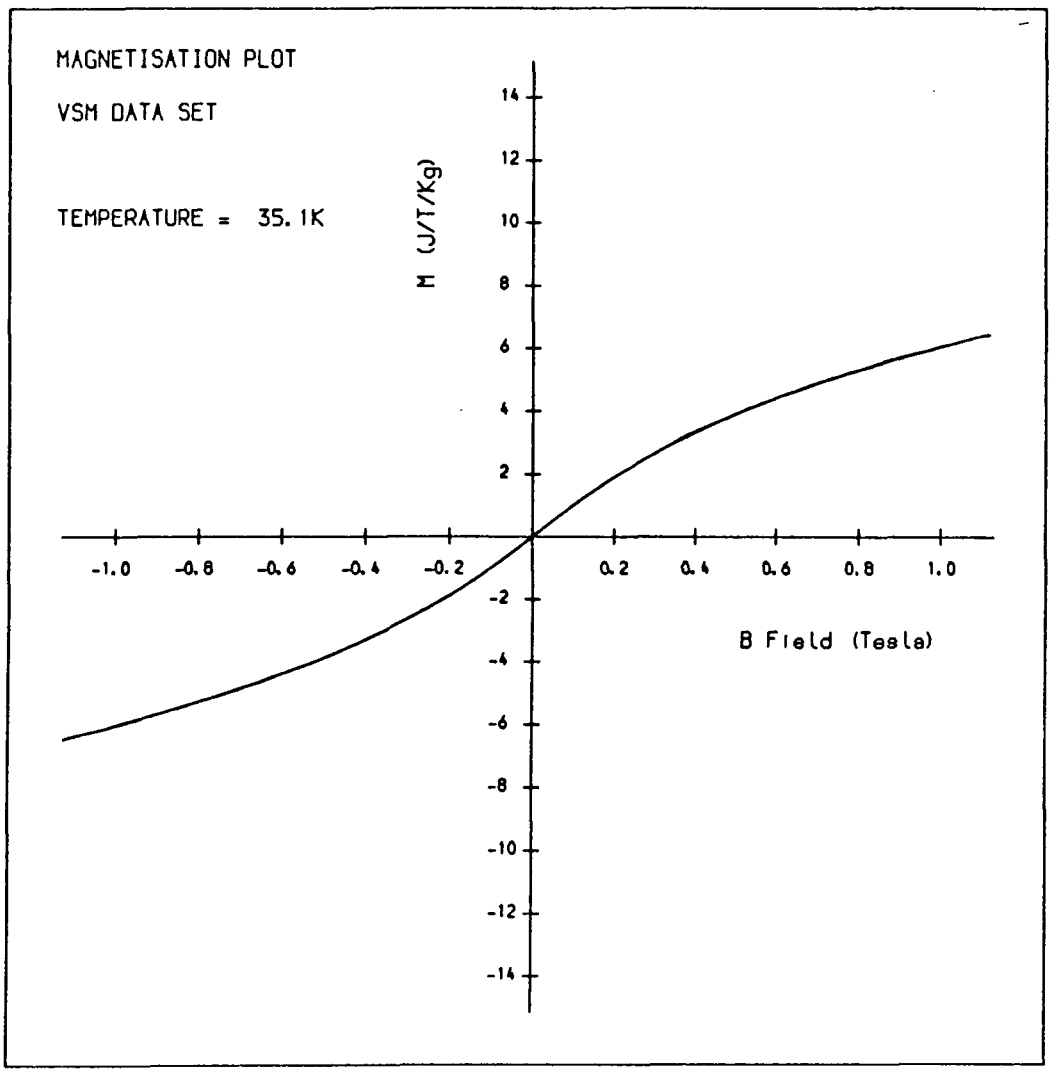
MAGNETISATION PLOT
VSM DATA SET
TEMPERATURE = 35.1K
M (J/T/Kg)
14
12
10
8
6
4
2
-2
-4
-6
-8
-10
-12
-14
-1.0
-0.8
-0.6
-0.4
-0.2
0.2
0.4
0.6
0.8
1.0
B Field (Tesla)

Figure 4.3e

Figure 4.4 Arrot plot of the VSM data [$M^2(\mu_B/atom)^2$ against B/M (gauss/μ_B)].

Figure 4.5 $X^{-1}(T)$ predicted from the intercepts of the Arrot plot best fit lines with the $M^2=0$ axis.

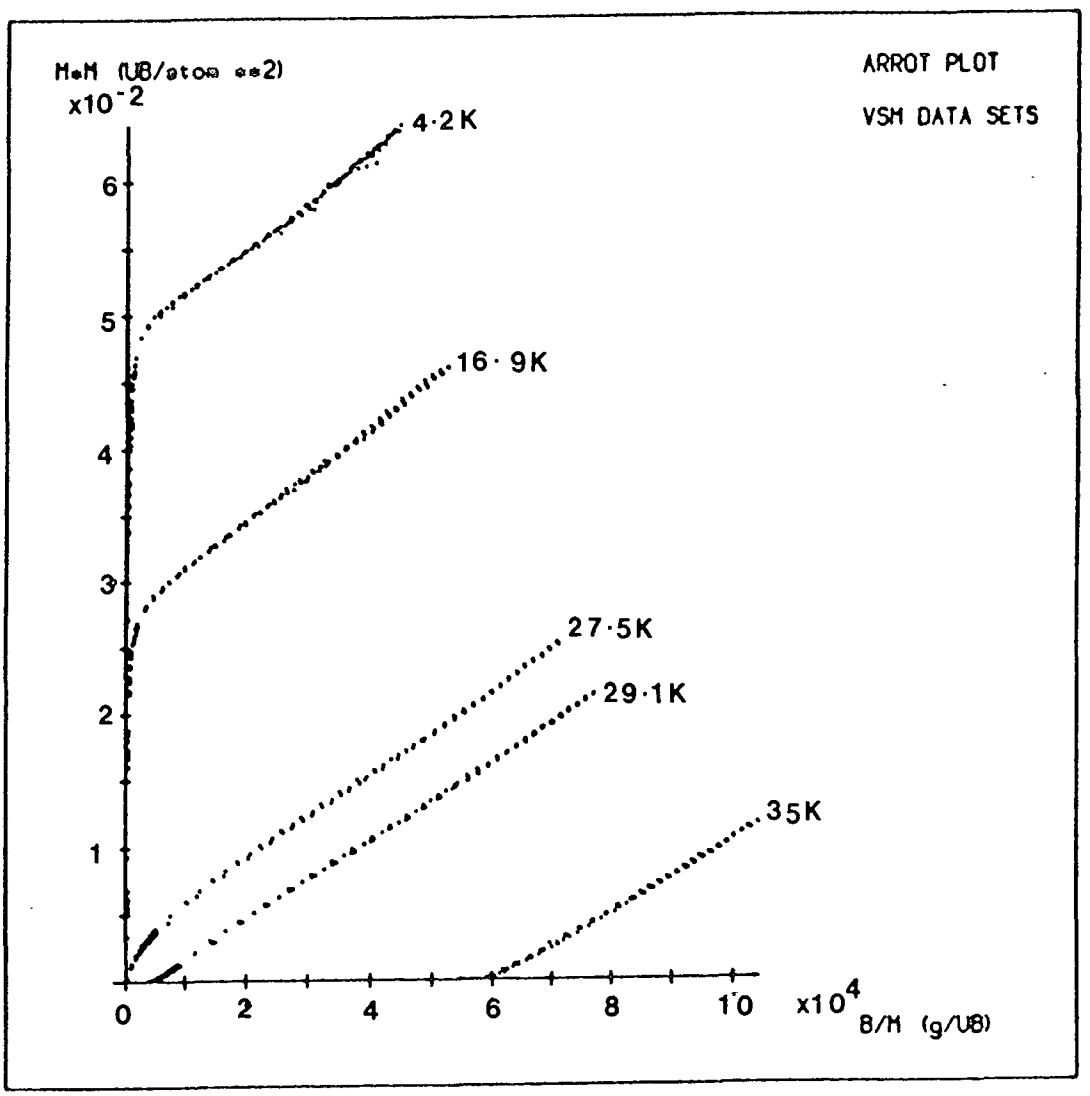
M•M (UB/atom ••2)
x10^-2
ARROT PLOT
VSM DATA SETS
4·2K
16·9K
27·5K
29·1K
35K
6
5
4
3
2
1
0
2
4
6
8
10
x10^4
B/M (g/UB)

Figure 4.4

Figure 4.5

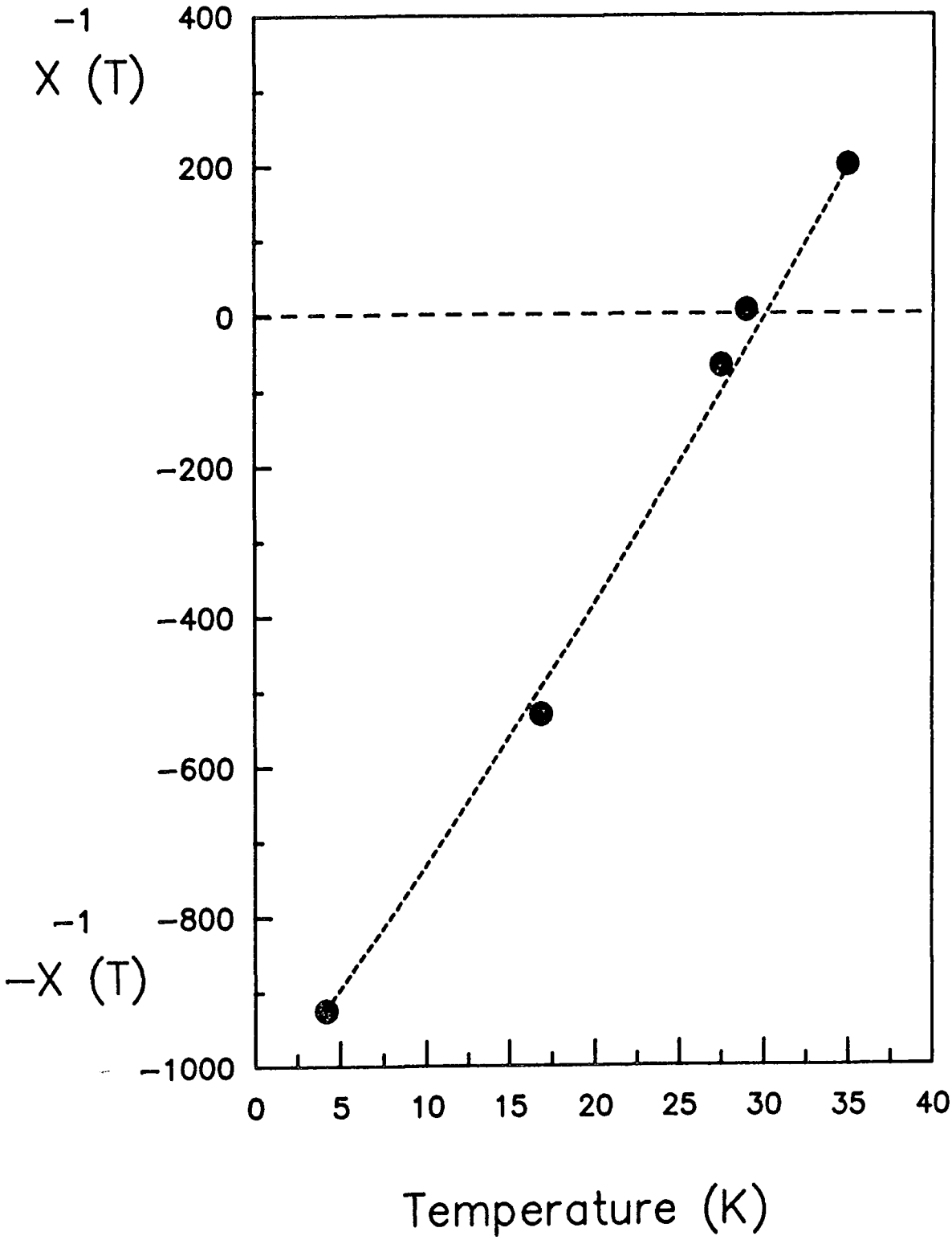
-1
X (T)
400
200
0
-200
-400
-600
-800
-1000
-1
-X (T)
0
5
10
15
20
25
30
35
40
Temperature (K)

Figure 4.6 Hysteresis curve for a single crystal sample of $ZrFe_2$. The extrapolation of the magnetisation to the B=0 axis, above domain alignment, predicts a magnetic moment of $1.63(7)\mu_B$ per Fe atom.

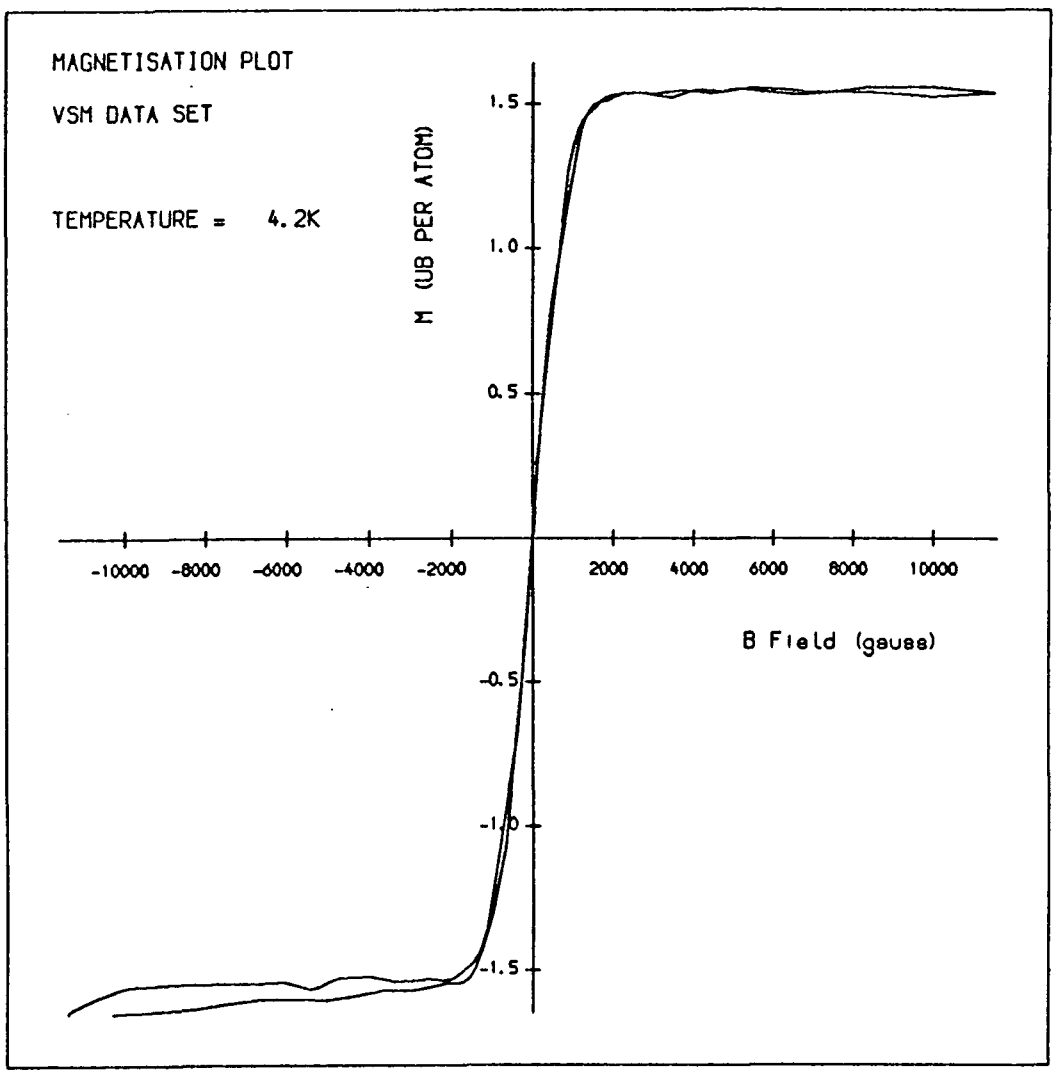
MAGNETISATION PLOT
VSM DATA SET
TEMPERATURE = 4.2K
M (UB PER ATOM)
1.5
1.0
0.5
-0.5
-1.0
-1.5
-10000
-8000
-6000
-4000
-2000
2000
4000
6000
8000
10000
B Field (gauss)

Figure 4.6

CHAPTER 5

Spin Density Fluctuations in $TiBe_{1.5}Cu_{0.5}$

5.1 The Parent Compound $TiBe_2$

The magnetic nature of the binary metal alloy $TiBe_2$ has been the centre of a great deal of discussion, it being isostructural and isoelectronic to the well know weak itinerant ferromagnet $ZrZn_2$. $TiBe_2$ was originally assumed to be an ordered itinerant-electron magnet[40] but it is now generally agreed that it is best described as an enhanced paramagnet.

The first major interest in the compound was aroused following bulk magnetic investigations[41] and was followed by evidence of a flat magnetic susceptibility below about 20K with a smooth maximum at 10K[42] like that observed for Pd near 80K. By extrapolation of $X^{-1}(T)$ to T=0K the system shows a negative intercept and the compound was labelled antiferromagnetic. Neutron diffraction studies[43] and specific heat measurements[44] failed to establish the existence of a phase change. Later work[45,46,47] have converged to the existence of a strongly enhanced paramagnetic state at all temperatures.

5.2 The Copper Induced Ferromagnetic State

Unpublished work[48] predicted that with the substitution of a small quantity of copper atoms into the C15 cubic laves structure of $TiBe_2$ at Be atom sites ferromagnetic ordering might result, when the parent compound is considered as an enhanced paramagnet, from the data obtained in a previous experimental investigation[40]. This was indeed proved to be the case[49]. How and why this transition from an enhanced paramagnetic to ferromagnetic state should occur is not completely understood. An explanation offered by J. L. Smith is that a change in the density of states at the Fermi surface arises through an expansion of the lattice upon the introduction of Copper into the $TiBe_2$ lattice. This transition is by no means unique, Gadolinium substitution in YCo_2[50] and YCo_3[51] also reveal this type of behaviour. However the introduction of Gadolinium into $TiBe_2$ does not result in a ferromagnetically ordered state. The existence of a ferromagnetic ground state would thus appear to depend critically upon the induced density of states at the Fermi level.

It has been shown in the $TiBe_{1.8}Cu_{0.2}$ system using polarised neutron diffraction investigations[52], similar to those detailed elsewhere in this thesis, that the magnetic moment distribution originates from the Ti lattice positions and that a degree of delocalisation exists. Similar studies of the parent compound[53] reveal a similar magnetic moment distribution for a sample aligned in an external field of 4.6T. The addition of copper into the lattice may be likened to the application of an internal magnetic

field[37].

The transition from a paramagnetic to a ferromagnetic ground state as a function of copper substitution ($TiBe_{2-x}Cu_x$) has been studied using both bulk magnetic measurements (x_c=0.16)[49] and small angle neutron scattering[54] (x_c=0.07). This difference is probably due to sample heterogeneities and uneven distribution of copper in the sample resulting in different densities of states at the Fermi level in a system already close to the magnetic phase instability.

5.3 Sample Preparation

The material used in this study where provided by Felcher at the Argon Laboratories. It was prepared from the high purity elements Ti 99.99%, Cu 99.999% and Be 99.5% by arc melting in an argon atmosphere on a water cooled copper hearth. Ti-Cu alloy was first prepared by repeated arc melting to insure complete mixing. The correct weight of Be was then added and the product again repeatedly arc melted to insure complete homogeneity and stoichiometry. The samples were then powdered and analysed using room temperature Debeye-Scherer X-ray diffraction to confirm a C15 phase structure with the absence of or at least only a small amount of any second phase.

The use of an incident long wavelength monochromated neutron beam of the D11 instrument permits the study of polycrystalline samples. For the experiment polycrystalline pieces upto 3mm x 3mm

x 3mm in size were used to fill the D11 sample holder of dimensions 10mm thickness by 10mm diameter.

The measured RRR of these specimens is low at around 17 but since this system is in effect impure due to the random substitution of Cu atoms at Be atom sites it is quiet respectable when compared to RRR's quoted for $TiBe_2$ of 19[45,40].

5.4 The Observed Neutron Scattering Cross-Section

In Chapter 2 the theoretical neutron scattering cross section was discussed. To be able to compare collected intensity data as a function of scattering angle from the small angle scattering experiment collected data must first be corrected for background scattering, sample absorption, counter cell efficiency and finally calibrated.

Numerous background signals are present in any neutron scattering experiment. If they are not treated with care, especially in systems that show weak scattering, serious errors may result.

The background noise of any neutron experiment may be broken down into three possible sources.

(1) General noise from the counting system electronics.

(2) Stray neutrons from surrounding instruments and the

neutron source.

(3) Neutrons scattered from the incident beam eg. from the sample holder and cryostat tail.

Sources (1) and (2) contribute a flat response over the entire neutron spectrum and may be simply deducted from the scattering response if necessary.

To account for the background sources two scans are taken. The first is taken with an empty sample holder and the second with a neutron opaque material at the sample position, for this purpose cadmium is generally used (at low temperatures). From these two scans background sources may be obtained.

The difference between the empty cell (I_{ec}) and cadmium cell (I_{cd}) detector responses, that vary with counter cell position, corrected for sample transmission ($\alpha(T)$) provides a measure of the background attenuated by the sample under investigation. All unscattered neutrons either strike the beam stop (placed at zero angle directly in front of the detector) or pass to cells close to the detector centre and are ignored in the data analysis. The cadmium only scan provides a measure of the background of neutrons that reach the detector without passage through the sample. The corrected sample intensity ($I_{s,corr}$) may be calculated from the total observed intensity profile ($I_{s,total}$).

$$I_{s,corr} = I_{s,total} - I_{cd} - \alpha_s(T)\,(I_{ec} - I_{cd}) \qquad 5.1$$

This calculation does not provide correction for: (1) inelastically scattered neutrons prior to sample scattering and the resulting variation in sample attenuation; (2) neutrons scattered from the surroundings after sample scattering.

The sample transmission $\alpha_s(T)$ has been measured continuously with the aid of a modified beam stop with 5 small holes cut in it allowing a small fraction of the transmitted beam to be monitored by the detector cells directly behind the beam stop. The sample transmission of 0.368 was a good estimate over the entire temperature range under investigation.

Counter cell efficiency is measured by obtaining a scattering profile from a perspex sheet placed in the sample holder. Polymethylmethacrylate has a strong incoherent elastic scattering cross section permitting all cells to be scaled to a flat uniform response after any background corrections have been performed.

$$I_{plexi,i} = I_{plexi\ total,i} - I_{cd}(1-\alpha_{plexi}(T)) - \alpha_{plexi}(T)\, I_{ec} \qquad 5.2$$

at cell i.

To obtain an absolute calibration of the scattering cross section a vanadium sample is placed in the sample position and a scan taken. Vanadium has a large incoherent scattering cross section that dominates the total scattering with little if no

multiple scattering events provided that the sample is thin enough.

$$I_{van,i} = I_{van\ total,i} - I_{cd}(1-\alpha_{van}(T)) - \alpha_{van}(T)\ I_{ec} \quad 5.3$$

Correction is made to this for counter cell efficiency. A vanadium sample is not used to correct for cell efficiency itself because at low q anomalous scattering is observed believed to be the result of scattering from absorbed hydrogen unremoved during manufacture. Calibration of the data is obtained against an average response observed at high q where the response is flat.

In addition to the background corrections the total cross section includes contributions from sample dependent sources that should be considered. These include phonon, impurity, defect and incoherent nuclear scattering.

The low q regime of investigation means that phonon scattering contributions are small. The zero phonon modes are negligible since the chosen incident wavelength (8Å) is well beyond the Bragg cut off, likewise the single phonon absorption processes occur at large transfer energies well beyond the D11 spectrometer range of detection. Multiphonon and inelastic nuclear scattering provide a small k dependent contribution which are approximately temperature independent and may be corrected for by subtraction of a low temperature sample scan (1.5K in these measurements) corrected for background and scaled for sample transmission. Since there may still be a thermal dependent magnetic contribution at 1.5K this subtraction is in fact an over

subtraction. This has been considered by subtraction of a theoretical 1.5K magnetic scan from the modeled data.

The total observed cross section is given by:

$$\left(\frac{d\sigma}{d\Omega}\right)_s = \frac{I_s}{I_{van}}\left(\frac{\sigma_{inc}}{4\pi}\right)_{van}\frac{(N_a/V)_{van}}{(N_a/V)_s}\frac{A_{van}L_{van}\alpha_{van}(T)}{A_s\ L_s\ \alpha_s(T)} \qquad 5.4$$

Where

A_i = sample cross section perpendicular to the incident beam.

L_i = thickness of sample

α_i = sample transmission

and I_{van} and I_s have been corrected for counter efficiency.

$$I_s = I_{s,observed} \times \frac{\sum_i (P_i/n)}{P_i} \qquad 5.5$$

and $I_{van} = \sum_j V_j/n$ 5.6

P_i = detector counts at cell i (or groups of cells on a defined annulus)

V_j = detector counts at cell group j for scattering from a vanadium sample where j corresponds to large q where the scattering is a flat response.

5.5 Results

The temperature dependence of intensity difference data with a sample detector distance of 5m and an incident neutron wavelength of 8Å is shown in figure 5.1. That is a low temperature background scan has been removed. At such typical temperatures (1.5-2K) the magnetic scattering is small but finite giving a small temperature dependent offset to each point. The intensity falls away quickly above the Curie temperature , the model chosen must be able to predict this behavior. An additional test of the model is that unlike many others describing observed scattering[28,16,27], a single equation with the same basic parameters suffices to describe both the weak ferromagnetic and the paramagnetic phases.

5.5.1 Modeling with the SCR RPA Theory

The data collected below the Curie temperature at both sample detector distances (2.5 & 5m) were initially modeled using the two pole delta function line shape described by the SCR RPA. Empirical fits were attempted allowing the values of the spin wave stiffness and the energy gap to vary freely. The goodness of fit has been correlated using the Chi squared test and contour plots of this quantity with the parameters D and E_g used as an indicator to the best fit. Good fits to the data have been obtained over all observed q for all temperatures below T_c for data collected with a sample detector distance set at 5m. A value of the spin wave stiffness corrected to 0K of D=35±5 mevÅ^{-2} corresponding to a

Figure 5.1 Constant q, temperature dependence of observed intensity difference data of a $TiBe_{1.5}Cu_{0.5}$ sample taken on the small angle scattering spectrometer D11 with a sample-detector distance set at 5m and with an incident neutron wavelength of 8Å. This data has had a 1.5K background removed. The observed scattering intensity is directly proportional to the scattering cross section when all cells have equal counter efficiency.

Figure 5.1

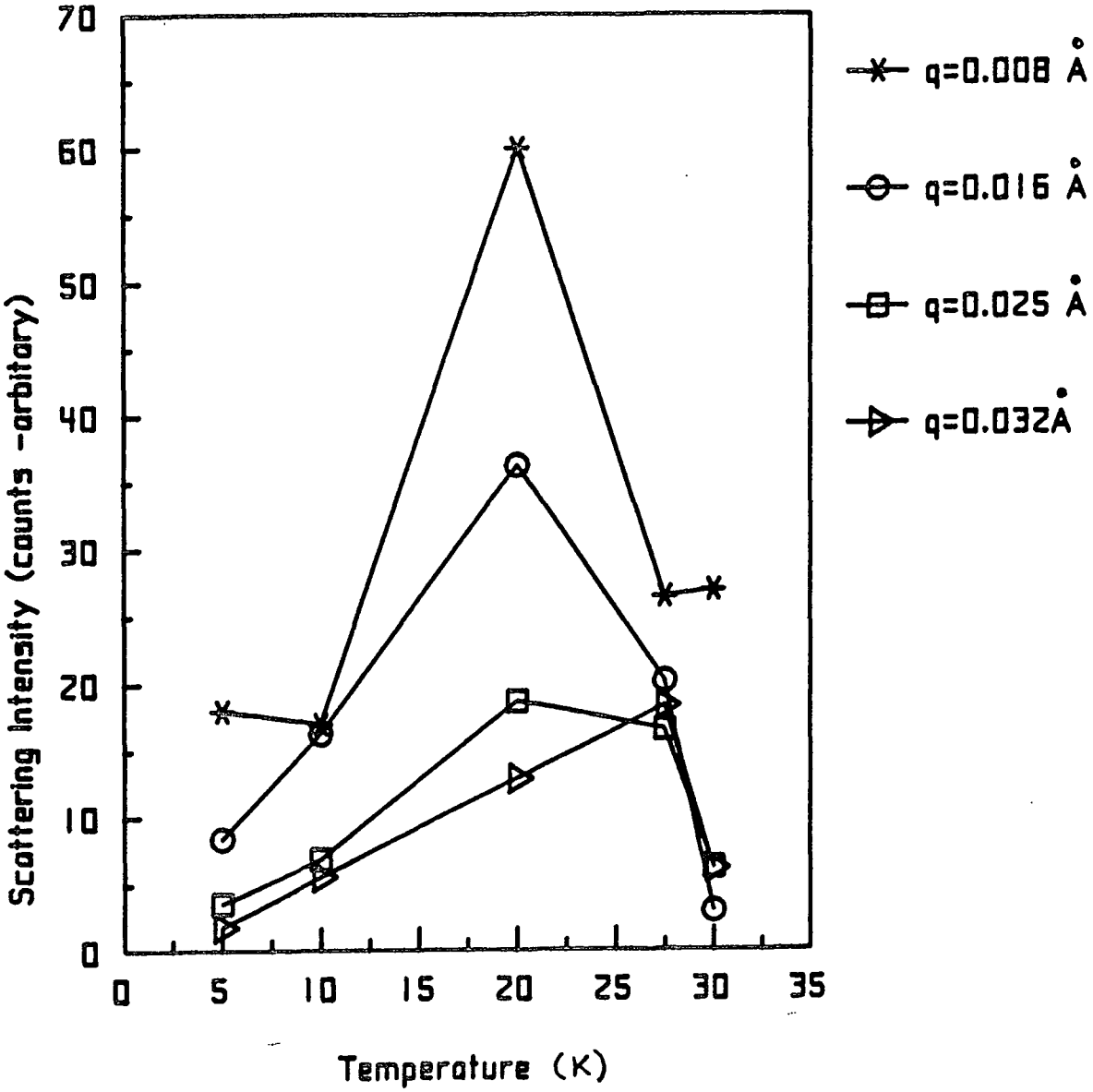
70
60
50
40
30
20
10
0
Scattering Intensity (counts -arbitary)
0
5
10
15
20
25
30
35
Temperature (K)
q=0.008 Å
q=0.016 Å
q=0.025 Å
q=0.032Å

critical cut off angle of 0.057 radians and an average energy gap of 7±3μev is obtained.

For data collected at higher q using the sample-detector distance of 2.5m the story is not the same. Whilst the cut off angle falls above the observed data (in q) for the 5m setting it falls well within the observable q_{el} range of the 2.5m setting. The discontinuity discussed in chapter 2 is predicted in the spectrum around θ_c whilst the intensity falls away quickly above this value only extending beyond the associated cut off due to the machine angular resolution. The difference between the observed and predicted values of scattering cross section at higher q is a good indication that scattering is occurring from damped spin wave modes.

5.5.2 The Damped Spin Wave Model

The inconsistency of the SCR RPA prediction at high q has been resolved using the two pole Lorentzian line shape model below the Curie temperature based on a generalised damped coupled harmonic oscillator. This model requires the use of three essentially independent parameters D(T), E_g and Γ the relaxation function. D(T) ,the spin wave stiffness, is the same as that defined in the SCR RPA description and Γ is the same function as that used in the description of diffuse scattering in the paramagnetic regime.

The energy gap term E_g is generally small compared to $D(T)q^2$

Figure 5.2 Contours showing the goodness of fit to experimental data of simulated cross section data based on the SCR RPA response function at 10K for an incident neutron wavelength of 8±0.6Å. The contour levels are directly proportional to the statistical goodness of fit parameter X^2 calculated from the observed and predicted data.

Magnetic scattering from longitudinal spin fluctuations are not included in the predicted data as they have been calculated as adding only a negligible quantity to the total scattering cross section.

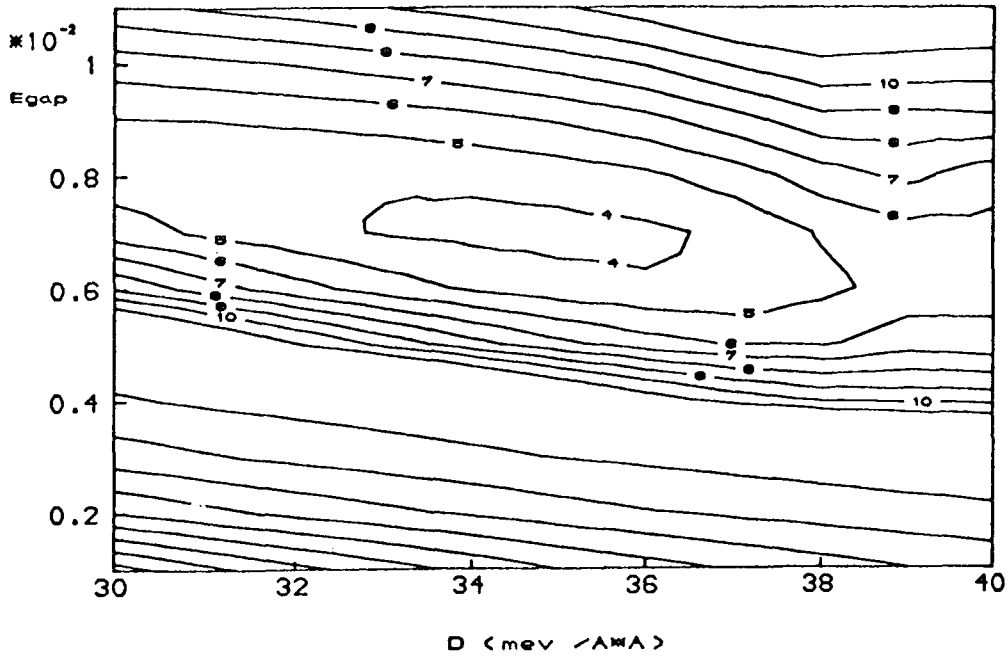

Figure 5.2

Figure 5.3 The best fit data of D(T) and E_g at 10K predicted from the contours in figure 5.2 have been used to simulate data collected at a sample-detector distance of 5m using an incident neutron wavelength of 8±0.6Å using the SCR RPA model. The solid line represents the simulated data using D=35 mevÅ^{-2} and E_g=6μev, whilst the discrete data points represent the observed cross sections inclusive of machine resolution.

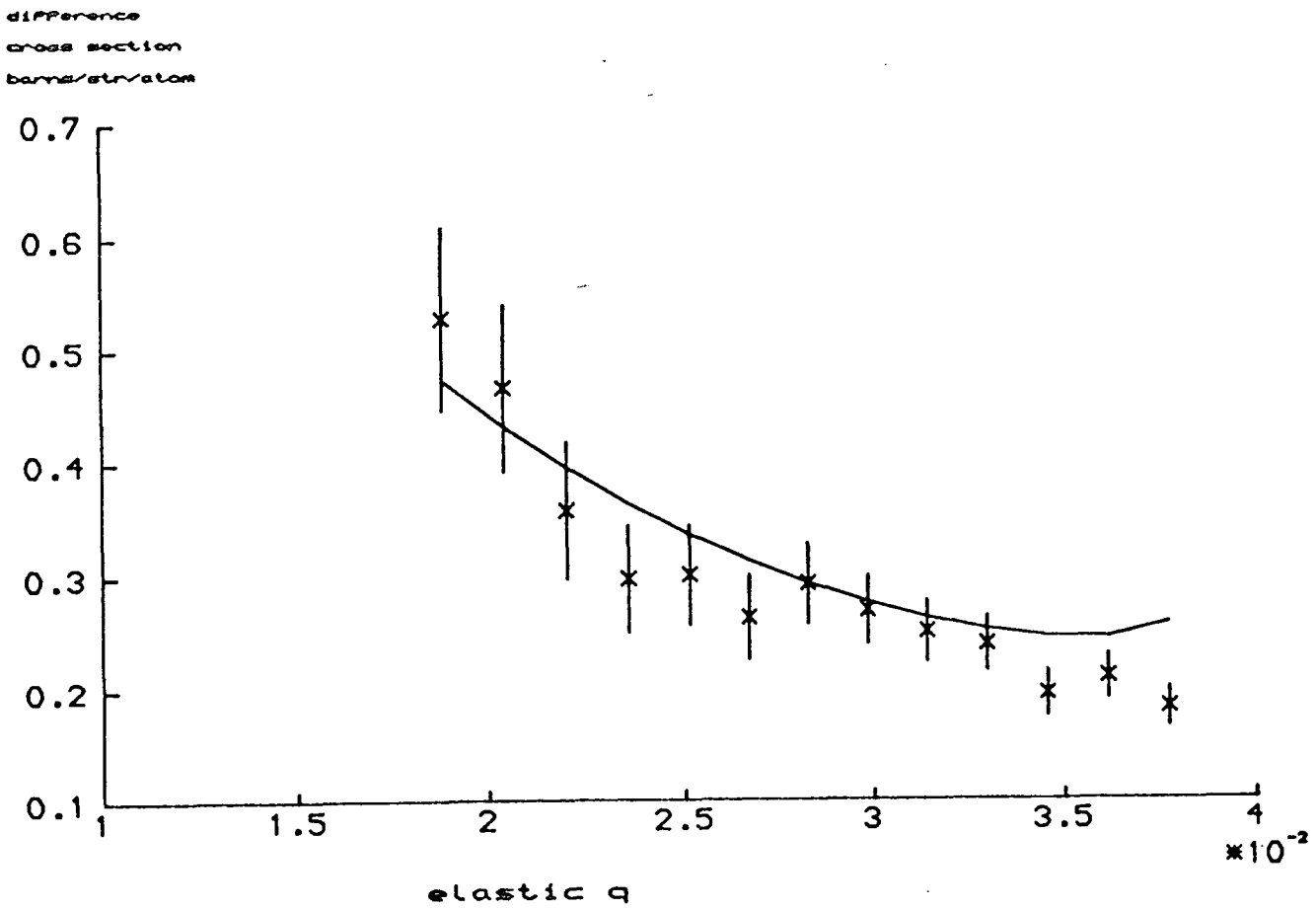
difference
cross section
barns/str/atom
0.7
0.6
0.5
0.4
0.3
0.2
0.1
1
1.5
2
2.5
3
3.5
4
*10^-2
elastic q

Figure 5.3

Figure 5.4 Wavevector dependence of the scattering cross section observed at 10K relative to a low temperature 1.9K background at a neutron incident wavelength of 8±0.6Å. The solid line is a resolution convolved fit to the SCR RPA response function with a pole position of the quadratic dispersion $\hbar\omega(q) = D(T)q^2+E_g$ (a) $E_g=0\mu ev$, (b) $E_g=4\mu ev$. An analytical solution to the integrated response has been used close to θ_c the discontinuity in the simulated response is still visible. This model is clearly not satisfactory in describing the observed high q data.

The rise at high q of the simulated data is from neutrons scattered through angles close to the critical scattering angle picked up due to the machine resolution in angle.

Figure 5.4a

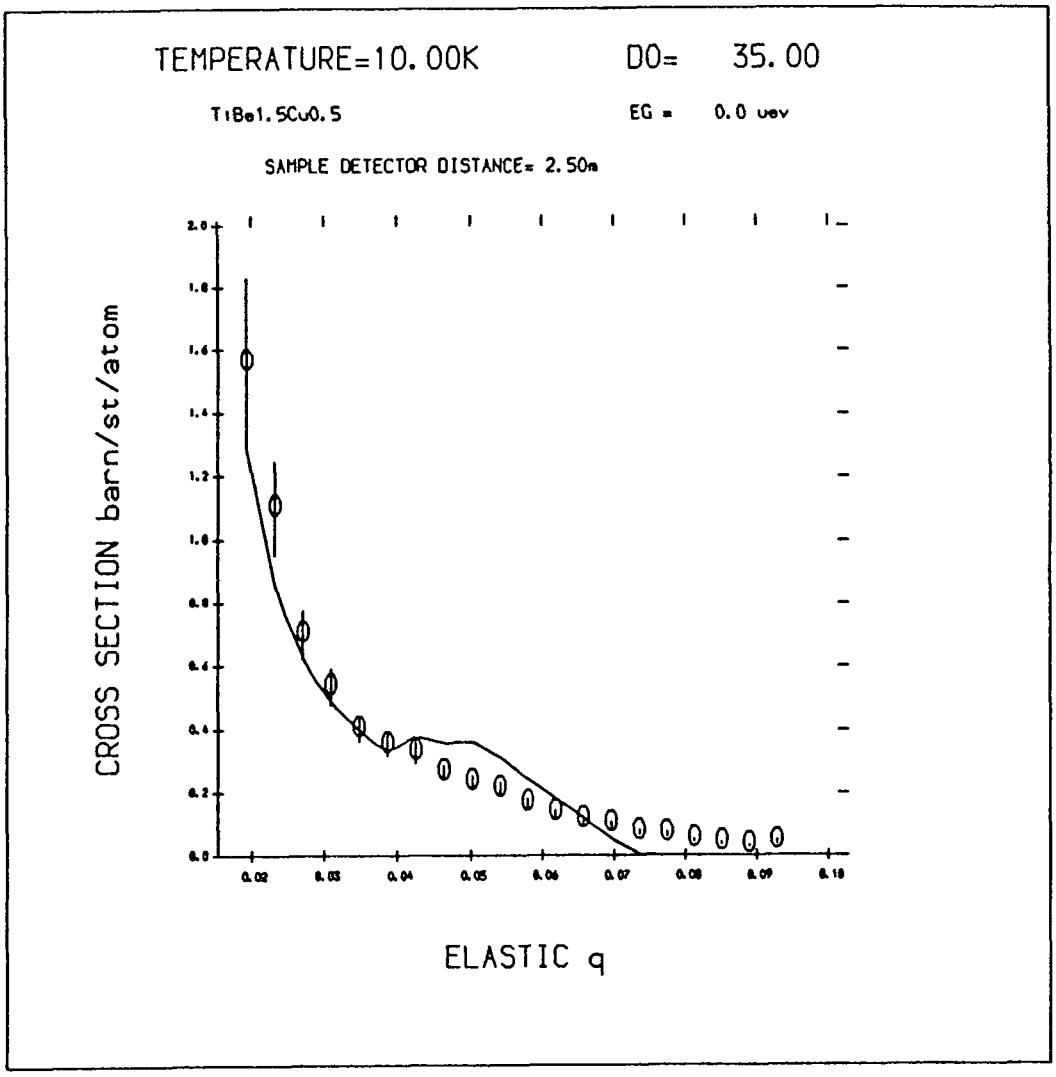
TEMPERATURE=10.00K
D0= 35.00
Ti1Be1.5Cu0.5
EG = 0.0 uev
SAMPLE DETECTOR DISTANCE= 2.50m
CROSS SECTION barn/st/atom
ELASTIC q

Figure 5.4b

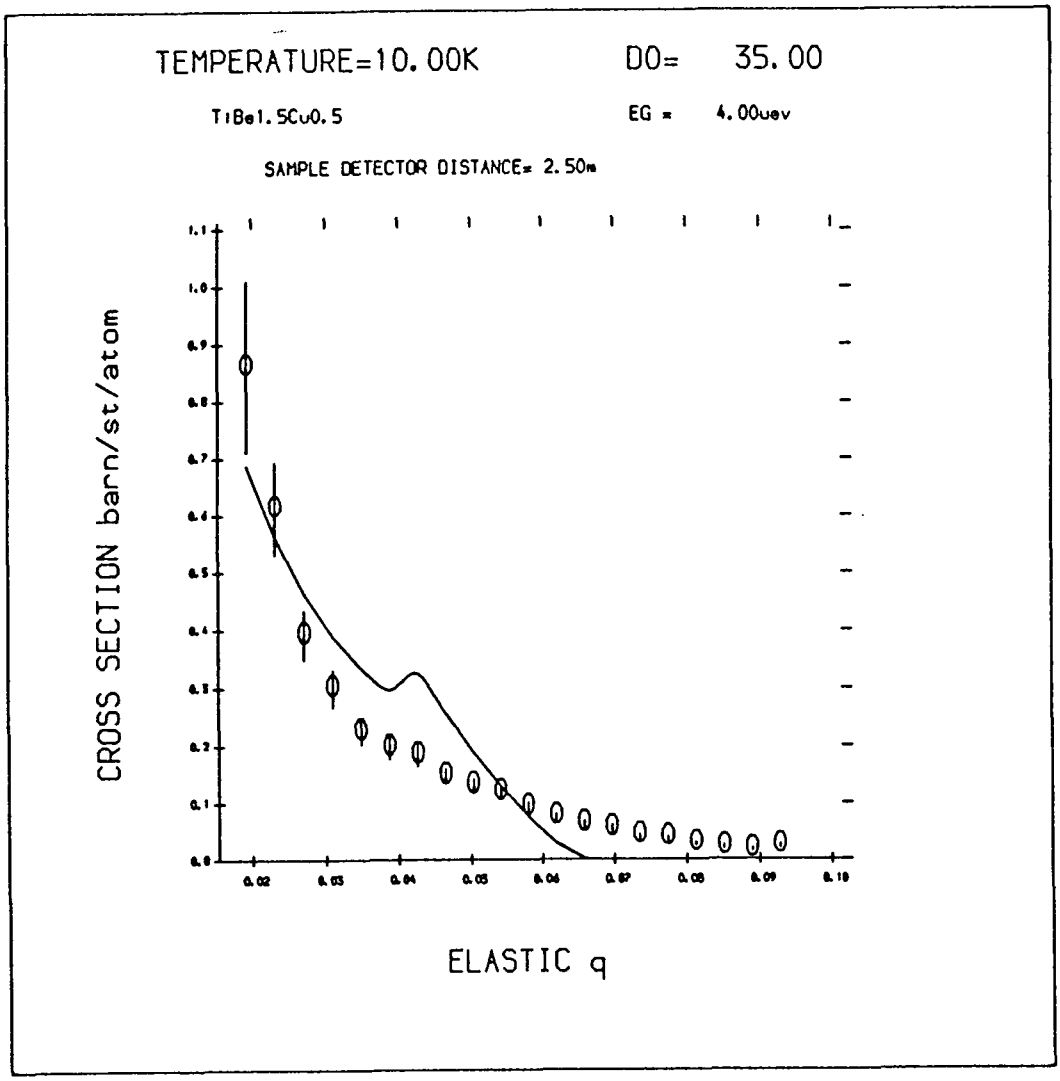
TEMPERATURE=10.00K
DO= 35.00
TiBe1.5Cu0.5
EG = 4.00uev
SAMPLE DETECTOR DISTANCE= 2.50m
CROSS SECTION barn/st/atom
ELASTIC q

in the wavevector regime of study but dominates the response at very low q. The value of this parameter may be misleading where anomalous scattering occurs at low q due to sample or instrument effects. The quantity $c_{\perp}$, which effectively scales the intensity and is temperature independent, has been assumed equal to c defined by the paramagnetic scattering above T_c and the SCR RPA below and is closely related to D(T). The relaxation function $\Gamma(q)$ is a measure of the half width of the line shape function. At low q, $\Gamma(q)$ is small and the Lorentzian line shape function tends toward the delta function response of the SCR RPA model, whilst at higher q the term may become large, widening the distribution along the frequency axis, permitting the modeling of a finite response beyond the critical angle defined in the SCR RPA. This fits in well with the requirements made of a model to supersede the SCR RPA in fitting the observed scattering data.

$$\Gamma(q) = \gamma q X^{-1}(q) \qquad 5.7$$

$$X^{-1}(q) = cq^2 \qquad 5.8$$

The temperature independent parameter $\hbar\gamma$ is the same as that used in the description above T_c.

The computer program developed to model the collected data is complex and uses a great deal of computer resource. The additional complexities over the SCR RPA fit program arises through the need to account for contribution to the total scattering cross section from weighted contributions in all ω,q

space rather than just the four contributions of the SCR RPA. Additionally a new variable parameter is introduced to describe the line shape width. This has limited the fitting of data to the determination of only a few parameter combinations rather than the blanket coverage used to produce contour plots. An effective means of the best fit parameter combinations has been found by iteration using the X^2 fit quantity as a guide to the best fit of data in three bands (i) all q (ii) high q (iii) low q. Using this fit data and by visual inspection of the predicted curve to the experimental calibrated data the parameter combinations have been determined with good accuracy as can be seen from the figures 5.5 and 5.6 showing the fits for data at both sample detector distance settings and at all observed temperatures below T_c. Table 5.1 summaries the observations. The problem in using this solution rather than the contour plots is that errors in the parameters are difficult to predict. Figures 5.10 and 5.11 show the variation in $\hbar\gamma$ and c with temperature, the spread of the predicted points away from the average model curves gives an indication of the errors in the parameters.

5.5.3 Modeling the Data Above T_c

The theoretical diffuse scattering response above T_c described through the imaginary part of the generalised susceptibility by:

$$\chi''(q,\omega) = \frac{\omega\chi(q)\Gamma(q)}{\omega^2 + \Gamma^2(q)} \qquad 5.9$$

$$\Gamma(q) = \gamma q \chi^{-1}(q) \qquad 5.10$$

$$\chi^{-1}(q) = \chi^{-1} + cq^2 \qquad 5.11$$

has been used to fit data using values of c and $\hbar\gamma$ predicted below T_c and using $\chi^{-1}(T)$ as a floating parameter.

The fits obtained at just above the Curie temperature (27-28K) and at 35K from data collected at both sample-detector distance settings are shown in table 5.2. The inverse susceptibility parameter agrees well with that measured using the vibrating sample magnetometer in chapter 4 providing a good check on the models applicability in the description of observed scattering. The fitted data is shown in diagrams 5.7 and 5.8.

5.6 Conclusions

Figure 5.9 summaries three fits at the 5m sample detector distance setting at three temperatures spanning the Curie temperature. This is the first documented account of the use of a single model lineshape to describe observations of damped magnetic scattering from a weak itinerant magnet below and above the magnetic phase transition. Two fundamental parameters c and $\hbar\gamma$ are sufficient to describe the observations. Figures 5.10 and

5.11 show the variation of the empirical parameters c and $\hbar\gamma$ with temperature, deviation from the average solid line in each case describes the errors associated with the determination of these values using the neutron scattering technique. It has been proposed that the temperature variation of the spin wave stiffness follows a simple form. The validity of this description is shown in figure 5.12, the solid line representing the theoretical value of D(T).

The use of a damped coupled harmonic oscillator description collapsing to a single pole at the Curie temperature is effective in the description of collective fluctuations in the $TiBe_{1.5}Cu_{0.5}$ system across the phase transition. Questions arise regarding the fundamental nature of these fluctuations in the parent alloy. It has been shown that with the application of an external magnetic field[53] an internal ferromagnetic state is induced. In this situation are the collective fluctuations below T_c damped spin waves or indeed best described by the undamped spin wave model of the SCR RPA? The damped spin wave modes may for instance only be associated with rather impure systems which by definition the substitution of Cu in a lattice at random positions causes. The study of $TiBe_{2-x}Cu_x$ for $0<x<0.5$ may be revealing here.

TABLE 5.1

Sample Detector Distance(m)	Temperature (K)	D ($mevÅ^{-2}$) (±6)	E (μev) (±3)	$\hbar\gamma$(μevÅ) (±1)	X^2
5	5	32	2	3	10
	10	35	4	3	11.6
	20	24	2	3	17
2.5	5	30	3	3	5
	10	30	5	3	2
	20	20	10	3	8
	22	25	6	3	6.7

TABLE 5.2

Sample Detector Distance(m)	Temperature (K)	$\hbar\gamma$(μevÅ) (±1)	c $x10^4(Å^2)$ (±1.2)	X^{-1}	X^2
5	27.5	2.7	5	15	4.9
2.5	27.6	2.7	5.3	20	3.35
	35	3.5	5.4	200	21

Figure 5.5 The normal scattering angle dependence ($q_{el}=2\pi\theta/\lambda$ for small angles) of the observed scattering cross section difference at a sample-detector distance of 5m, an incident neutron wavelength of 8±0.6Å at temperatures of (a) 5K, (b) 10K, (c) 20K. The solid line is a resolution convolved fit to the two pole damped harmonic oscillator response function with a pole at the position $h\omega(q) = D(T)q^2+E_g$. The parameters used in the fits are given in Table 5.1.

Figure 5.5a

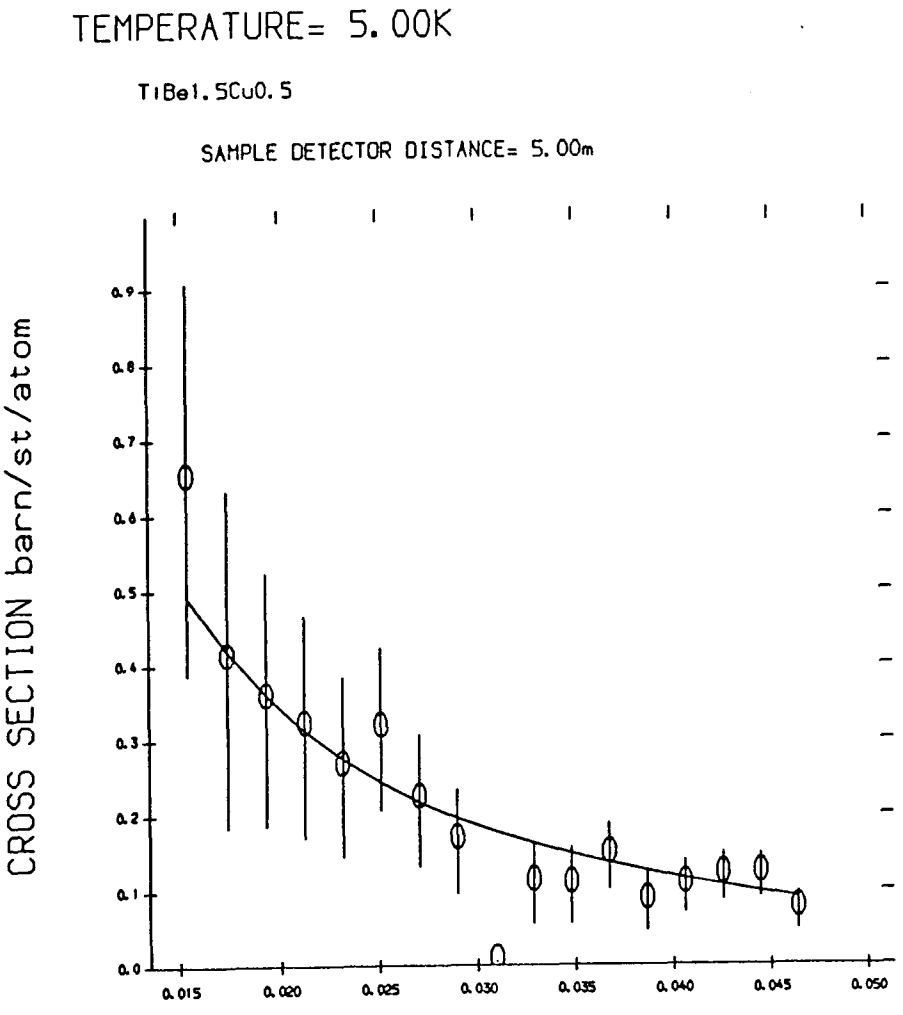
TEMPERATURE= 5.00K
TiBe1.5Cu0.5
SAMPLE DETECTOR DISTANCE= 5.00m
CROSS SECTION barn/st/atom
0.0
0.1
0.2
0.3
0.4
0.5
0.6
0.7
0.8
0.9
0.015
0.020
0.025
0.030
0.035
0.040
0.045
0.050
SCATTERING ANGLE θ radians

Figure 5.5b

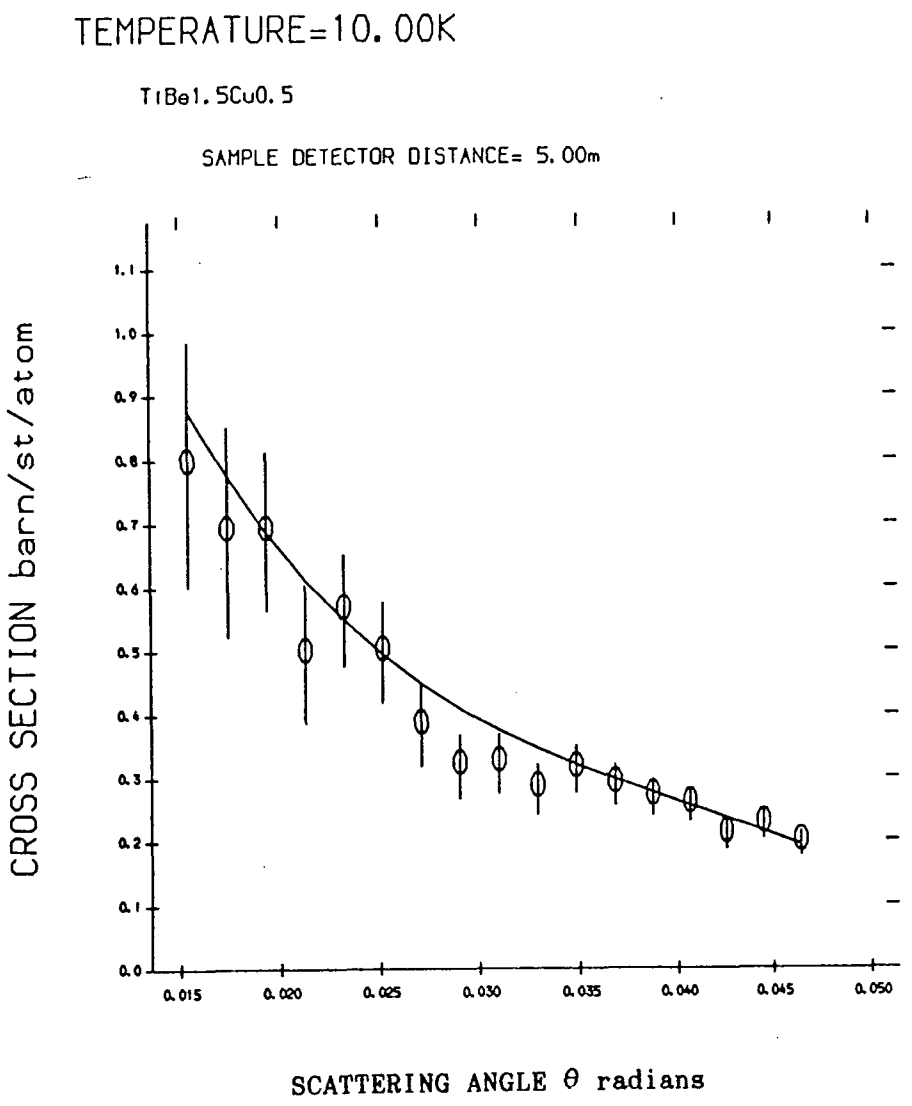
TEMPERATURE=10.00K
TiBe1.5Cu0.5
SAMPLE DETECTOR DISTANCE= 5.00m
CROSS SECTION barn/st/atom
1.1
1.0
0.9
0.8
0.7
0.6
0.5
0.4
0.3
0.2
0.1
0.0
0.015
0.020
0.025
0.030
0.035
0.040
0.045
0.050
SCATTERING ANGLE θ radians

Figure 5.5c

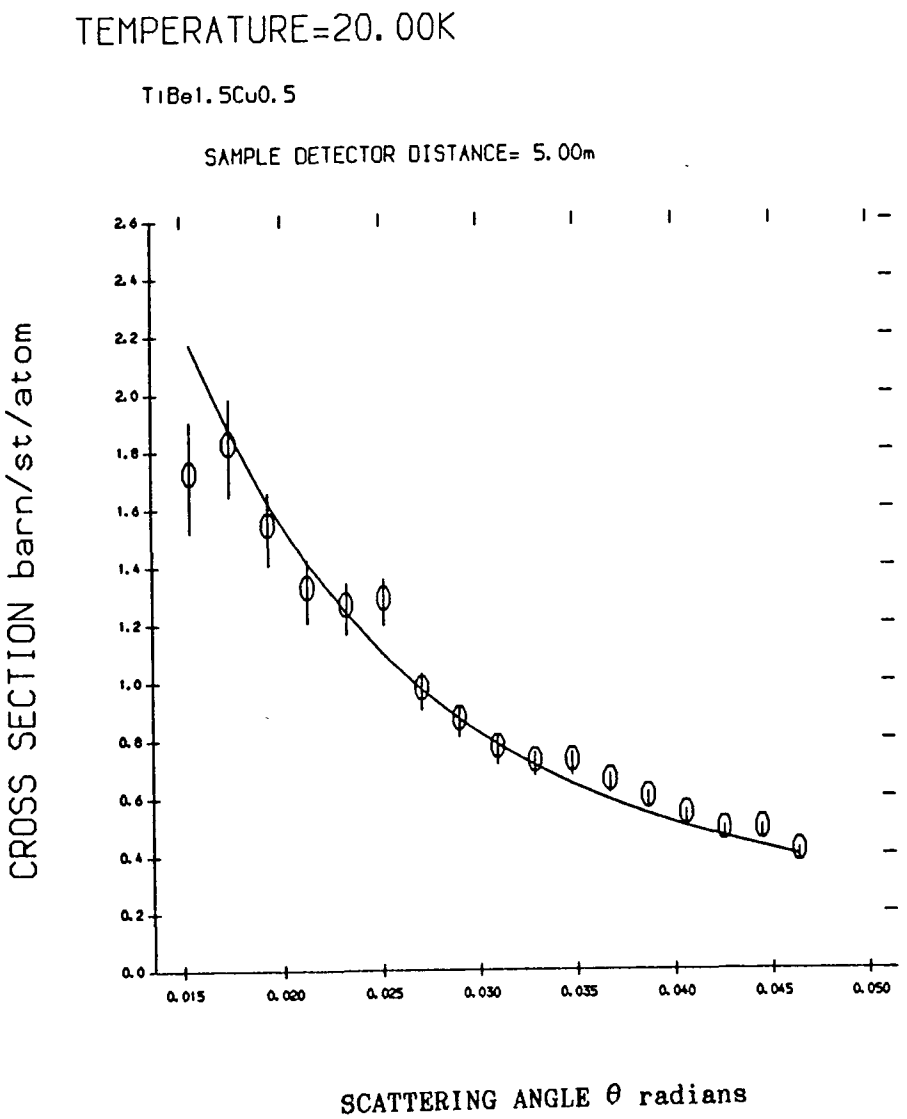
TEMPERATURE=20.00K
TiBe1.5Cu0.5
SAMPLE DETECTOR DISTANCE= 5.00m
CROSS SECTION barn/st/atom
2.6
2.4
2.2
2.0
1.8
1.6
1.4
1.2
1.0
0.8
0.6
0.4
0.2
0.0
0.015
0.020
0.025
0.030
0.035
0.040
0.045
0.050
SCATTERING ANGLE θ radians

Figure 5.6 The normal scattering angle dependence ($q_{el}=2\pi\theta/\lambda$ for small angles) of the observed scattering cross section difference at a sample-detector distance of 2.5m, an incident neutron wavelength of 8±0.6Å at temperatures of (a) 5K, (b) 20K. The solid line is a resolution convolved fit to the two pole damped harmonic oscillator response function with a pole at the position $\hbar\omega(q) = D(T)q^2+E_g$. The parameters used in the fits are given in Table 1.

Figure 5.6a

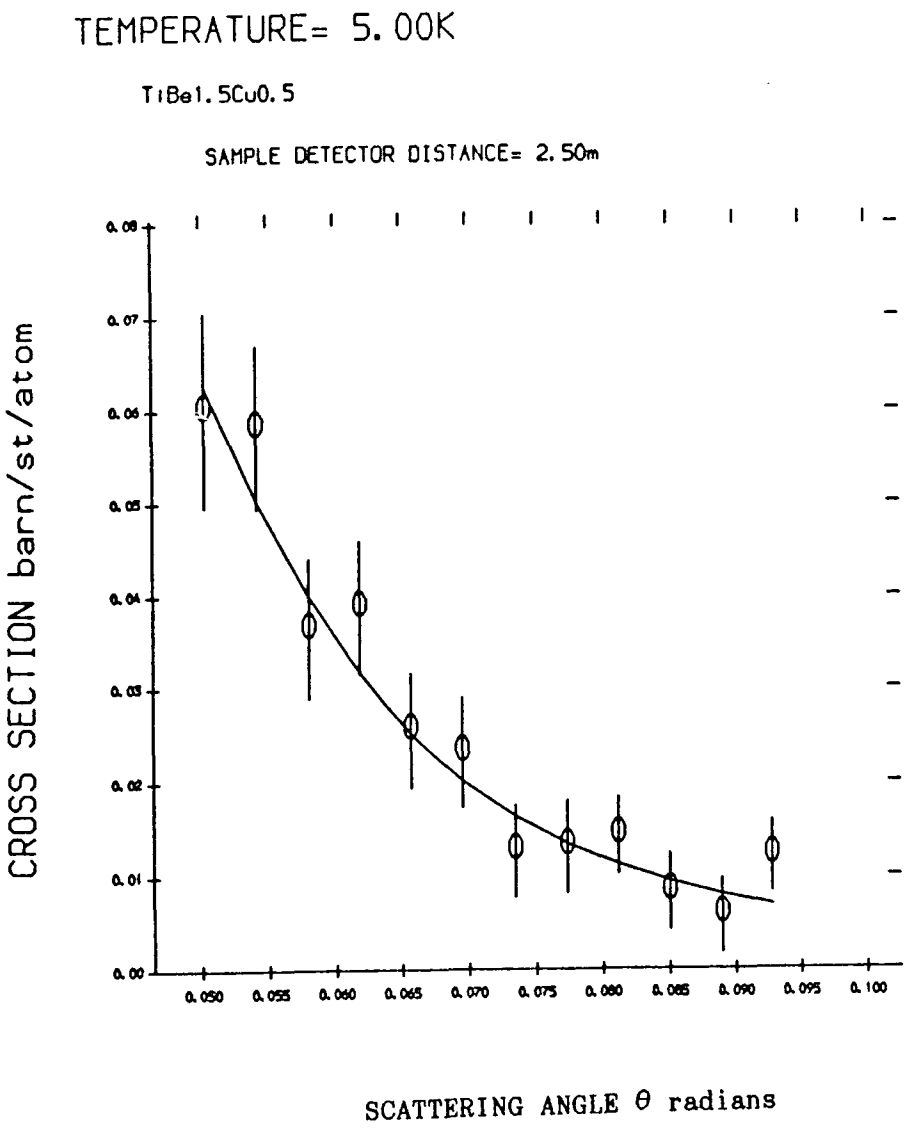
TEMPERATURE= 5.00K
TiBe1.5Cu0.5
SAMPLE DETECTOR DISTANCE= 2.50m
CROSS SECTION barn/st/atom
0.00
0.01
0.02
0.03
0.04
0.05
0.06
0.07
0.08
0.050
0.055
0.060
0.065
0.070
0.075
0.080
0.085
0.090
0.095
0.100
SCATTERING ANGLE θ radians

Figure 5.6b

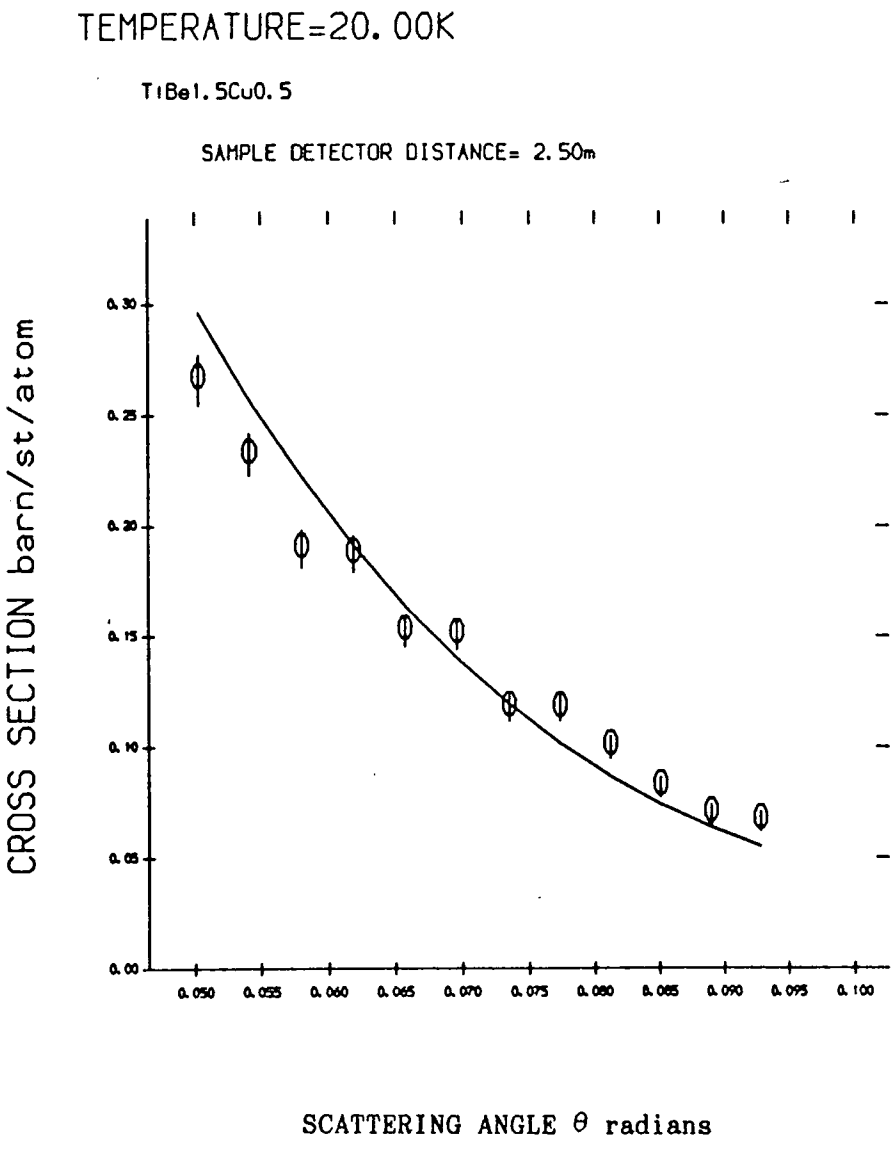
TEMPERATURE=20.00K
TiBe1.5Cu0.5
SAMPLE DETECTOR DISTANCE= 2.50m
CROSS SECTION barn/st/atom
0.30
0.25
0.20
0.15
0.10
0.05
0.00
0.050
0.055
0.060
0.065
0.070
0.075
0.080
0.085
0.090
0.095
0.100
SCATTERING ANGLE θ radians

Figure 5.7 Scattering angle dependence ($q_{el}=2\pi\theta/\lambda$) of the small angle scattering measured at 27.5K and modeled using a single pole $X''(q,\omega)$ description of scattering from collective fluctuations above the magnetic phase transition. $X''(q,\omega)$ is defined in equation 5.9 with a relaxation frequency $\Gamma(q)=\gamma q(X^{-1}+cq^2)$, $\hbar\gamma=2.7\mu ev$ and $c=5x10^4 A^2$ with $X^{-1}=15$.

Figure 5.7b

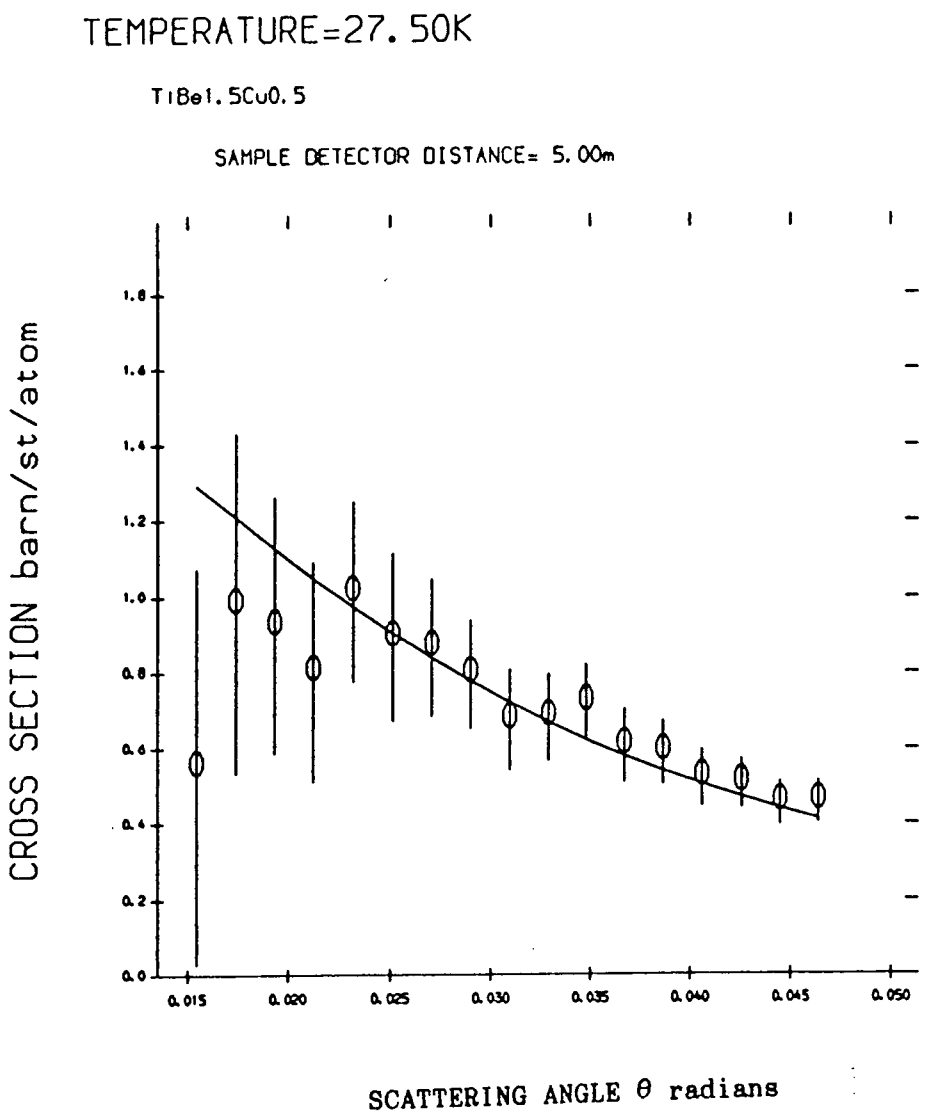
TEMPERATURE=27.50K
TiBe1.5Cu0.5
SAMPLE DETECTOR DISTANCE= 5.00m
CROSS SECTION barn/st/atom
1.8
1.6
1.4
1.2
1.0
0.8
0.6
0.4
0.2
0.0
0.015
0.020
0.025
0.030
0.035
0.040
0.045
0.050
SCATTERING ANGLE θ radians

Figure 5.8 The small angle scattering angle dependence of the collective fluctuation above T_c for (a) T=27.6K and (b) T=35K for neutrons incident with a wavelength of 8±0.6Å and a sample-detector distance of 2.5m. The solid line is a resolution convolved fit to a single pole description of $X''(q,\omega)$.

(a) $\hbar\gamma = 2.7\mu ev$ $c = 5.3x10^{-4}Å^2$ $X^{-1} = 20$

(b) $\hbar\gamma = 3.5\mu ev$ $c = 5.4x10^{-4}Å^2$ $X^{-1} = 200$

Figure 5.8a

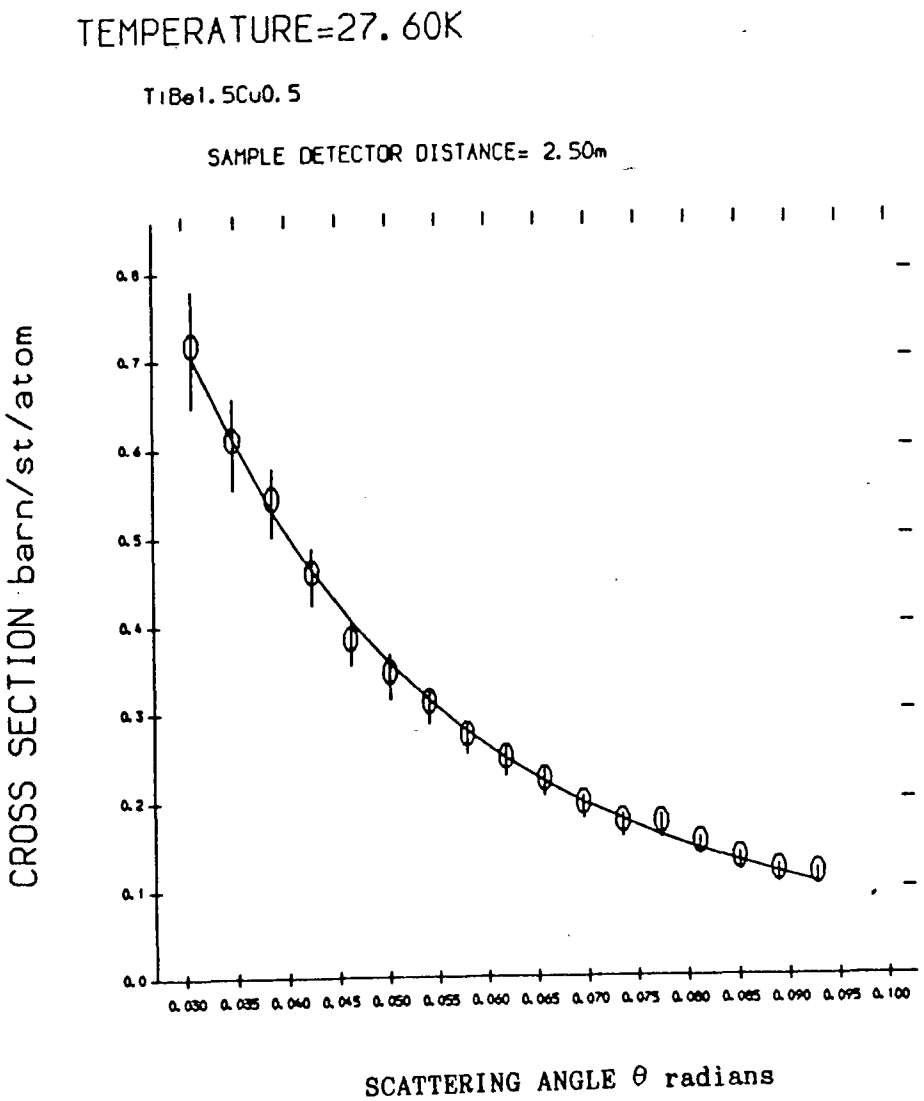
TEMPERATURE=27.60K
TiBe1.5Cu0.5
SAMPLE DETECTOR DISTANCE= 2.50m
CROSS SECTION barn/st/atom
0.0
0.1
0.2
0.3
0.4
0.5
0.6
0.7
0.030 0.035 0.040 0.045 0.050 0.055 0.060 0.065 0.070 0.075 0.080 0.085 0.090 0.095 0.100
SCATTERING ANGLE θ radians

Figure 5.8b

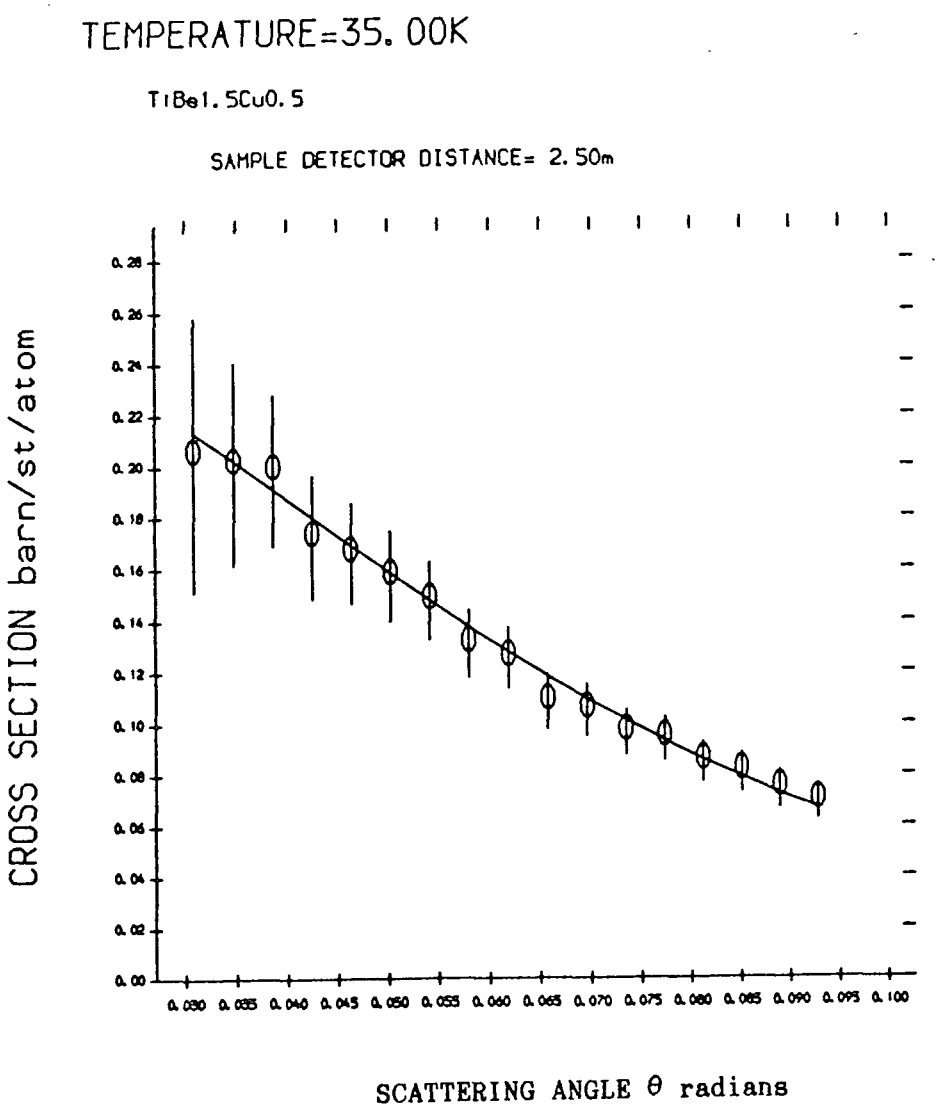
TEMPERATURE=35.00K
TiBe1.5Cu0.5
SAMPLE DETECTOR DISTANCE= 2.50m
CROSS SECTION barn/st/atom
0.28
0.26
0.24
0.22
0.20
0.18
0.16
0.14
0.12
0.10
0.08
0.06
0.04
0.02
0.00
0.030 0.035 0.040 0.045 0.050 0.055 0.060 0.065 0.070 0.075 0.080 0.085 0.090 0.095 0.100
SCATTERING ANGLE θ radians

Figure 5.9 The wavevector dependence of the difference cross sections observed and simulated at (a) 5K (b) 20K and (c) 27.5K where T_c=27K. The spectrometer has been used in a configuration with an incident wavelength of 8±0.6Å and a sample-detector distance of 5m. The simulated data parameter values of D and the energy gap are given in Tables 5.1 and 5.2.

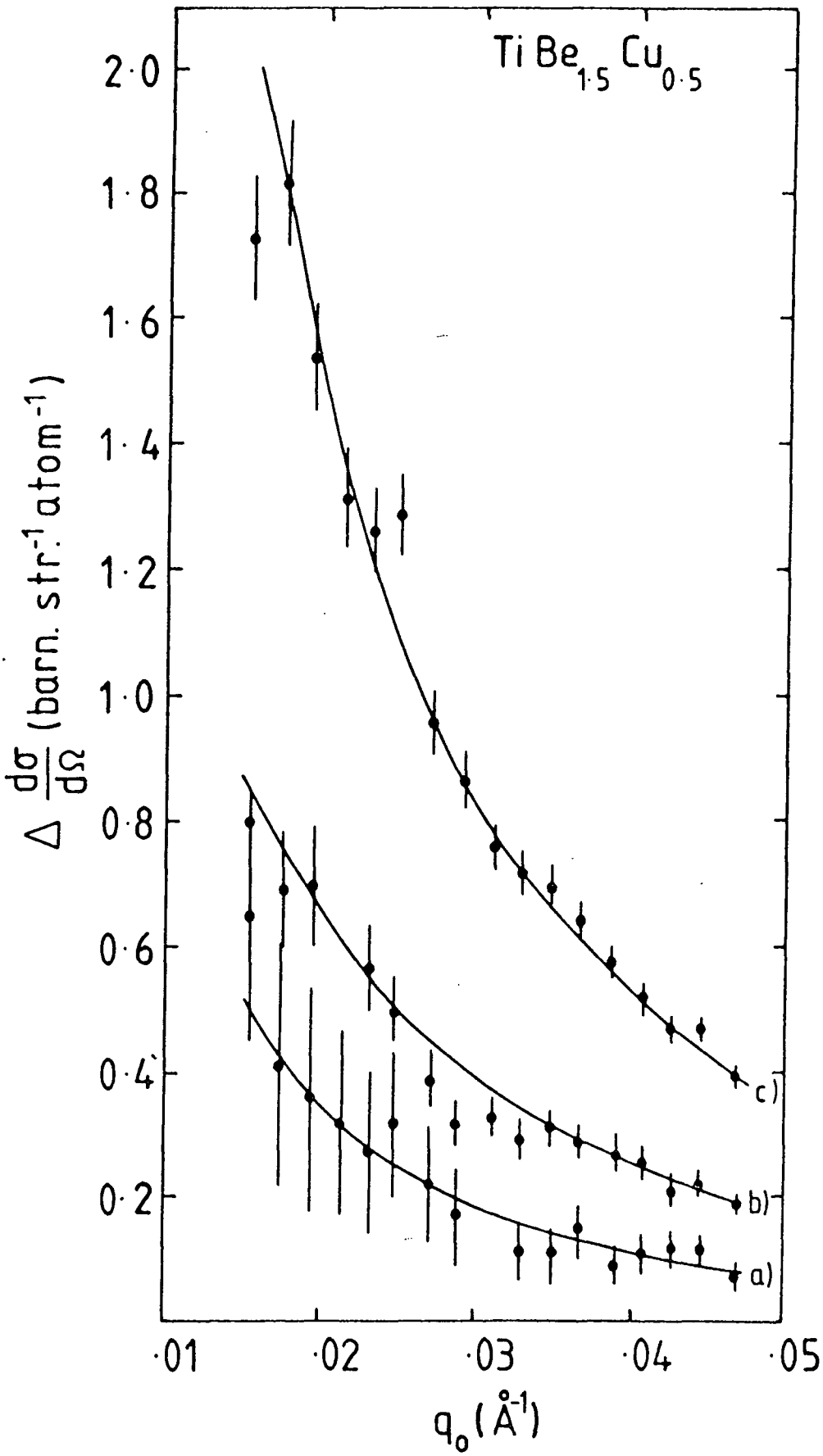
Ti Be1·5 Cu0·5
2·0
1·8
1·6
1·4
1·2
1·0
0·8
0·6
0·4
0·2
Δ dσ/dΩ (barn. str.-1 atom-1)
·01
·02
·03
·04
·05
q0 (Å-1)
c)
b)
a)

Figure 5.9

Figure 5.10 The simulated temperature dependence of the torsional constant c. In theory the variation from the mean should be due only to experimental error in the determination of c.

Figure 5.10

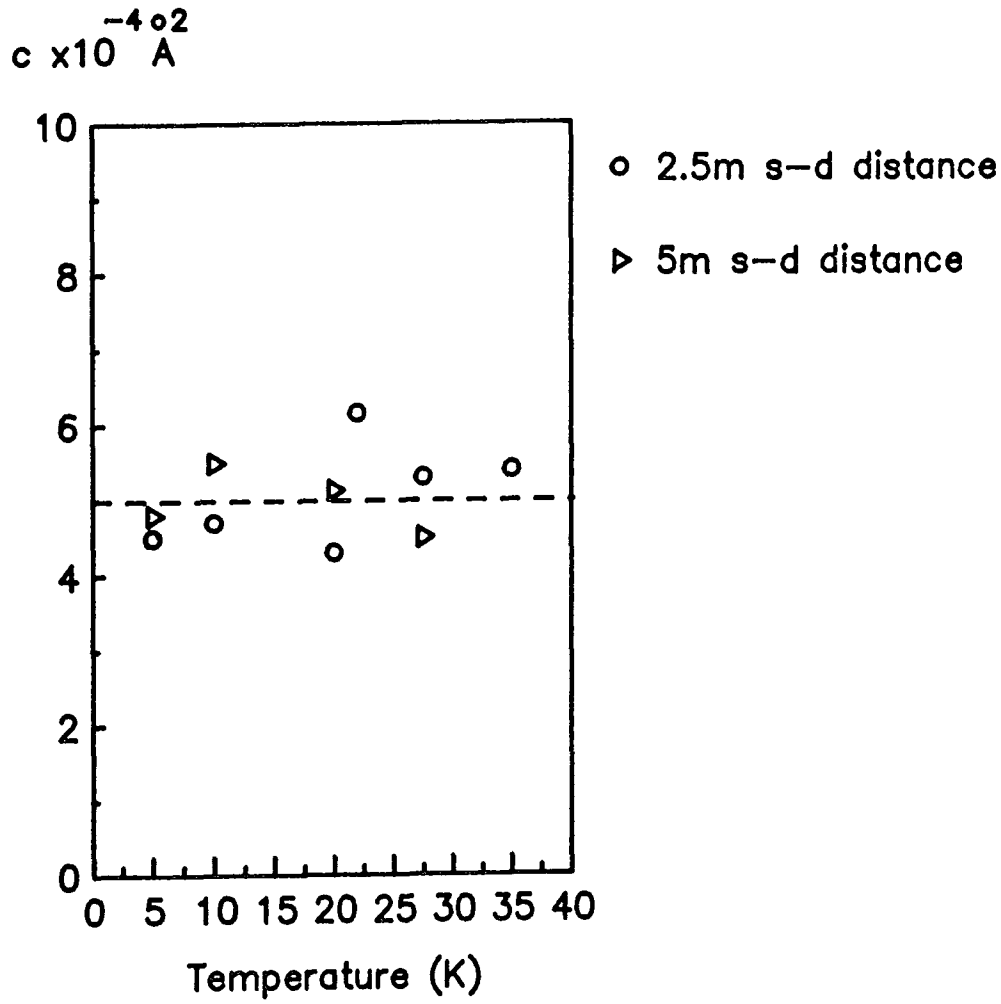
c x10^-4 o2 A
10
8
6
4
2
0
0 5 10 15 20 25 30 35 40
Temperature (K)
o 2.5m s-d distance
▷ 5m s-d distance

Figure 5.11 The temperature dependence of the model parameter $\hbar\gamma$, in theory it is temperature independent. The error bars are those predicted from calculation of the quantity at each individual temperature, the true error in the parameter is that given by the variation from the mean value.

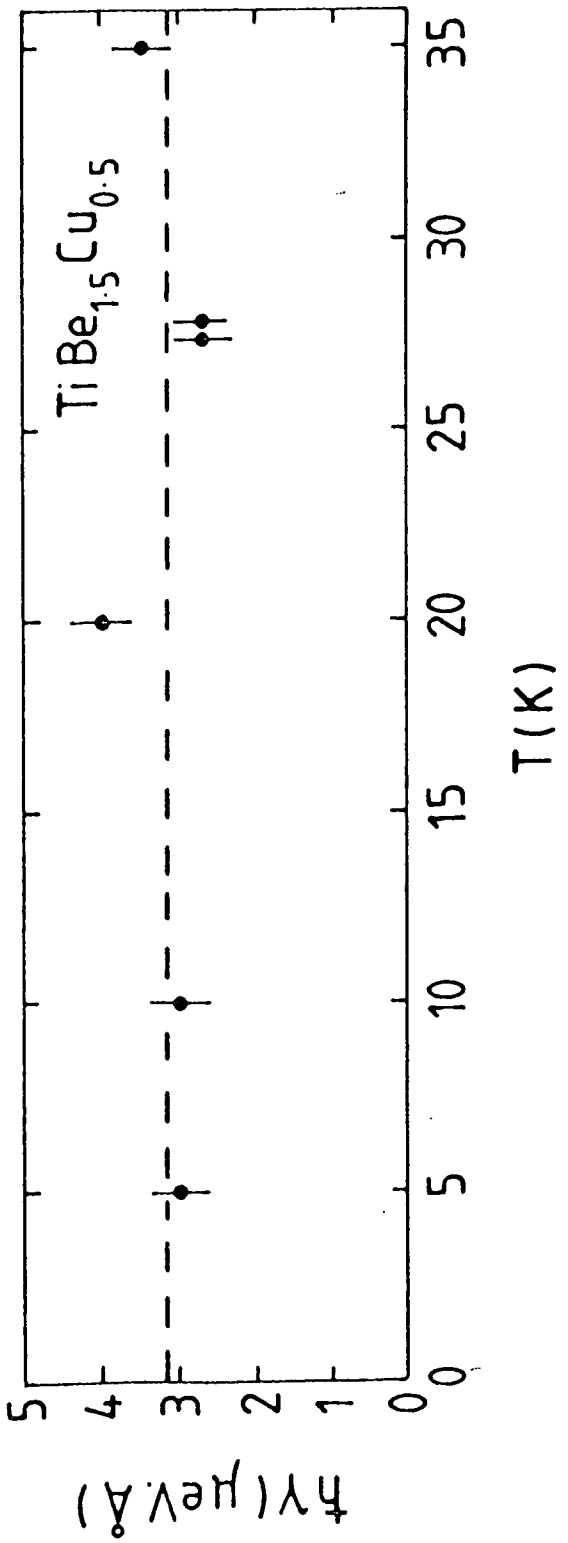

Figure 5.11

Figure 5.12 The spin wave stiffness calculated from the fitted data against the proposed theoretical temperature dependence $D(T) = D_0(1-(T/T_c)^2)^{1/2}$.

Figure 5.12

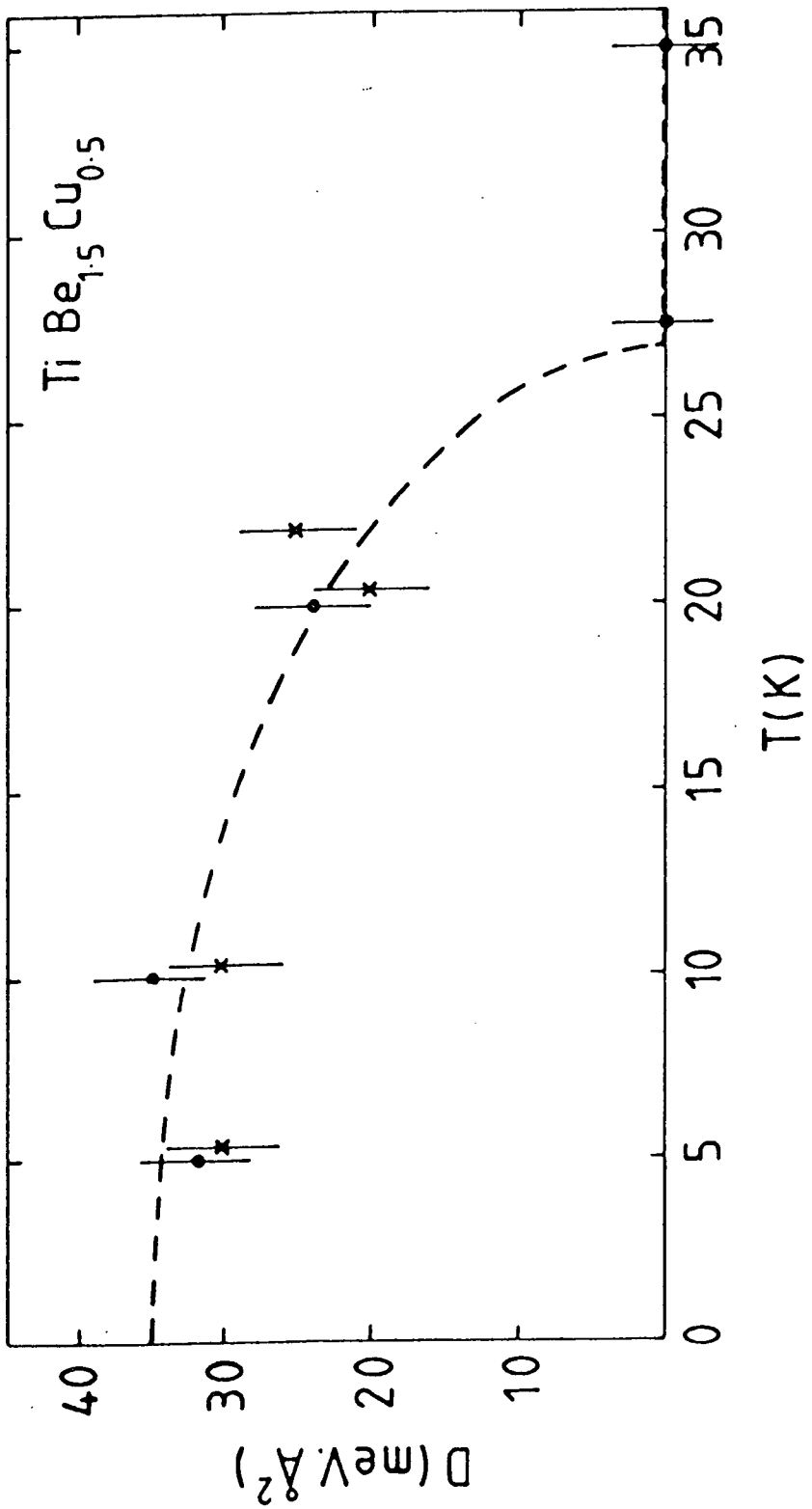

CHAPTER 6

MAGNETIC DENSITY DISTRIBUTION DETERMINATION

6.1 Introduction

The neutron possesses no electrical charge whilst it maintains a magnetic dipole moment. This combination provides a unique probe of matter. The presence of a magnetic moment provides scope for polarisation of a neutron beam with respect to the spin quantum number.

The neutron interacts with matter both by non-magnetic and magnetic scattering the latter occurring through three distinct interactions. The first of these is through the electron spins the second is through the orbital angular momentum of unpaired electrons and the third is through interactions with the nuclear spins.

Of primary interest in this work is the interaction with electrons from the incompletely filled atomic electron shells such as the 3d and 4d orbitals of the transition elements. The contribution to the total neutron scattering cross section arising from magnetic scattering from the electron current is of little importance in transition metal systems owing to the presence of a

crystal field that lifts the orbital degeneracy of the ground state wave function and effectively quenches the orbital contribution. The ion of the rare earth elements posses both spin and unquenched orbital angular momentum. Since the system under investigation contains both 3d (Fe) and 4d (Zr) transition ions the presence of a significant magnetic moment at the Zr atom site might well require that orbital degeneracy effects be considered.

In any neutron diffraction experiment the most general aim is the determination of a complete set of structure factors out to a specified position in reciprocal space. The structure factor, defined at a given Miller index hkl, F_{hkl} is related to the distribution of scattering centers within a given crystallographic cell:

$$F_{hkl} = \sum_i A_i f_i(k)\, e^{ik.r_i} e^{-w_i \sin^2\theta_i/\lambda_i^2} \qquad 6.1$$

Where i is the position of the i^{th} scattering center with the scattering power A_i and the form factor $f_i(k)$. $e^{-w_i \sin^2\theta_i/\lambda_i^2}$ is the Debye Waller factor that is a measure of the scattering response variation with temperature due to thermal vibrations of the scattering center. 2θ is defined as the angle between the incident and exit wavevectors for diffraction experiments (in contrast to small angle quasielastic scattering).

F_{hkl} describes either the nuclear or the magnetic scattering

structure factors. In the case of nuclear scattering the $A_i f_i(k)$ term may be replaced by the single parameter b, the scattering amplitude[56]. No form factor is required in this description because of the short range of the interaction ($\approx 10^{-12}$ to 10^{-13} cm) compared to the wavelength of a thermal neutron ($\approx 10^{-8}$ cm) resulting in isotropic scattering. Magnetic scattering is primary due to the outer electrons whose spatial distribution is comparable with thermal wavelengths, a form factor is thus involved in the scattering description and may be Fourier inverted to yield a spatial distribution of the magnetisation density.

The distribution of scattering centers (ρ) within the crystal cell may be calculated from:

$$\rho_r = \frac{1}{V}\sum_i F_{hkl} e^{ik.r_i} \qquad 6.2$$

where V is the volume of the unit cell.

The way in which individual structure factors are related to the diffracted intensities is not unique but dependent upon the crystal perfection. In the case of an ideal crystal, where coherence is maintained throughout the whole crystal, the intensity is dynamically exchanged between the incident and diffracted beams. The first Born approximation cannot be used to simplify calculation. In this dynamical scattering limit the integrated intensities, after complex theoretical analysis may be shown to be proportional to $|F_{hkl}|^{18}$.

Most crystals however possess irregularities in their atomic arrangements resulting in the whole consisting of many small crystallites as a consequence of dislocations, point defects and sub grain boundaries. These inhomogeneities destroy the coherence between the components of the incident beam scattered by different parts of the crystal. The individual crystallites are themselves sufficiently perfect to reflect the beam coherently. In this limit scattering may be considered in the kinematical limit in which the first Born approximation may be used. In this case the system can be thought to consist of a mosaic spread of blocks the scattering from which results in an angular broadening of the scattered beam.

In the kinematical limit the scattering intensities can be shown to be proportional to the sum of the squares of the magnetic and nuclear scattering factors (see section 6.3).

It is possible to measure the magnetic contribution to the diffracted intensities using standard neutron diffraction techniques assuming a knowledge of the nuclear scattering factors is available from theoretical calculations. The main disadvantage of this method is that for weak magnetic systems the magnetic scattering intensities become small quickly away from q=0 events when compared to the nuclear scattering intensities. This is due to a combination of the magnetic from factor which falls quickly with increasing momentum transfer and the small magnetic moment that governs the magnetic scattering power.

Using a polarised incident beam (all incident neutron spins either up or down) provides an alternative and potentially more refined method for the determination of the magnetic structure factors. The major disadvantage of this method is that to produce a polarised beam there is a large reduction in intensity of the incident beam over a conventional beam. Until recently this lack of intensity on polarised neutron instruments was low enough to discount all but the easiest of experiments. The relative intensity between the unpolarised and polarised beams remain very similar to this day but the absolute intensity has increased to a level where many experiments may be carried out. One must balance one technique against the other before deciding on the more appropriate method and use of beam time. Because of the requirement for accurate determination of a possibly weak magnetic signal and good data for the production of a fourier map of the magnetisation density of the sample, the polarised neutron technique was chosen.

6.2 Sample Requirements

There are several requirements made of the sample for effective use of a polarised source. A good quality single crystal of the material is highly desirable, that is one with high order, stoichiometry and purity. The magnetic and nuclear structure factors, defined by the crystallographic structure of the material, must neither be zero nor in phase quadrature to one

another. The determination of unambiguous results is only possible if the nuclear structure is centrosymmetric since the magnetic form factor cannot be found exactly even when the amplitude and phase of the nuclear structure factors are known. These requirements are satisfied by the C15 cubic laves structure of $ZrFe_2$. The magnetic structure factors are also centrosymmetric furthering the ease of analysis.

6.3 The Polarised Neutron Technique

The present work involves the study of an ordered magnetic system in a large magnetic field (4.6 Tesla) applied perpendicular to the scattering plane. It is preferential for analysis of the collected intensities that all domains in the crystal are aligned otherwise depolarisation of the beam may result.

In the case of an incident polarised beam of neutrons scattering from a solid through both nuclear and magnetic interactions the theoretical differential cross section in the first Born approximation consists of 4 terms[18]. Two of these terms are simply the purely nuclear and magnetic scattering cross sections as in the case of an unpolarised experiment. The two additional contributions arise from (i) interference between nuclear and magnetic scattering and (ii) an additional magnetic term that does not contribute to the scattering cross section when all system spins are aligned either parallel or anti-parallel.

For a system where the term (ii) is zero the differential

cross section has been shown by Halpern and Johnson[57] to reduce to:

$$\sigma = b^2 + 2bp\lambda.q + p^2q^2 \qquad 6.3$$

For scattering from a single atom, where q is the magnetic interaction vector defined by:

$$q = \epsilon(\epsilon.k)-k \qquad 6.4$$

and k is the unit vector in the direction of the atomic magnetic spin and ϵ is a unit vector in the direction perpendicular to the effective reflecting planes of the crystal i.e. the scattering vector. b is the nuclear scattering length whilst p, for a system where the orbital contribution to the magnetic scattering is fully quenched, is defined by:

$$p= \left(\frac{e^2\gamma}{2mc^2}\right)2Sf \qquad 6.5$$

f is the magnetic form factor and 2S is equal to the magnetic moment of the system in Bohr magnetons.

The geometry in this experiment has been chosen, as far as possible, such that $q^2=1$.

6.4 Diffracted Intensities

The study of scattered intensities due to an an incident polarised beam of neutrons was performed at the I.L.L. on the D3 diffractometer. This machine is a two axis diffractometer on which the incident beam is either parallel or antiparallel to the specimen rotation axis ω, which is in general the sample magnetisation direction. The detector moves about two axes, γ parallel to ω and ν that allows the detection of reflection out of the equatorial plane.

The polarised beam is produced by reflection from the (220) plane of a $Co_{98}Fe_{8}$monochromator. This particular reflection satisfies the condition that $|F_N| \approx |F_M|$ which is the criterion at which nearly total polarisation occurs. The actual polarisation of the incident beam is dependent upon the incident wavelength but on D3 always falls within 98±1%.

Figure (6.1) shows a schematic representation of the D3 diffractometer.

The polarisation of the beam P is given by the ratio defined in equation 6.6. n^+ and n^- signify spin parallel and antiparallel.

$$P = \frac{n^+ - n^-}{n^+ + n^-} \qquad 6.6$$

Figure 6.1 The D3 polarised neutron diffractometer at the Institut Max Von Laue, Paul Langevin (ILL), Grenoble, France. Taken from the ILL publication -Neutron Research Facilities at the ILL High Flux Reactor (1983).

Figure 6.1

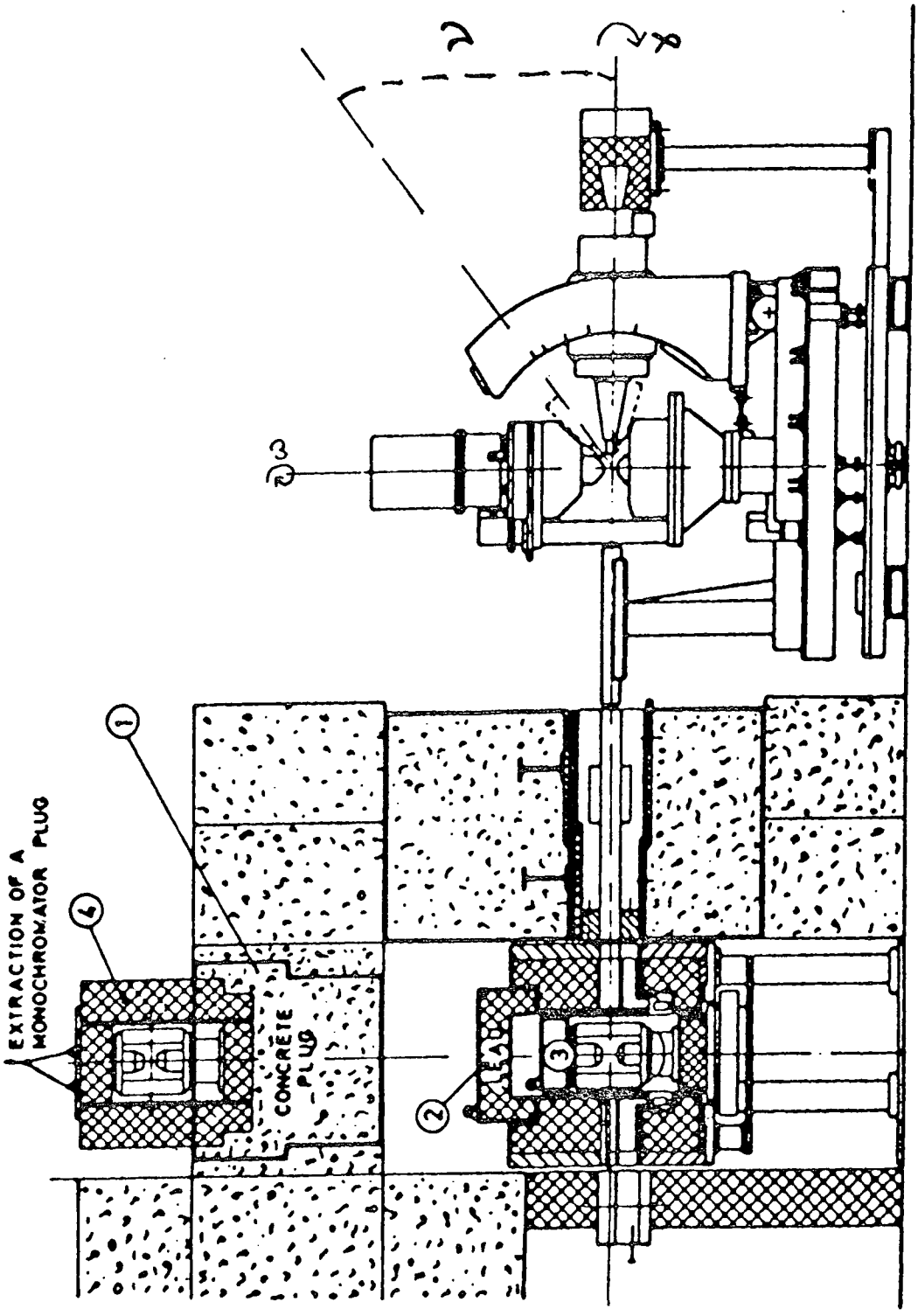

For scattering from an assembly of atoms a phase difference term is included for scattering from different atoms. This results in b and p in equation 6.3 becoming equal to the scattering factors. If the magnetic scattering amplitude includes a significant contribution from the orbital angular momentum of the unpaired electrons the definition of p becomes significantly more complex.

When the orbital contribution to the total scattering intensity is quenched the diffracted intensities are given by[18].

$$I(K) \propto F_M^2(k) + F_N^2(k) + 2\ P\ F_N(k).F_M(k) \qquad 6.7$$

From this equation it can be seen that even when the magnetic structure factor F_m becomes small compared to the nuclear structure factor F_n the cross term may add significantly to the diffracted intensities. This technique therefore lends itself well to the analysis of ordered weak magnetic materials. By analysing the spins of the diffracted beam one may gain further information, specifically about the absolute direction of the magnetic structure factor in the plane perpendicular to the scattering vector[58]. This is due to the unique nature of magnetic scattering when the effective magnetisation components are perpendicular to the polarisation direction resulting in spin flip processes. Further this technique may be employed to distinguish between magnetic and nuclear scattering in a powder sample. D3 has no such facility and this shall be discussed no further.

6.5 Spin Flip of the Polarised beam

The sense of polarisation of the incident beam is kept by the application of a magnetic guide field parallel to the polarisation direction and perpendicular to the direction of flight. In order to alter the direction of polarisation several distinct methods have been developed. The traditional technique involves the flipping of neutrons adiabatically using a radio frequency coil to produce a magnetic field H_1 perpendicular to the neutron beam and guide field H_0[59]. The r.f. frequency is applied such that the change in resultant field direction H_0+H_1 varies less than or equal to the Larmor frequency of the precessing neutrons. When the neutrons initially enter the influence of the r.f. field their velocity is large enough to cause a very quick change in magnetic surroundings. This does not however effect the wavefunction of the neutrons that by definition must remain continuous and no change in polarisation sense is caused. This is often referred to as the 'Sudden ' approximation. By choosing the correct conditions of field, dimension and frequency the r.f. technique has been used to produce a spin flipper with a change in polarisation direction of π. The disadvantage of this method is that a time dependent polarisation is produced that changes with the r.f..

Mezei[60] developed an alternative system using rectangular coils with the application of a direct current to achieve the required results of a stable continuous flipped beam. If a neutron

is considered to enter a magnetic region produced by such a coil, by using the Sudden approximation, it can be seen that the neutron enters the field produced by the coil with unchanged spin. The field produced by the coil H_1 causes an internal field of $H_0 + H_1$ that makes an angle θ with the field outside the coil H_0. By choosing that $|H_0|=|H_1|$ and $H_0.H_1=0$ and that the transit time within the coil corresponds to the Larmor frequency then the neutron is caused to precess about $\theta=\pi/4$ and turn through $\pi/2$. By using two such coils a total change in spin direction of π is obtainable. One disadvantage of such a system is that neutrons of different velocities from that for which the coil has been specifically designed are not totally spin reversed. By setting the two coils back to back with H_1 in opposing directions in the two coils, it is possible to overcome this problem. In this case the spin of each neutron in the beam undergoes exactly the same number of Larmor precessions between entering the influence of the first coil and exiting the field of the second. In this way all neutrons of all wavelengths may be spin flipped with reference to the incident neutron spin alignment. For this technique to work well a sudden field reversal is required and interaction between the two coils must be minimal[61]. This may be achieved by placing a superconducting sheet between them. A superconductor is a perfect diamagnet (Meissner effect of a type I superconductor) below the critical field and therefore acts as a barrier between the two fields if the field in the coils is low.

On D3 the device used to invert the polarisation vector is different. The sense of polarisation is turned around by the use

of a Meissner-Majorana cryoflipper. The device is a non-adiabatic spin flipper. The magnetic guide fields as seen from the neutron's frame are reversed, in such a device, in a time much shorter than than the Larmor period. The neutron spin vector can be considered to remain fixed in the laboratory frame as it traverses the magnetic discontinuity but reversed with respect to the guide field. Figure (6.2) shows the design of the D3 instrument with reference to the magnetic fields. The polarised neutrons enter the flipper and are held in a guide field. They then traverse a region of 'free space' in which adiabatic spin change processes may take place, before again entering a well defined magnetic region. This second magnet may have a field either parallel to the first, in which case the polarisation of the beam remains the same, or in the opposing direction. If the field is different then within the region of free space the neutron spin is caused to flip. Upon entering the region surrounded by the second magnet the spin will have either flipped or remained unchanged. At the interface between the second and third magnet a superconducting sheet of niobium is used to isolate the two sections of guide field. The neutrons traverse this area, as in the case of back to back Mezei coils, without change in spin, as a result of the Sudden approximation. The third and fourth magnets act to keep the polarisation in either its new or old orientation. Beyond the influence of the free space region non-adiabatic processes only occur. The first and fourth guide fields are produced by permanent magnets on D3, whilst the other two are a product of coils with direct current. The second coil can easily be set to produce spin flip or otherwise by changing

Figure 6.2 The non adiabatic spin flipper on the D3 polarised neutron diffractometer.

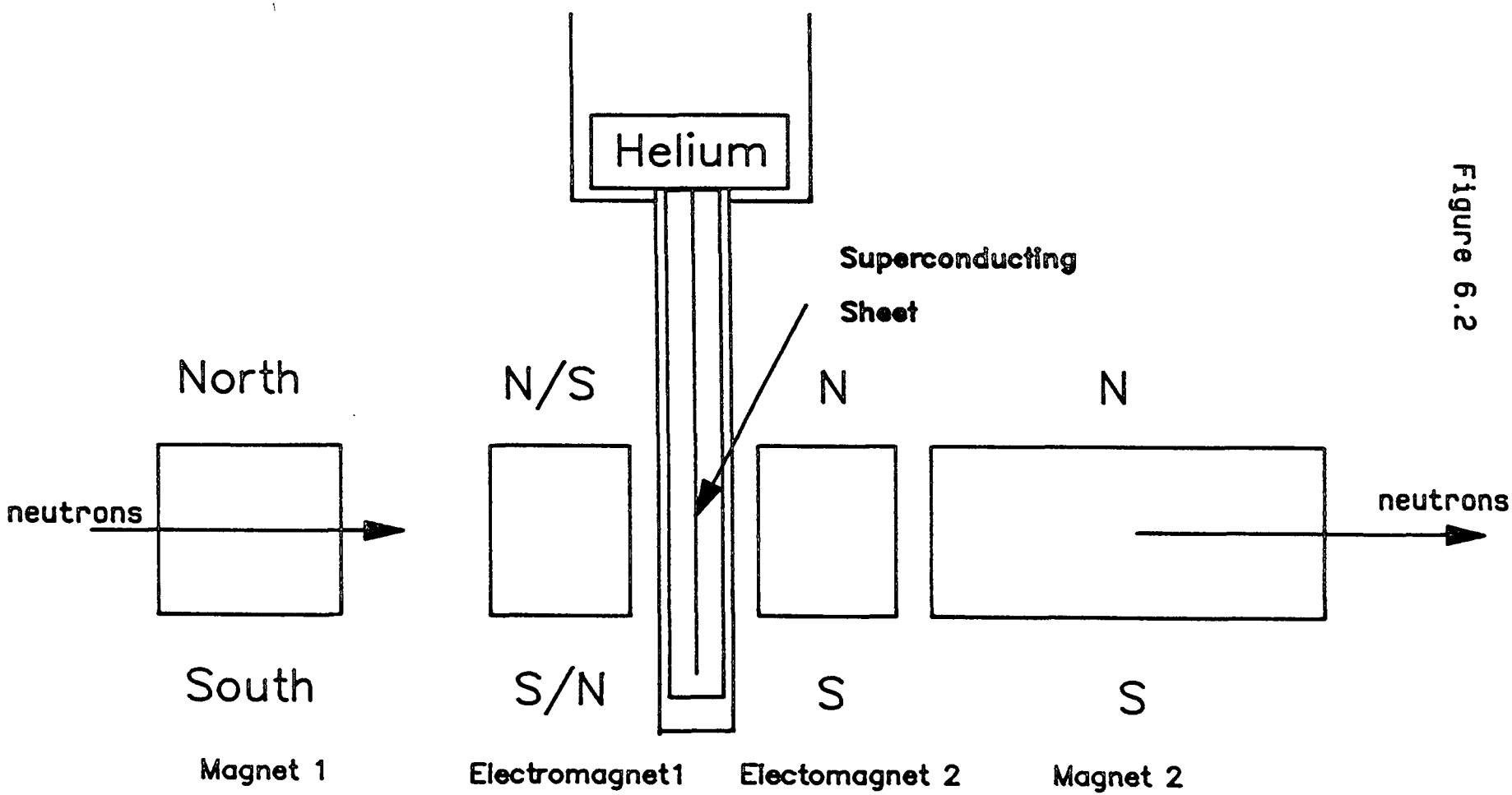
Helium
Superconducting
Sheet
North
N/S
N
N
neutrons
neutrons
South
S/N
S
S
Magnet 1
Electromagnet1
Electomagnet 2
Magnet 2

Figure 6.2

the current direction.

6.6 The Determination of the Flipping Ratio R

The cryoflipper allows the measurement of diffracted intensities of the incident beam in two spin states. The ratio of these two intensities R can be measured.

$$R = \frac{I^{+}}{I^{-}} \qquad 6.8$$

The ratio of diffracted intensities is also dependent upon the extent of polarisation of the incident beam defined through the vector quantity P. The system $ZrFe_2$ is centrosymmetric lending itself to simple analysis:

$$R(k) = \frac{I^{+}(k)}{I^{-}(k)} = \frac{|F_M^{+}(k)|^2 + |F_N^{+}(k)|^2 + 2|P|F_M^{+}(k).F_N^{+}(k)}{|F_M^{-}(k)|^2 + |F_N^{-}(k)|^2 - 2|P|F_M^{-}(k).F_N^{-}(k)} \qquad 6.9$$

If we assume that $|P^{+}| = |P^{-}| = |P| = 1$ then

$$R(k) = \frac{I^{+}(k)}{I^{-}(k)} = \frac{|F_M^{+}(k)|^2 + |F_N^{+}(k)|^2 + 2F_M^{+}(k).F_N^{+}(k)}{|F_M^{-}(k)|^2 + |F_N^{-}(k)|^2 - 2F_M^{-}(k).F_N^{-}(k)} \qquad 6.10$$

F_M is the transverse component of the magnetic scattering factor $F_M = F_M \sin\theta$ where θ, is the angle between the scattered

wavevector and the magnetisation direction. If the condition is set such that k is perpendicular to the magnetic field direction placed on the crystal, which is the case on D3, then R becomes:

$$R(k)= \frac{I^{+}(k)}{I^{-}(k)} = \frac{|F_M^{\dagger}|^2 + |F_N^{\dagger}|^2 + 2F_M^{\dagger}.F_N^{\dagger}}{|F_M^{\bar{\dagger}}|^2 + |F_N^{\bar{\dagger}}|^2 - 2F_M^{\bar{\dagger}}.F_N^{\bar{\dagger}}} = \frac{|F_M^{\dagger} + F_N^{\dagger}|^2}{|F_M^{\bar{\dagger}} - F_N^{\bar{\dagger}}|^2} \qquad 6.11$$

Since $F_M.P^{\pm}$ now becomes $\pm F_M$ it is usual to define the ratio $F_M/F_N = \gamma$. Hence $R = \frac{(1+\gamma)^2}{(1-\gamma)^2}$. If γ is small this reduces to

$$R = (1+ 2\gamma+ \gamma^2) (1 + 2\gamma +.....) \approx 1 + 4\gamma \qquad 6.12$$

Which is the case for weak itinerant ferromagnets such as $ZrZn_2$. In the case of $ZrFe_2$ the magnetic structure factors were initially unknown and this approximation was thought and indeed proved to be inconsistent with the system under investigation. γ is defined in full as one of the two roots of the equation:

$$\gamma = \frac{R + 1 \pm (2R)^{0.5}}{R - 1} \qquad 6.13$$

Thus by measuring the flipping ratio R for a given Bragg reflection the ratio of magnetic to nuclear scattering may be determined. For complete analysis an unpolarised neutron diffraction experiment, with the sample in a zero magnetic field was also carried out in order to determine the nuclear structure

factors by experiment (as well as to determine further parameters used in the analysis of the polarised neutron data as discussed later in this chapter). The D15 diffractometer at the I.L.L. was used for this purpose. Using this instrument one can measure the sum of the squares of the nuclear and magnetic structure factors.

$$I \propto F_N^2 + \frac{2F_M^2}{3} \qquad 6.14$$

The factor of 2/3 arises because 2 out of 3 components of the magnetic structure factor lie in the plane perpendicular to the incident wavevector. The nuclear structure factors may thus be determined. This in itself requires an initial approximation. One must assume that a calculated theoretical value based upon a model of Fe site only magnetism of F_M is true in order that F_N be obtained. By including an interaction between the nuclear and magnetic structure factor terms determined from polarised and unpolarised diffraction analysis the estimation of F_M becomes less critical.

6.7 Corrections to the collected data

There are two main sources of error associated with the collection of data by the diffraction of neutrons. The first type are those that arise due to the inherent incapabilities of the machine. These include $\lambda/2$ contamination of the beam due to reflection from the monochromator, momentum spread of the incident beam and in the case of polarised neutrons incomplete

polarisation. The second source of errors are those that arise from imperfections in the specimen used for study. Examples of this type of problem are depolarisation and absorption of the beam along with multiple scattering and extinction. In order to obtain results from the data, corrections and refinements have been carried out using a computer. During the course of the data analysis programs and subroutines of the Cambridge Crystallographic Subroutine Library (CCSL) have been extensively used[62]. Using this program suite these corrections have been relatively easy to make.

6.8 Correction Overview

The errors due to spin reversal and imperfect polarisation are discussed by J.B. Forsyth[63]. The extent of polarisation from the $Co_{98}Fe_{8}$ monochromator is well known. If the depolarisation coefficient is D and ϵ is the flipping efficiency the equation for R can be solved for $\gamma = \gamma\sin\theta$ where θ is the angle between the polarisation vector and the scattering vector $\mathbf{k}$[64].

$$\gamma = x(\epsilon+1) + \frac{(x^2(\epsilon+1)^2-(R-1)^2)}{R-1} \qquad 6.15$$

where

$$x = P_i DF'_N \sin\theta |F_N| = P_i D\sin\theta \qquad 6.16$$

for a centrosymmetric system. P_i is the incident polarisation F_N' is the real part of the nuclear scattering factor and $|F_N|$ is the modulus of the nuclear structure factor. D is different for each reflection and is calculated by

$$D = \int_{\substack{\text{crystal} \\ \text{volume}}} \exp(\zeta d)\, dv \qquad 6.17$$

$$\zeta = \frac{1}{t} \ln \frac{P_i}{P'} \qquad 6.18$$

and the transmitted polarisation P' is measured for a sample thickness t[64]. The effect due to depolarisation may be reduced by using a crystal that is orientated in the magnetic field of the cryomagnet such that the sample is magnetised along an easy direction. By using a sample with a large aspect ratio the path length of the neutrons inside the crystal can be reduced thus reducing the effects of absorption. By using a sample of this kind saturation of the sample in the magnetic field of the D3 experiment is more likely.

The $\lambda/2$ contamination of the incident beam is negligible when using an incident beam of $\lambda<1$Å and a CoFe monochromator.

The last of the corrections and probably the most difficult to solve is the one of multiple scattering. This gives rise to extinction at large scattering intensities and evidence of flipping ratios at systematically absent reflections. These corrections apply equally to diffracted intensities from a

polarised neutron experiment as to an unpolarised one. Any corrections for extinction or multiple scattering have been calculated for the D15 data and carried over to the D3 data. For this process to be valid the same crystal in the same orientation at the same temperature (4.2K) has been used in both experiments.

Corrections for multiple scattering, other than the special case of extinction, are difficult to make and have not been undertaken in this work. The extent of extinction in a sample is modeled through the mosaic spread.

6.9 The Mosaic Spread

If the single crystal used in this experiment were perfect all incident neutrons would be Bragg scattered within a few atomic layers of entering the crystal and most of the sample would only be irradiated by previously scattered neutrons. Thus multiple scattering would make the experiment very difficult if not impossible. This is referred to as primary extinction. This problem is surmounted by the use of crystals that posses a mosaic. In this situation , as pointed out by Darwin[66], the whole is made up of small blocks formed by dislocations. These small blocks show a spread of slight misorientations from one another. Thus incident neutrons are scattered at slightly differing Bragg angles from each block allowing deep penetration of unscattered neutrons into the crystal. Therefore the collected intensity is increased since a greater angular range of reflections are observed at the collector. As the beam penetrates if the crystal is thick the

scattered neutrons have a greater probability of striking a second crystallite with the same orientation as the first. This may cause what is known as secondary extinction. An ideal sample for this type of experiment has a size and mosaic such that secondary extinction is the only type that need be considered.

The Becker Coppens model of extinction[67] has been used to predict the extent of the correction required to the collected intensity. The crystal is modeled as a collection of mosaic blocks with a distribution of orientation described by the Lorentzian line shape. For this purpose two parameters are introduced one to describe the domain radius and the other the distribution. It should be noted that the effects of extinction and multiple scattering are distinct from that of absorption where the neutrons are captured and result in the production of γ-ray emissions. Corrections for absorption of the beam can be made if necessary if the absorption coefficients are known.

6.10 The Unpolarised Neutron Experiment

To obtain nuclear structure factors a set of integrated intensities must be measured using an unpolarised neutron diffractometer. In order to determined the observed values of the nuclear structure factors from these integrated intensities several stages of correction and refinement are required.

As previously mentioned the collected data from such an experiment for a magnetic sample actually corresponds to the sum

of the squares of the nuclear structure factors for the nuclear and magnetic parts. To help in the analysis of the magnetic system the C.C.S.L has kindly been extended to take this into account[68].

6.11 The Incident and Monochromated Beam

When considering the collection of data from a diffractometer the experimental resolution of the peak is of primary importance. From this peak and its integrated intensity must be deconvolved the nuclear structure factors. In the simplest situation the incident neutrons at the sample consist of all one wavelength and when scattered by an ideal crystal produce a δ function type response. This is not the situation when considering scattering using a real machine. The collimation, mosaic of sample and crystal monochromator are all finite. This produces a finite width in both wavelength and real space spread.

The incident thermal neutrons enter the diffractometer as a collimated beam. They then strike the monochromator that posses mosaic that is a result of the necessity for the production of an intense beam. This results in the production of a wavepacket, at any given instance at the monochromator, that has width in wavelength defined by the mosaic and collimation. On leaving the monochromator the beam hits the sample, that itself has mosaic which further acts to broaden the beam in both angular spread and momentum. To obtain results that are independent of the mosaic of the monochromator the integrated intensities of the scattered beam

are measured. To achieve this the crystal is rotated by a stepper motor and intensities measured so that all components of the primary beam are diffracted by all parts of the crystal. The detector used for this purpose must satisfy the condition that it is larger than the angular divergence of the crystal.

By convoluting the distribution of the incident collimated beam upon the monochromator with that for a perfect crystal the momentum packet of the monochromated beam may be obtained. The same results may alternatively be achieved by convoluting the distribution for a fully collimated beam with that for a crystal with finite mosaic spread. By doing this and considering the half width for a perfect crystal[69] it is possible to obtain the half width of the resulting rocking curve.

$$\Delta\omega^2 = \alpha_1\left(1 - \frac{\tan\theta}{\tan\theta_1}\right)^2 + \zeta_1^2\left(2 - \frac{\tan\theta}{\tan\theta_1}\right)^2 + \zeta_2^2 \qquad 6.19$$

Where ζ and ζ_1 are the mosaic of the crystals (ζ=0 for a perfect crystal) and α describes the collimation (α=0 for perfect collimation). θ and θ_1 are the Bragg angle and average scattering angle of the monochromator. It can further be shown that the resulting monochromatic beam has a bandwidth given by

$$\frac{\Delta\lambda}{\lambda} = \Delta\theta\cot\theta_1 + \frac{\Delta d}{d} \qquad 6.20$$

Where Δd is the variation in lattice constant of the

monochromating crystal. In order to obtain the required characteristic beam the monochromator may be designed with required mosaic, lattice constant gradient and curvature. These conditions are discussed in some detail by Dachs[69].

The neutron scattering factors may be related to the magnitude of the collected integrated intensities[69] by $N_0\lambda^3 Lp|F|^2\delta v$ where N_0 is the number of unit cells per unit volume, p is the polarisation factor and L is the Lorentz factor. The Lorentz factor accounts for the resulting spread of incident wavevectors that arrive at the sample. Any mosaic properties of the sample are dealt with independently of this factor. By definition the Lorentz factor is a geometrical term that corrects for the differing rates at which the reciprocal lattice points sweep the area of reciprocal space defined by the Ewald sphere construction that represents all possible reflections for the incident beam when the crystal is rotated at constant angular velocity about the ω axis. This in effect means that at differing reflections the collected integrated intensity vary by a factor that is dependent upon the Bragg angle. For scattering from a single crystal in normal beam equatorial geometry of the diffractometer

$$L = \frac{1}{\sin 2\theta} \qquad 6.21$$

In general, for example in 4-circle geometry

$$L = \frac{1}{\cos\alpha\cos\zeta\sin\gamma} \qquad 6.22$$

For normal beam geometry $\gamma=2\theta$, $\alpha=\zeta=\pi$. In this way the collected intensities may be corrected for momentum spread in the real system.

As previously discussed the resulting collected intensities must be corrected for mosaic spread and thermal vibrations of the specimen crystal. To obtain nuclear structure factors it is therefore necessary to least squares fit the Lorentz corrected intensities to the theoretical values. This is achieved in two stages using the C.S.S.L.. The two parameters describing the extinction and multiple scattering factors are estimated, the domain radius is set to a fixed large value. The isotropic temperature factors w_i and the linear scaling factor are then used as variables. From the resulting observed nuclear structure factors the final structure factors are obtained by use of the Becker Coppens model of extinction.

6.12 The Polarised Neutron Experiment

Investigation into the magnetic distribution is carried out using the polarised neutron technique. The results from this type of experiment require similar corrections and refinement to those used on D15 data. A simplification to these modifications arises through the need for the determination of a ratio. This makes unnecessary the stages associated with the determination of

absolute structure factors from the collected integrated intensities. Corrections for extinction, absorption and multiple scattering are still required, however the values of the parameters describing these phenomena for unpolarised scattering are equally relevant for scattering of a polarised beam and the results may be carried across. This requires that the same crystal be used for both experiments.

The D3 instrumentation is fully computer controlled. The sample is held in a steady field and temperature environment using a split coil cryomagnet. Once the crystal is located inside the cryomagnet it becomes essential to define its position and orientation in real space. The shafts of the diffractometer are set according to the crystal orientation and reflection conditions.

The determination of the orientation is achieved by locating several strong reflections and describing the crystal sense using a matrix. From this so called UB matrix[70] the machine is then able to locate the required positions of the detector and crystal such that any predefined Bragg reflection is found.

The precise position of the peak varies from that defined by the UB matrix and the shaft settings. This in general is due to several compound effects such as: a slightly incorrect matrix; sample location within the magnetic field and an imperfect crystal. It is essential that the peak of the rocking curve is located for the production of good flipping ratios with small

errors.

The precise position of the peak is found by moving the crystal about the ω-axis whilst keeping the shaft settings and detector position constant. In taking measurements at these slightly different settings the peak position may be located. Measurements for incident up and down spin states are collected at this stage in order that time for further investigation may be allotted efficiently. The time for each scan is set by the user at this stage. In this case scans of 5.7 seconds proved adequate.

Once located the counting of flipping ratios can begin. The actual intensities measured are a combination of the required intensity and background. The background rate must be determined and subtracted from the signal. This is achieved by collecting intensities either side of the peak and subtracting from the main peak intensity.

The background may be different for the two incident spin polarisations and thus to compensate background scans taken some $1\text{-}4^{o}$ either side of the Bragg peak beyond the rocking curve are taken for both spin up and spin down states.

The optimum time distribution for the complete collection is determined such that the time spent collecting the 4 data sets for the reflection and background are measured to an accuracy that contributes an equal weighting to the estimated error.

The up to down time ratio is used to determine the amount of time spent counting within each measurement cycle. Each cycle consists of a period of some 1 to 2 seconds in which time the spin is flipped once and the scattered intensities are collected in separate counters.

6.13 Further Corrections

There are two potential problems that must be appreciated and if necessary corrected for that originate as a result of the superconducting cryo-magnet.

It can be shown that a force is present on a neutron as it passes through a magnetic field gradient[71]. The direction of this force is opposite for the two different polarisation states. This results in a change in velocity of the neutrons, the direction of which depends on the spin state. This amounts to a difference in wavelength and thus a change in Bragg angle for the two states. Moon has given an equation for this in the form of an error in the observed flipping ratio. It turns out that if the crystal is positioned such that the change in rocking curve with angle is zero or small that this problem becomes of little significance.

$$\Delta R d\theta = - \frac{2|\mu_N| H \tan\theta}{m_N v^2 \, \eta(\theta)} \, d\eta(\theta) \qquad 6.23$$

Where H is the central field, v is the neutron velocity and $\eta(\theta)$ is the rocking curve distribution. The ideal crystal for

such an experiment has a rocking curve with a flat top distribution in light of this error and the difficulty in holding the sample steady in a large magnetic field.

The second problem arises from a requirement for the production of an asymmetrical field using the split coil magnet available on D3. This asymmetry is incorporated into the design of the magnet so that no zero field regions exist along the neutron flight path that may cause depolarisation of the beam. This results in the production of a vertical field that causes separation of the two spin states in the same way as the Stern Gerlach experiment. It can be shown[72] that the angular separation of the two beams in the vertical plane is given by:

$$\Delta(\uparrow,\downarrow) = \frac{2|\mu_N|}{m_N v^2} \int_{\text{neutron path}} \frac{\delta H}{\delta z} dz \qquad 6.24$$

This effect may be of little significance if the crystal is orientated such that the reciprocal lattice vector is in the horizontal plane since any divergence in the beam is easily collected at the detector. However if this is not the case any slight misorientation may result in an incorrect flipping ratio. By masking out alternatively the top and bottom halves of the scattered beam at the detector the measured results show equal error but in opposing directions. Thus the effect may be accounted for.

CHAPTER 7

Magnetisation Density Distribution in $ZrFe_2$

7.1 Introduction

The binary metal alloy $ZrFe_2$ is magnetic with a $MgCu_2$ (C15) cubic Laves phase structure which is stable over a narrow range of composition about the ideal 66.7 atomic percent iron. The space group is Fd3m with Z=8. This structure may be described in two ways depending upon the position of the centre. With the centre (3m) at the origin, the atomic positions are fixed at:

Table 7.1

Atom	Site	Symmetry	x	y	z
Fe	16(d)	$\bar{3}$m	0	0	0
Zr	8(a)	$\bar{4}$3m	1/8	1/8	1/8

The structural stability has been investigated by Brukner et. al.[73] and related to changes in cell dimension and bulk magnetic properties by Bruckner et. al.[74] and by Kai et. al.[75]. The latter authors find a much narrower range of stability for the C15 structure from 66.0 to 67.2 at% Fe and a range of stability for the hexagonal phase ($MgNi_2$) Laves phase from 68.6 to 72.7 at% Fe, whearas the study by Bruckner at. al. associate the whole range 66.0 to 73.0 at% Fe with the cubic phase. Despite these differences, there is general agreement on the rates of change of

cell dimension, Curie temperature (T_c) and saturation magnetisation (σ_m) with iron concentration in the ideal composition region, which is characterised by T_c = 600K, σ_m = 3.09 μ_B/formula unit at 4.2K and a cell dimension of 7.070[75] or 7.089 Å[73]: these rates are some -0.012 Å, 36°C and 0.048μ_B per at% increase in Fe concentration, receptively. There is some indication that the rates of change in the Curie temperature and saturation magnetisation change at the ideal composition, being lower than the average values quoted above 66.7 at% Fe and higher on the Fe-rich side of $ZrFe_2$.

The saturation magnetisation of $ZrFe_2$ at room temperature (300K) has been reported by Peigger and Craig[76] and also by Bruckner et. al.[74]: both sets of authors find a value of 2.6 μ_B/formula unit at the composition $ZrFe_2$, though the rate of change of this quantity with composition is much higher (0.25 μ_B /at% increase in Fe) than at low temperature due to the relative proximity of the composition dependent T_c. An ambient temperature polarisation neutron study by Kocher and Brown[77] on a large grained, polycrystalline specimen found that the moment distribution at the Fe site corresponded to a more extended form factor than that in α-iron and that there was no significant moment at the Zr site. No value for the iron moment was given but the saturation magnetisation at 4.2K and ambient temperature were measured as 3.12 and 2.56 μ_B/formula unit, respectively.

7.2 Theoretical Background of $ZrFe_2$

Three theoretical band structure calculations and their unique solutions have been focused upon. These three models agree with each other and also with experimental results, within the accuracy of the methods employed, in the absolute value of the integrated saturation magnetisation. However the calculated local moments differ for each calculation.

Klein et. al.[78] used a rigid band splitting mean field Stoner model. The calculated moment in the system is some three times too small. This short fall has been attributed to the presence of covalent magnetisation[79].

The concept of hybridisation of orbitals has been used in the calculations of Yamada and Shimuza[80] and Mohn and Schwartz[81] to predict the existence of a negative magnetic moment at Zr atom sites. The Mohn and Schwartz model is based upon self consistent, non relativistic, spin polarised band structure calculations utilising the augmented spherical wave methods of Willaims et. al.[79] and predict a diffuse negative moment at the Zr atom sites with 20% contribution to the total moment originating from s and p orbitals. This model has been used to predict the valence core states of the system allowing quantities such as the hyperfine field to be estimated[82]. Armatage at. al.[83] have performed measurements on the forced magnetostriction of $ZrFe_2$ and justified the existence of a ferrimagnetic ground state through the use of this model.

Yamada and shimuza based their theory upon the tight band structures of d electrons using the tight binding limit[84] and justified neglecting d states with s and p hybridisation through the work of Klein et. al. where they showed that greater than 92% of the local density of states of either atom is due to the d electrons alone. The existence of a negative moment associated with the Zr atoms is explained through the hybridisation of 3d and 4d electron orbitals. The predicted moment distribution is less diffuse than that predicted by the Mohn and Schwartz model.

Table 7.2

Moments (μ_B/atom)	Klein et. al.	Mohn et. al.	Yamada et. al.
Fe	1.62	1.9	1.87
Zr	0	-0.56	-0.53
Total (μ_B/Fe atom)	1.62	1.62	1.61

7.3 Experimental

A single crystal study of $ZrFe_2$ is reported in which unpolarised neutron diffraction data have been used to determine its thermal parameters at 4.2K and to characterise the small degree of extinction present in the sample. These data have been used with polarised neutron flipping ratio measurements, made at the same temperature, to obtain an accurate description of the spatial distribution of magnetisation in the compound. This

experiment provides the first single crystal experiment capable of resolving the inconsistencies of the described theoretical works.

A similar experiment has been reported on the C15 intermetallic alloy $LuFe_2$ using a single crystal[85]. Enough data was collected to enable fourier density maps of the magnetisation to be constructed. The work concluded that there was no evidence of a magnetic moment at the rare earth atom sites whilst the magnetisation distribution around iron sites is tetragonal. This is consistent with the tetragonal configuration of the Fe atoms within the lattice work. The presence of a tetragonal crystal field resulting in the removal of the 5-fold 3d degenerate orbits into a singlet and two doublets. This description accounts well for the observed magnetisation distribution and a difference between the integrated moment at the Fe sites and that measured using bulk magnetisation measurements was attributed to electron polarisation effects.

The bulk single crystal was grown as part of this work. Its growth is discussed in detail in chapter 4.

Its saturation magnetisation has been determined using a V.S.M., discussed in chapter 5, and is $3.26\mu_B$/formula unit at 4.2K. Both unpolarised and polarised neutron diffraction measurements have been made at 4.2K on a single crystal pillar elongated parallel to the $<1\bar{1}0>$ direction, corresponding to the magnetisation easy direction, with dimensions 1x0.5x0.5 mm. The former data was collected using the D15 diffractometer at the

Institut Laue Langevin (ILL), Grenoble. In the determination of the UB matrix that defines the position of the crystal and its orientation in the 4 circle diffractometer so that Bragg reflection may be located by the control computer in real space, the cell dimension has been determined. With an incident wavelength of 1.171Å, 11 strong reflections have been located manually in order to determine the orientation matrix and a cell paramter a_0 of 7.05(2)Å found. With the neutron wavelength set to 0.8519Å the same result has been determined. A total of 396 reflections were measured out to a $\sin\theta/\lambda$ limit of $1.0Å^{-1}$: after averaging over equivalents , which gave a merging R factor of 2.97% on F^2 and a X^2 of 19 using an incident neutron wavelength of 1.1713(48)Å, the 97 inequivalent observed moduli of structure factors were used in a weighted least squares refinement of a model in which the variables were the isotropic temperature factors on Zr and Fe, the Fe magnetic moment, a scale factor and a mosaic spread parameter to describe the small degree of extinction in the sample using the Becker-Coppens formalism (see chapter 6 for a complete description). The weighting scheme was $1/\sigma^2$, where σ is the standard deviation in the structure factor derived from the agreement between equivalent reflections.

$$R_w^2 = \frac{\sum_i \left(\alpha_i |F_i^2(obs) - F_i^2(calc)|^2 \right)}{\sum_i \alpha_i F_i^2(obs)} \qquad 7.1$$

Where α is equal to the reciprocal of the standard deviation squared.

The form factor for the Fe moment was derived from the wavefunction for Fe 3d given by Clementi and Roetti[86]. In the refinement, Zr was assumed to carry no moment and the excellent final R-factor of 1.08%, Weighted R factor, R_w=1.03% and X^2=2.6 showed that the data are not sensitive to the presence of a small moment at the Zr site. The refined values for the temperature factors and the mosaic spread, which are listed in table 7.1, were then used to derive the observed magnetic structure factors from the polarised beam flipping ratios measured on the D3 instrument, also at the ILL. These measurements were made with an incident wavelength of 0.84Å and in a field of 1.5T, sufficient to saturate the sample with its pillar axis vertical, parallel to the ω axis of the normal beam instrument and to the applied field direction. The UB matrix , determined from the position 11 Bragg reflections revealed an a_0=7.07(2). A total of 283 flipping ratios were averaged over the equivalent reflections to produce 55 unique structure factor, corrected for imperfect incident beam polarisation (0.975)

7.4 The Moment Distribution

The magnetic moment structure factors derived from the D3 measurements provided the observed data for an initial weighted least-squares refinement of a magnetic model with the form factors specified above. The final R-factor was 11.1%, R_w=8.5% and a X^2 of 23 with Fe and Zr moments of 1.79(4) and -0.16(8) μ_B, respectively. The weighted scheme was as before. At this stage

in the refinement there was no indication of a significant expansion or contraction of the observed form factor relative to the model. One reflection, 1 1 1, has a magnetic structure factor close in magnitude to its nuclear one. In these circumstances, the polarised beam technique gives poor accuracy and this reflection was omitted from the refinement leaving 54 observed magnetic structure factors. Difference Fourier sections, calculated from the observed structure factors, parallel to (001) through both the Fe and Zr atoms were computed in the belief that they would show the deficiencies of our model: in the latter case, since these would be most affected by a weak moment on the Zr. There is little visual indication of an aspherical distribution in magnetisation density from the Fourier maps (figures 7.2 to 7.7), that show a set of orthogonal planes through the lattice viewed from different positions. The magnitude of the moment predicted from band structure calculations would be expected to distort the moment distribution around the Fe atom sites from spherical and the negative moment distribution at the Zr atom sites should be clearly observed.

Departure from the spherical symmetry in the spatial distribution of the magnetisation about the centre of a magnetic atom can result from the action of the crystalline field. To investigate this possibility, the moment distribution centred on the Fe was modeled by a multipolar expansion of the products of spherical harmonics and radial integrals, $\langle j_n \rangle$. The site symmetry in 3m which leads to three independent mutipoles Y_{20}, Y_{40} and Y_{43} (referred to quantum axes Z parallel to [111] and X parallel to

[1$\bar{1}$0]) in addition to the $Y_{00}\langle j_0\rangle$ spherical term. A significant improvement in fit was obtained by refining the amplitudes of these products: R=7.9%, R_w=5.1% with X^2=9 for 6 basic variables and the 54 observations. Table 7.2 gives the values of the parameters of this model and their standard deviations, there is a slight but barely significant indication of some expansion of the Fe radial form factor as indicated by the coefficient for $\langle j_2\rangle$ which was added to $\langle j_0\rangle$ to model this effect.

The level of sphericity around the Fe sites is remarkable on two accounts. First the presence of a barely significant moment at the Zr site has no effect on the distribution, this is understandable when one compares the magnitude of the ratio of the moments at the two sites. Secondly and perhaps more significantly the radial distribution is surprising in its uniformity being close to that associated with free Fe^{2+} rather than that observed in $LuFe_2$ that follows a distribution associated with the tetragonal distribution of the Fe atoms.

The relevence of these results andconclusions to the ground state of $ZrFe_2$ magnetism are based upon the assumption that no metamagnetic phase transition occurs with the application of a large external magnetic field. This is supported by the bulk magnetisation measurements of Y. Muraoka et. al.[96] in fields upto 50KOe.

TABLE 7.1

The refined parameters for the structure of $ZrFe_2$ at 4.2K derived from the unpolarised neutron integrated intensity data.

Atom	Parameter	Value
Fe	ITF	0.12(1) $Å^2$
	moment	1.63(5) μ_B
Zr	ITF	0.15(1) $Å^2$
	moment	0
	mosaic spread	$0.077(3)\times10^{-4}$ radians^{-1}

TABLE 7.2

The multipole amplitudes and their standard deviations for the best fit to the magnetisation in $ZrFe_2$.

Fe	Y_{00}	$1.68(3)\langle j_0\rangle+0.027(22)\langle j_2\rangle$
	Y_{20}	$0.03(2)\langle j_0\rangle$
	Y_{40}	$0.16(4)\langle j_0\rangle$
	$Y_{4\bar{3}}$	$-0.30(4)\langle j_0\rangle$
Zr	Y_{00}	$-0.21(4)\langle j_0\rangle$

TABLE 7.3

Some of the experimental iron structure factors determined from the polarised neutron flipping ratios calculated on the basis that the moment on the Zr atoms is zero. The type of reflection corresponds to the theoretical structure factors $N(q)=\sum_j b_j \exp(iq.R_j)\exp(-W_j)$ where the sum is over all the atoms i the unit cell with position R_j and b and W denote the scattering length and the Debye Waller factor respectively where $W_j=w_j(\sin^2\theta)/\lambda^2$ with the temperature factor w_j used in the refinement of data. If the scattering lengths for Fe and Zr are b_{Fe} and b_{Zr} respectively then $a=b_{Fe}-b_{Zr}/\sqrt{2}$, $b=b_{Zr}$, $c=b_{Fe}+b_{Zr}/\sqrt{2}$, $d=2b_{Fe}$, $e=2b_{Fe}-b_{Zr}$, $f=2b_{Fe}+b_{Zr}$.

reflection	$\sin\theta/\lambda$	type	$\lvert\mu f\rvert_{Fe}$
111	0.13	a	1.36
311	0.24	c	1.13
222	0.246	d	1.03
400	0.28	e	0.933
511	0.37	c	0.645
440	0.4	f	0.49
533	0.465	c	0.351
444	0.491	e	0.299
551	0.507	c	0.274
711	0.51	a	0.27
731	0.545	c	0.255
800	0.57	f	0.22
880	0.80	f	-0.06
12 00	0.85	d	0.033
888	0.9827	f	0.0728

Figure 7.1 Positions of the Fe and Zr atoms in the unit cell of $ZrFe_2$ which has the cubic C15 structure.

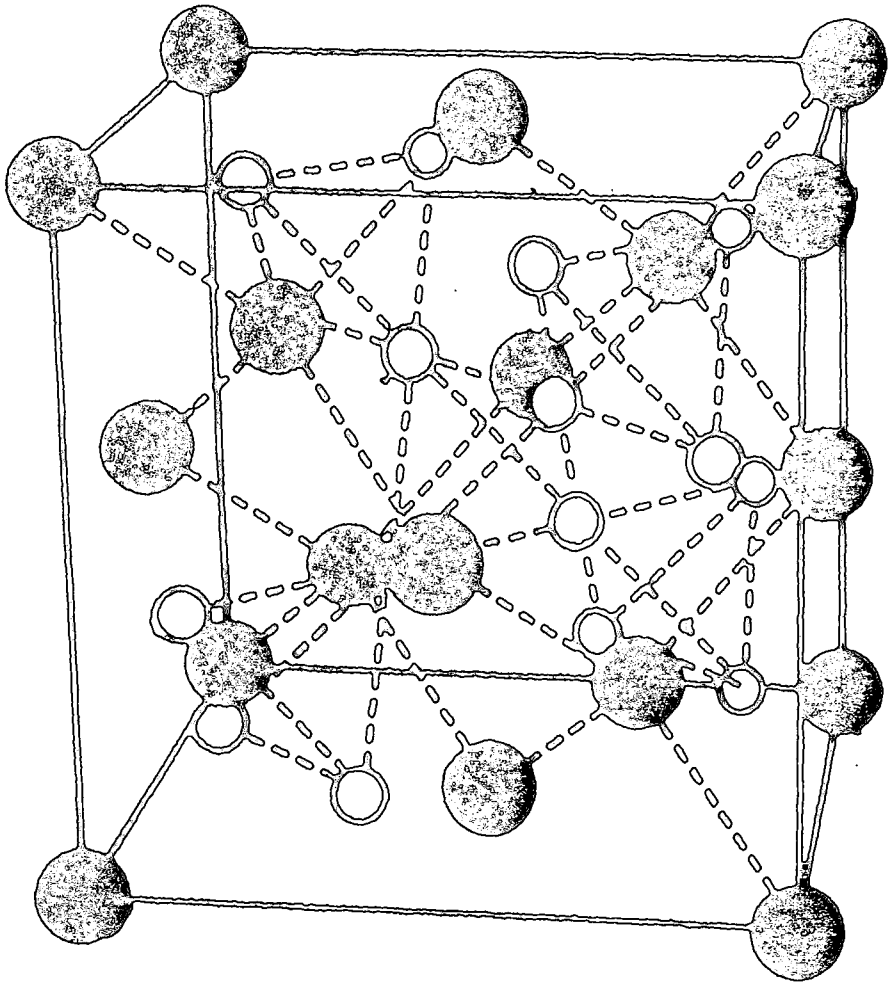

Figure 7.1

Figures 7.2 to 7.7 Magnetisation density maps in real space of the cubic C15 binary alloy $ZrFe_2$ with the contours $0.2\mu_B$ apart for the Fourier transforms of the experimentally determined structure factors out to $\sin\theta/\lambda=1\text{Å}^{-1}$.

Figures 7.2 shows the fourier density map through the $(1\bar{1}0)$ plane passing through the origin with different axes. Views through the orthogonal planes $(\bar{1}10)$ and $(11\bar{2})$ also passing through the origin are shown in figures 7.2 and 7.3 respectively

Figures 7.5,7.6 and 7.7 show sections through the orthogonal planes $(\bar{1}10)$,$(\bar{1}\bar{1}\bar{1})$ and $(11\bar{2})$ respectively.

Figure 7.2

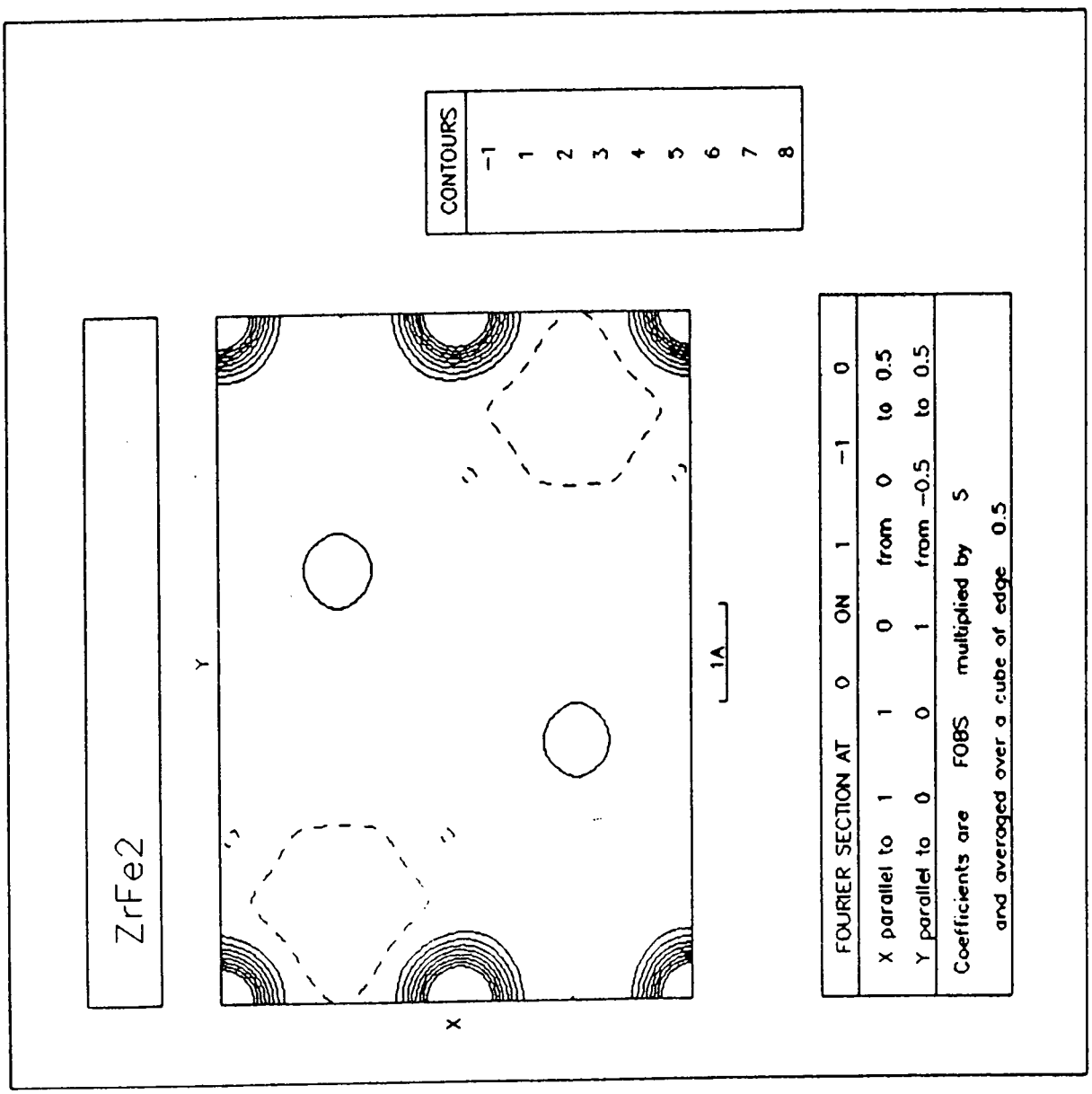
ZrFe2
CONTOURS
-1
1
2
3
4
5
6
7
8
Y
X
1A
FOURIER SECTION AT 0 ON 1 -1 0
X parallel to 1 1 0 from 0 to 0.5
Y parallel to 0 0 1 from -0.5 to 0.5
Coefficients are FOBS multiplied by 5
and averaged over a cube of edge 0.5

Figure 7.3

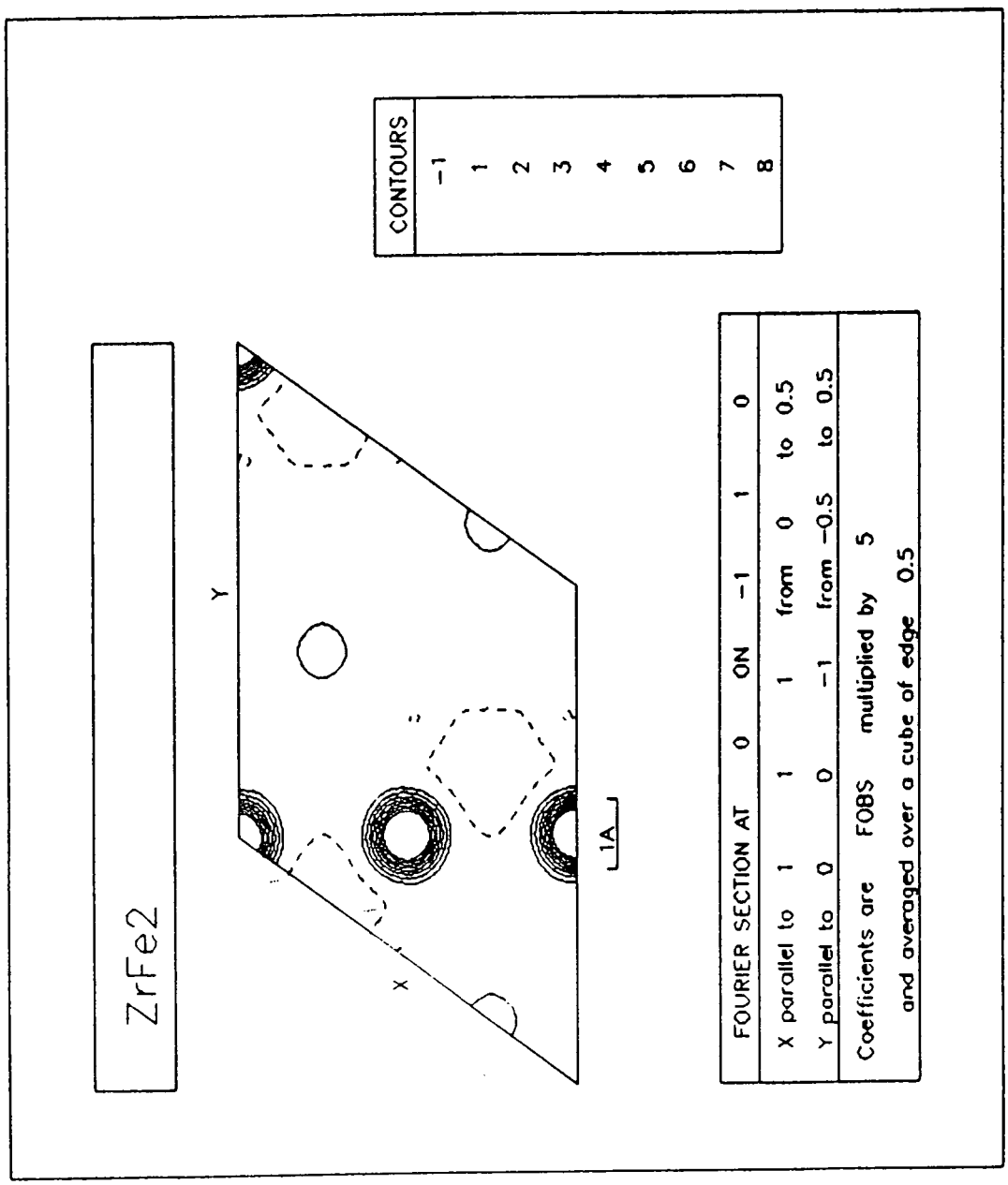
ZrFe2
Y
X
1A
CONTOURS
-1
1
2
3
4
5
6
7
8
FOURIER SECTION AT 0 ON -1 1 0
X parallel to 1 1 1 from 0 to 0.5
Y parallel to 0 0 -1 from -0.5 to 0.5
Coefficients are FOBS multiplied by 5
and averaged over a cube of edge 0.5

Figure 7.4

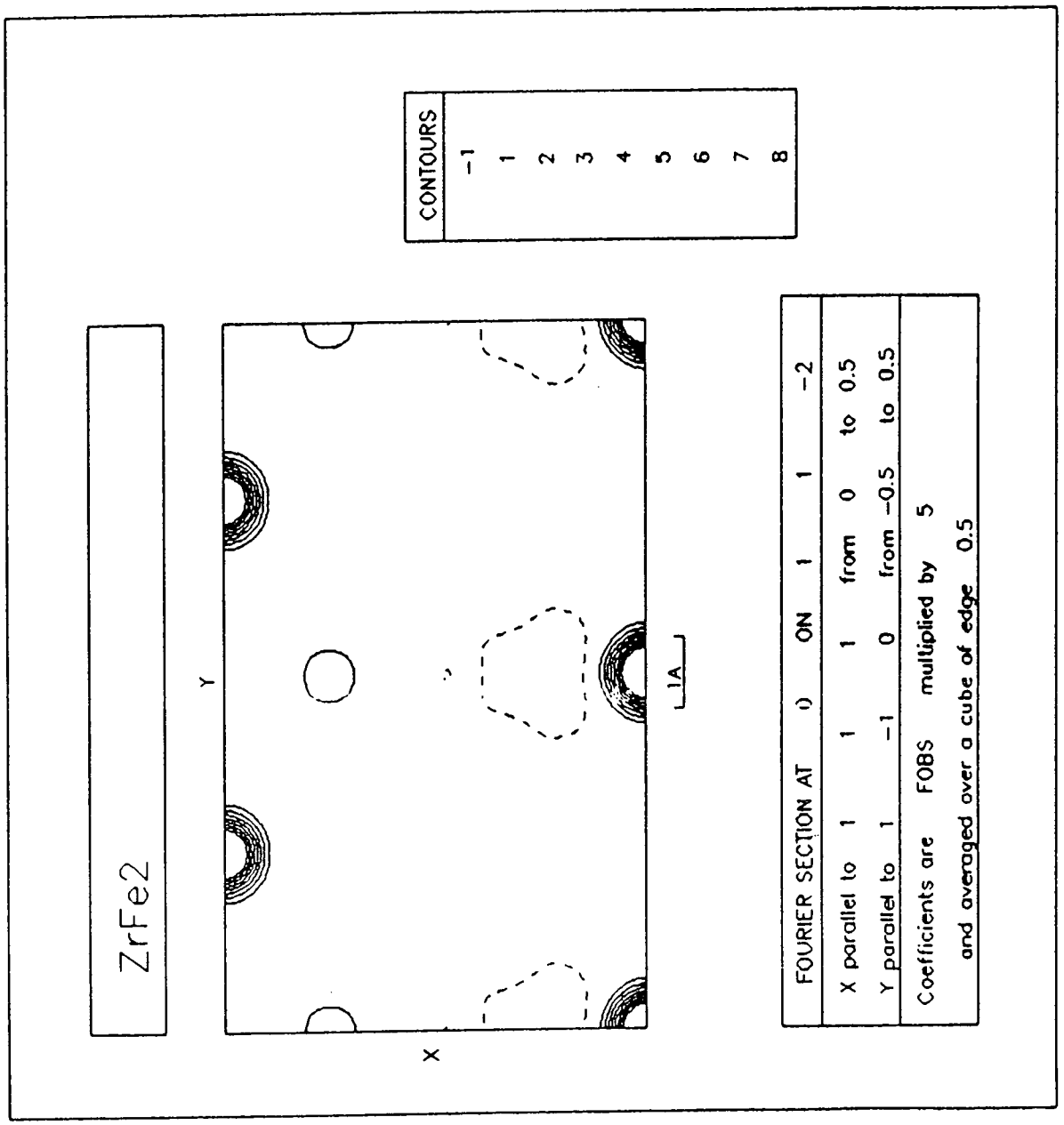
ZrFe2
Y
X
1A
CONTOURS
-1
1
2
3
4
5
6
7
8
FOURIER SECTION AT 0 ON 1 1 -2
X parallel to 1 1 1 from 0 to 0.5
Y parallel to 1 -1 0 from -0.5 to 0.5
Coefficients are FOBS multiplied by 5
and averaged over a cube of edge 0.5

Figure 7.5

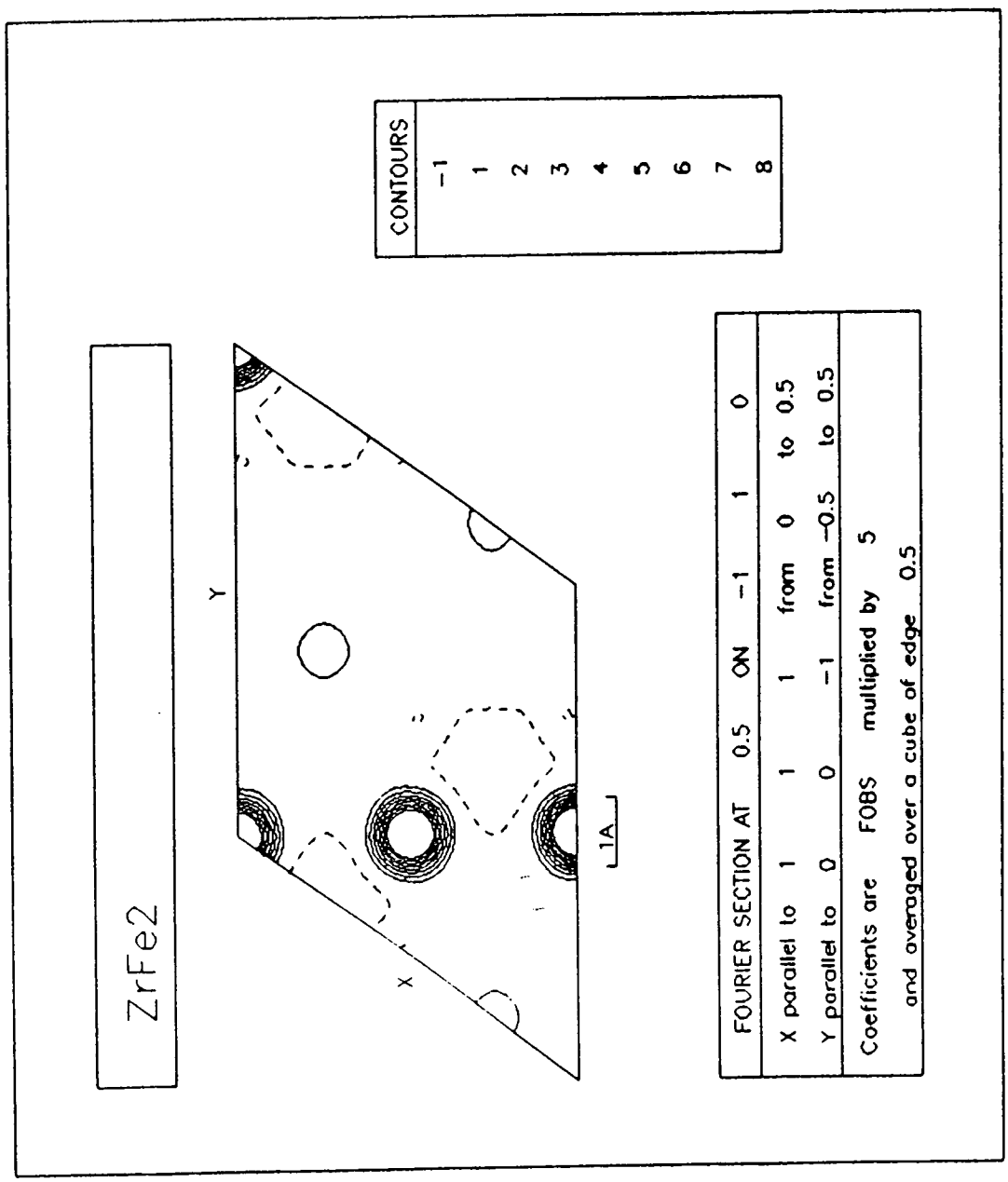
ZrFe2
Y
X
1A
CONTOURS
-1
1
2
3
4
5
6
7
8
FOURIER SECTION AT 0.5 ON -1 1 0
X parallel to 1 1 1 from 0 to 0.5
Y parallel to 0 0 -1 from -0.5 to 0.5
Coefficients are FOBS multiplied by 5
and averaged over a cube of edge 0.5

Figure 7.6

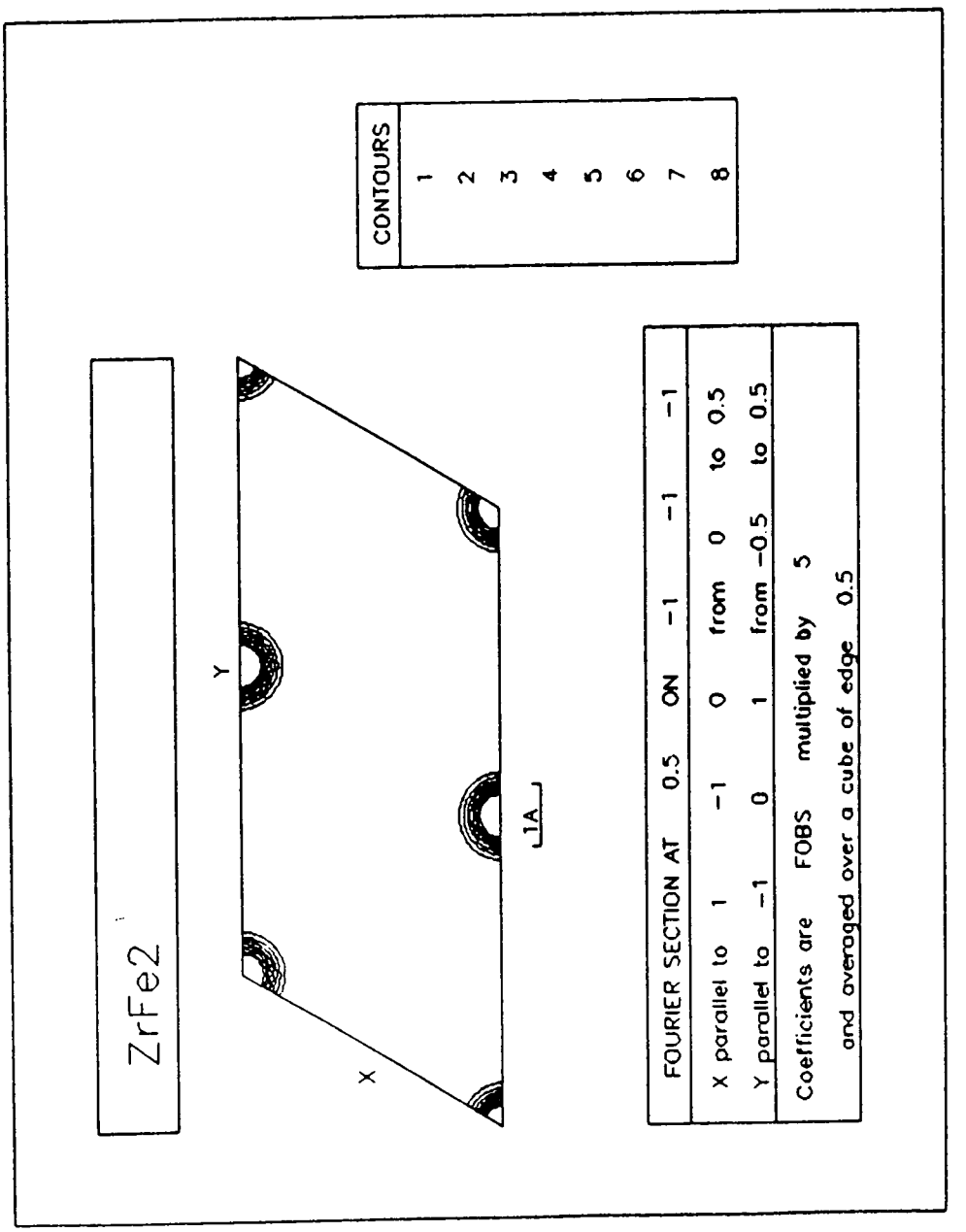
ZrFe2
Y
X
1A
CONTOURS
1
2
3
4
5
6
7
8
FOURIER SECTION AT 0.5 ON -1 -1 -1
X parallel to 1 -1 0 from 0 to 0.5
Y parallel to -1 0 1 from -0.5 to 0.5
Coefficients are FOBS multiplied by 5
and averaged over a cube of edge 0.5

Figure 7.7

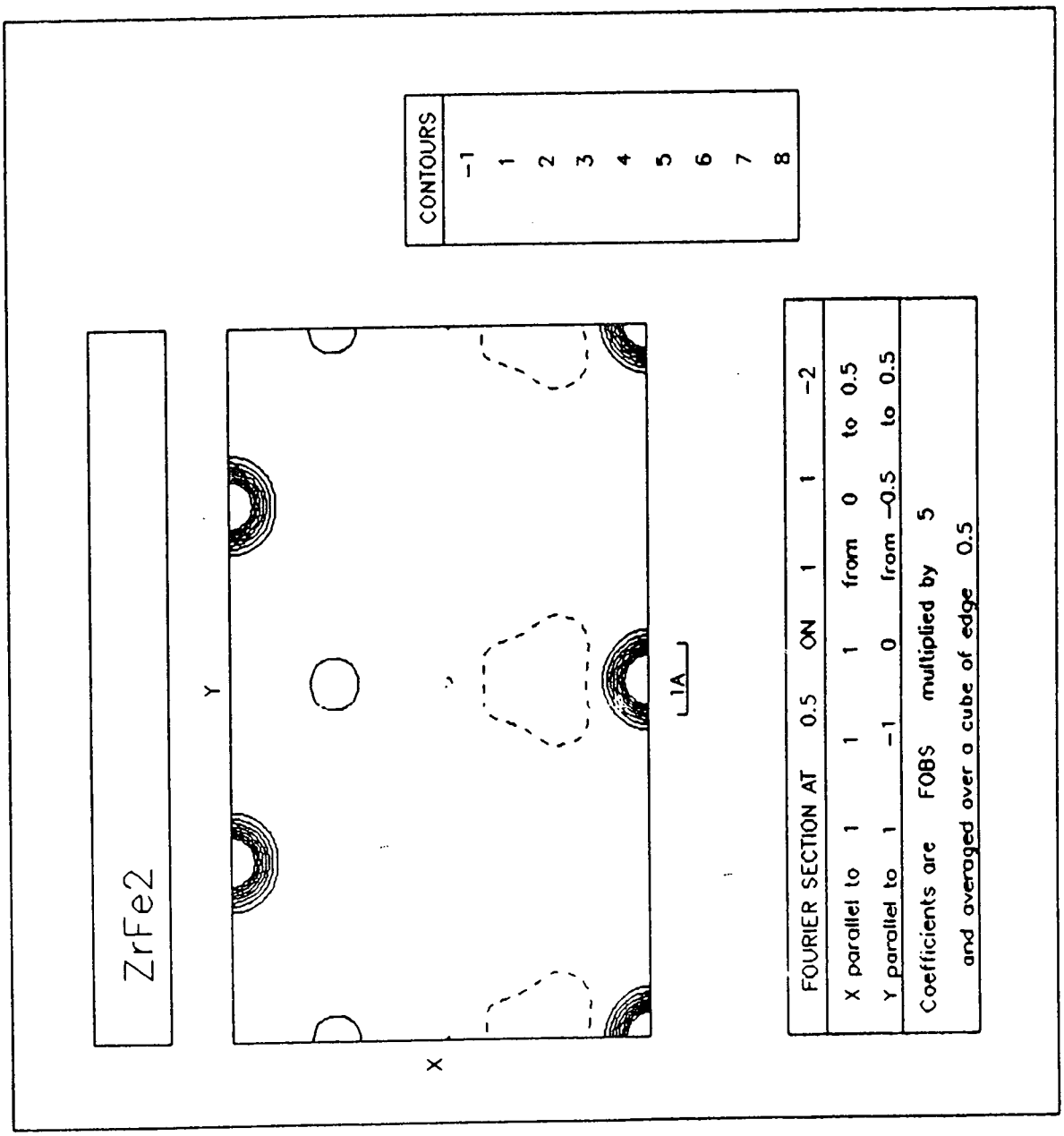
ZrFe2
Y
X
1A
CONTOURS
-1
1
2
3
4
5
6
7
8
FOURIER SECTION AT 0.5 ON 1 1 -2
X parallel to 1 1 1 from 0 to 0.5
Y parallel to 1 -1 0 from -0.5 to 0.5
Coefficients are FOBS multiplied by 5
and averaged over a cube of edge 0.5

Figure 7.8 The experimental and theoretical form factors for Fe. The solid line represents the free Fe^{2+} form factor with a magnetic moment of $1.63\mu_B$/Fe atom. The most striking feature is how closely the two match, there is no obvious contraction or expansion of the Fe magnetisation in reciprocal or real space.

Figure 7.8

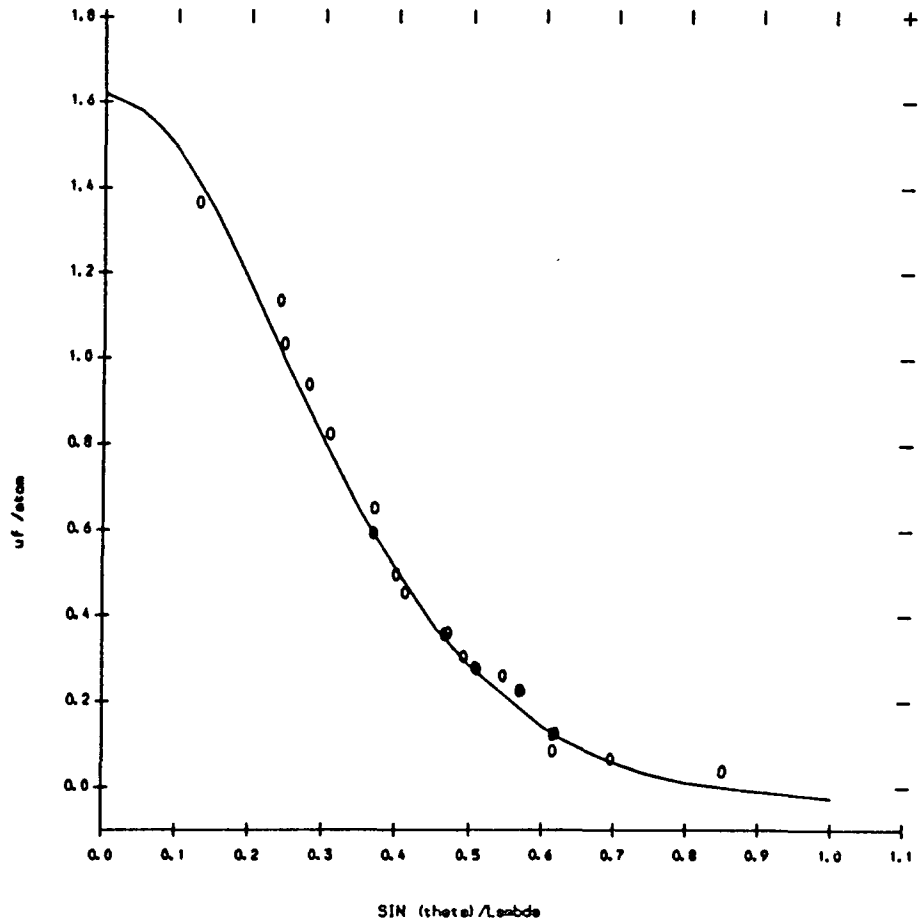
1.8
1.6
1.4
1.2
1.0
0.8
0.6
0.4
0.2
0.0
uf /atom
0.0
0.1
0.2
0.3
0.4
0.5
0.6
0.7
0.8
0.9
1.0
1.1
SIN (theta) /Lambda

CHAPTER 8

Spin Density Fluctuations in MnSi Under Pressure

8.1 Introduction

The material MnSi has been the focus of a great deal of investigation[87,88,89,90]. It exhibits a helical spin density wave below a transition temperature at ≅29K (wavelength = 0.035(5)$Å^{-1}$), ordering ferromagnetically in a small external magnetic field (6KGauss) with a moment of $0.4\mu_B$/Mn atom, with the characteristic behaviour of itinerant ferromagnets: not fully saturating in fields as high as 150 KGauss; above T_c, in the paramagnetic phase, the bulk magnetic susceptibility follows the Curie-Weiss form[92,93,94]. The theoretical ordering temperature is renormalised due to spin fluctuations by an order of magnitude over that predicted by the Stoner picture. The electron mass is higher by a factor of 5 over the band mass and MnSi is often viewed as an intermediate between the typically weak metal ferromagnets (eg. Ni_3Al[22], $ZrZn_2$[2]) and the heavy fermion systems (eg. UPt_3[95]).

8.1 Collective Fluctuations in MnSi

This chapter describes briefly an experimental investigation of collective fluctuations in MnSi using the small angle neutron

spectrometer D11 at the ILL. Using the description detailed in chapter 2 the fundamental collective modes in MnSi can be described using the microscopic parameters a,b,c and γ above T_c. The work was designed to follow the change in c and γ with variation in pressure following work showing[96] that the application of a hydrostatic pressure reduces the transition temperature falling to 0 Kelvin at a pressure of 15Kbar.

A pressure cell using an organic pressure medium (fluorinert) was loaded with a polycrystalline specimen of MnSi, a pressure applied, then introduced into the cryostat (see figure 2.1). A sample detector distance of 2.5m was set with an incident neutron wavelength of 7Å to be beyond the Bragg cut off and at the same time to keep the flux high (flux peak at 6.5Å). Unfortunately scattering from the pressure medium in the low q region probed by D11 proved to be larger than the expected intensities from scattering owing to the MnSi response. This background could not be systematically deducted from the total scattering response owing to its high temperature dependency and hysteretic nature. These difficulties have been associated with changes in the pressure cell medium causing specimen motion and anomalous low q scattering. This was the first time the cell had been used on the small angle scattering instrument, any subsequent work requiring the use of an alternative pressure medium. No alternative was available so study of the position of scattering from the helix in q space as a function of hydrostatic pressure became the primary interest.

8.2 Observation of Helical Spin Density Waves

A limited number of spectra were obtained below T_c with no evidence of a change of the helix in spatial extent (±0.007Å in q) between scans taken with hydrostatic pressures of 0 and 8.5 Kbar. At 10K a spiral peak has benn observed centrerd at q_{el}= 0.036(3)Å.

8.3 Conclusions

The use of the supplied standard pressure cell is not advised for future temperature dependant work.

This work was the first of its type and has lead to further work using triple axis spectrometer at the ILL where the elastically scattered neutrons from the pressure cell can be eliminated by energy analysis. This has been documented in reference 91.

Figure 8.1 Intensity data for scattering from the helical spin density waves of MnSi collected on the small angle scattering spectrometer D11 normalised to a monitor count of 1000. (a) The helical spin density wave at q=0.036(3)Å observed at 10K under a hydrostatic pressure of 400 bar. (b) a second spectra taken at 10K under 400 bar. The helix peak is obscured by anomalous low q scattering from the pressure cell medium. (c) a background scan taken with an empty pressure cell at 200K, 0 bar.

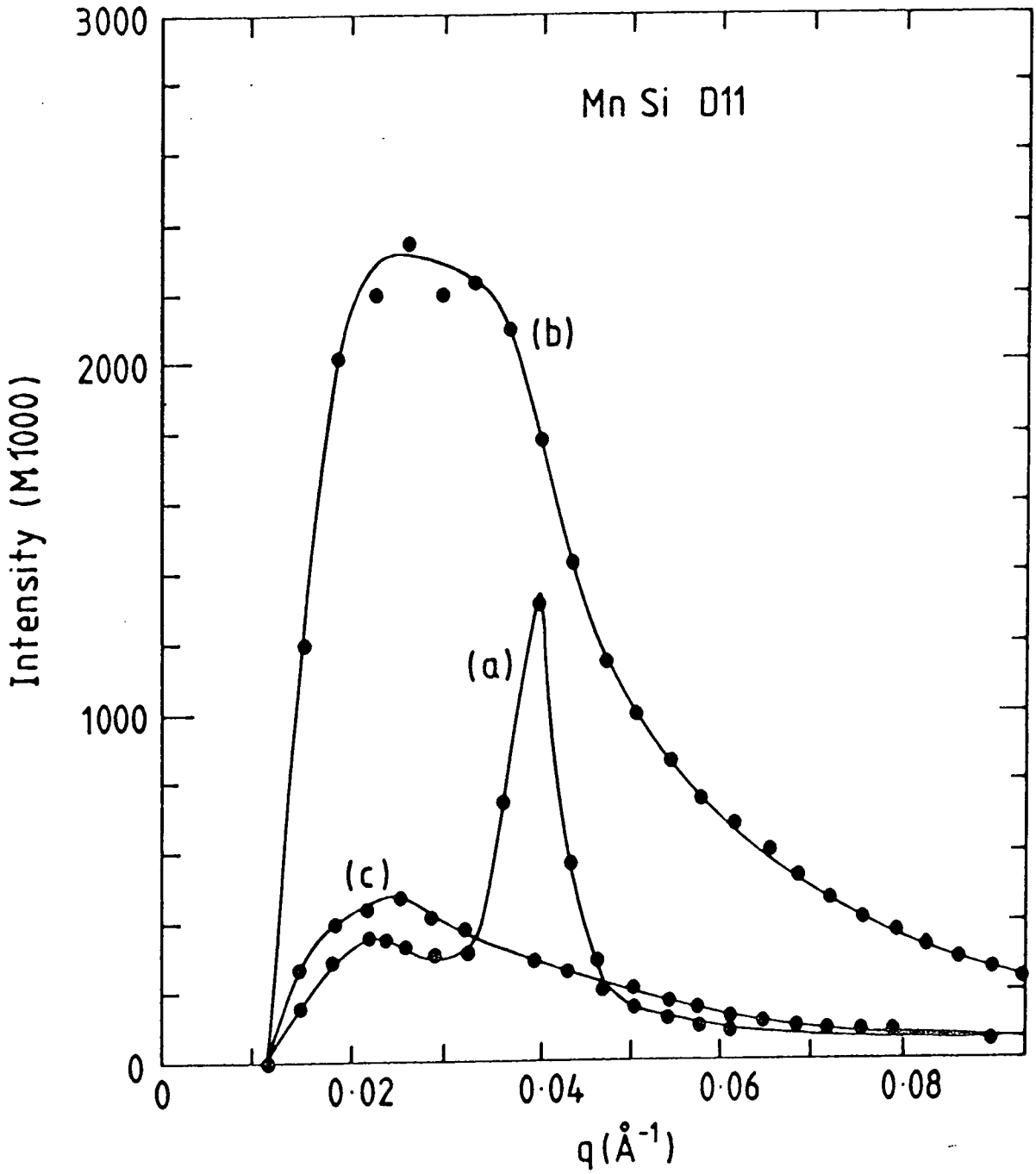
Mn Si D11
Intensity (M1000)
3000
2000
1000
0
0
0·02
0·04
0·06
0·08
q(Å⁻¹)
(a)
(b)
(c)

Figure 8.1

References

1 Bloch F. 1929 Z. Physiks 57, 545

2 Matthais B.T., Bozoth R.M., 1958 Phys. Rev. 100, 604

3 Matthias B.T., Clogston A.M., Williams H.J., Corenzwit E., Sherwood R.C., 1961 Phys. Rev. Lett. 7,7

4 Horwitz G, Callen H, 1961 Phys. Rev. 124,1757

5 Van Vleck J.H., 1953 Review of Modern Physics 25,220

6 Stoner E.C., 1938 Proc. Royal Soc. A165,372

7 Slater J.C., 1936 Phys. Rev. 49,537,931

9 Bloch F, 1930 Z. Physiks 61,206

10 Wigner E., 1934 Phys. Rev. 46,1002

11 Slater J.C., 1937 Phys. Rev. 52,198

12 Herring C., Kittel C., 1951 Phys. Rev. 81,869

13 Herring C., 1952 Phys. Rev. 87,60

14 Murata K.K., Donaich S., 1972 Phys. Rev. Lett. 29,285

15 Moriya T., Kawabata A., 1973 J. Phys. Soc. Japan 34,639

16 Lonzarich G.G., Taillefer L., 1985 J. Physics C18,4339

17 Lindley E.J., Mayers J., 1988 Neutron Scattering at a pulsed Source, Ed. Newport R.J., Rainford B.D., Cywinski R., IOP Publishing Ltd.

18 Lovesey S., 1984 The Theory of Neutron Scattering from Condensed Matter, Oxford University Press

19 White R.M., 1982 Quantum Theory of Magnetism, Springer Verlag

20 Izuyama T., Kim D.J., Kubo R., 1963 J. Phys. Soc. Japan 18,1025

21 Watson R.E., Freeman A.J., 1961 Acta. Cryst. 14,27

22 Bernhoeft N.R., Cole I., Lonzarich G.G., Squires G.L. 1982 J. Appl. Physics 53,8204

23 Bernhoeft N.R., Lonzarich G.G., Mitchell P.W., McKPaul D., 1983 Phys. Rev. B 28,422

24 Bernhoeft N.R., 1986 Physica 136B,443

25 Ishikawa Y., Noda Y., Fincher C., Shirane G., 1982 Phys. Rev. B 25,254

26 Hayden S.M., Lonzarich G.G., McKPaul D, Lindley E., 1989 Phys. Rev. Lett. 62,657

27 Moriya T., 1979 J. Magnetism & Mag. Mat. 14,1

28 Law S.A., 1987 Phd thesis for the University of Cambridge

29 Lingard P.A., 1983 Phys. Rev. Lett 50,No.9,690, 1983 Phys. Rev. B. 27,2980

30 Forster D., 1975 Hydrodynamic Fluctuations, Broken Symmetry and Correlation Functions, W.A. Benjamin.

31 Pfann W.G., 1959 Zone Refining, John Wiley and Sons Inc.

32 Bridgeman P.W., 1925 Proc. Amer. Acad. Arts. Sci. 60,305

33 Czochralski J, 1918 Z. Phys. Chem 92,219

34 Shar J.S., Crystal Growth ed. PAmplin B.R., Oxford Pergamon Press.

35 Sakakibara T., Mollymoto H., Muneyuki D., 1982 J. Phys. Soc. Jap. 51,No8,2439

36 Taillefer L. 1984, Spin fluctuations in Itinerant Electron Ferromagnets, Dissertation, University of Cambridge

37 Wohlfarth E.P.,1968 J. Appl. Phys.39,1061, 1977 J. Mag. Mag. Mat. 20,1980

38 Hoon S., Wilcock S, 1988 J. Phys. E 21,772

39 Lambrick D.B., 1985 Phd thesis, University of Durham

40 Enz C.P., Matthias B.T., 1978 Science 101,828

41 Saji H., Yamada T., Asanuma M., 1966 J. Phys. Japan 21,255

42 Matthais B.T., Giorgi A.L., Shuebing V.O., Smith J.L., 1978 Phys. Lett. 69A,No. 3,455

43 Rakhaecha U.C., Felcher G.P., Sinha S.K., Smith J.L., Matthais B.T., 1980 Solid State Comm. 33,495

44 Stewart G.R., Matthais B.T., Giorgi A.L., Szklarz E.G., Smith G.L., 1979 Solid State Comm. 30,709

45 Monod P., Felner I., Chauteau G., Shalteil D, 1980 J. Physique Lettres 41,2511

46 Beal T., Monod P., 1980,1981

47 Acker F., Hunguein R., Smith J.L., Heuang C.Y., 1982 J. Mag. Mag. Mat. 22,250

48 Acker F. Unpublished

49 Giorgi A.L., Matthias B.T., Stewart G.R., Acker F., Smith J.L., 1979 Solid State Comm. 32,455

50 Bloch D., Edwards D., Shimuzu M., Voiran J., 1975 J. Phys. F 5,1217

51 Gratz E., Sechovsky V., Wolfarth P., Kirchmay H.R., J. Phys. F 10,1980

52 Felcher G.P., Cable J.W., Smith J.L., 1980 Phys. Rev. Lett. 45,No. 9,751

53 McKPaul D., Warren P., Bernhoeft N.R., Unpublished

54 McKPaul. D, Moze O., Cornelius C.A., Giorgi A.L. 1984 J. Mag. Mag. Mat., 42,201

55 Moriya T., 1985 Spin Fluctuations In Itinerant Electron Magnetism, Springer Verlag

56 Bacon G.E., 1962 Neutron Diffration, Oxford University Press

57 Halpern O., Johnson M.H., 1939 Ibid 55,898

58 Lovesey S., 1984 The Theory of Neutron Scattering, Oxford University Press, Chapter 10

59 Nathans R., Shull C.G., Shirane G., Andresen A., 1959 J. Phys. Chem. Solids 10,138

60 Mezei F., 1972 Z. Physik 255,146

61 Majorana E., 1932 Nuovo Cimento 9,43

62 Brown P.J., Matthewman J.C., Cambridge Crystallographic Subroutine Library Users Manual Mark 3, May 1987

63 Forsyth J.B., 1978 N.A.T.O. Advanced Study Institute Series B Physics, page 48

64 Brown P.J., Forsyth J.B., 1964 Brit. J. Appl. Phys. 15,1529

66 Darwin C.G., 1923 Phil. Mag. 43,800

67 Becker P., Coppens P, 1974 Acta Cryst. A30,129

68 Matthewman J.C., Extension to the C.S.S.L. ref:62

69 Neutron Diffraction ed. Dachs H., Springer Verlag 1978 Article by Hayter J.B., Prandl W.

70 Busing W.R., Levey H.A., 1967 Acta Cryst. 22,457

71 Moon R.M., Koecher W.C., Shull G.C., 1975 Nucl. Inst. Meth. 129,515

72 Moon R.M., Koehler W.C., Cable J.W., 1976 Proc. Conf. Neutron Scattering, Gatlinburg, USA.

73 Brüchner W, Kleinstück K, Schulze G.E.R., 1967 Phys Stat Solidi 23,475

74 Brüchner W., Perthel R., Kleinstück K., Schulze G.E.R. 1968 Phys Stat. Solidi. 29,211

75 Kai K, Nakamichi T., Yamamoto M., 1968 J. Phys. Soc. Japan 25,1192

76 Peigger E., Craig R.S., 1963 J. Chem. Phys. 39,137

77 Kocher C.W., Brown P.J., 1962 J. Appl. Phys. Suppl. 33,1091

78 Klien B.M., Pickett W.E., Papaconstantopoulos D.A., Boyer L.L., 1983 Phys. Rev. B. 27,No. 11,6721

79 Williams A.R., Gregory A.R., Schweizer K., 1981 J. Mag. Mag. Mat 15,293

80 Yamada H., Shimuza M., 1986 J. Phys. F 16,1039

81 Mohn P., Schwarz K., 1985 Physica 130B,26

82 Dumelow T., Reidi P.C., Mohn P., Schwarz K., Yamada H., 1986 J. Mag. Mag. Mat. 54-57,1081

83 Armatage J.G.M., Dumelow T., Mitchell R.H., Reidi P.C., Abell J., Mohn P., Schwarz K., 1986 J. Phys. F 16,No. 7,L141

84 Slater J.C., Koster G.F., 1954 Phys. Rev. 94,1498

85 Givord D., Gregory A.R., Schweizer J., 1980 J. Mag. Mag. Mat. Vol 15-18, Pt 1, 293 293

86 Clementi, Roetti 1974 J. Chem. Phys. 61(5),1062

87 Shirane G., 1983 Phys. Rev. B 28,6251

88 Matsunaga M. et. al., 1982 J. Phys. Soc. Jap. 51,1153

89 Kuaka S. et. al., 1976 Solid State Comm. 20,925

90 Ishikawa Y., Arai M., 1984 J. Phys. Soc. Jap. 53,2726

91 Brown S.A., 1990 Itinerant Magnetism in MnSi, Phd Thesis University of Cambridge

92 Wernick M.B. et. al., 1972 Mat. Res. Bull. 7,1431

93 Bloch D. et. al., 1975 Phys. Lett. A51,259

94 Ishikawa Y. et. al., 1976 Solid State Comm. 19,525

95 Taillefer L., Phd Thesis University of Cambridge

96 Muroka Y., Shigu M., Nakamura Y., 1979 J. Phys. F 9,No. 9., 1889

Appendix A

Undamped Spin Wave Cross-Section

The cross section per atom integrated over the energy for unpolarised neutrons may be written:

$$\frac{d\sigma}{d\Omega} = 4\sigma_0 \frac{(n^{\uparrow}-n_{\downarrow})}{2} \frac{4}{3} \left[\sum_{j=1}^{2} \frac{k}{k'} (\omega_j)\, n(\hbar\omega) |J|_{\omega_j} + \sum_{l=1}^{2} \frac{k}{k'} (n(\hbar\omega_l+1) |J|_{\omega_l} \right]$$

Where $(n^{\uparrow}-n_{\downarrow})$ is the temperature dependent difference in the number of up and down spins per atom and $|J|$ is the Jacobian of integration. The energy of interaction $\hbar\omega_j$, $\hbar\omega_l$ for a quadratic spin wave spectrum with stiffness D and energy gap E_g when observing at an angle θ between the incident and scattered neutron wavevectors may be calculated by considering energy and momentum conservation.

$$\frac{\hbar^2}{2m} (k^2-k'^2) = Dq^2 + E_g \qquad : \qquad k'-k = q$$

which gives

$$\frac{k'}{k} = \frac{\cos\theta \mp \sqrt{\sin^2\theta_c - \sin^2\theta - \frac{E_g}{Ei} \sin\theta_c (1+\sin\theta_c)}}{1 + \sin\theta_c} = \alpha_l^{\pm}$$

$$\frac{k'}{k} = \frac{\cos\theta \mp \sqrt{\sin^2\theta_c - \sin^2\theta - \frac{E_g}{E_i}\sin\theta_c(1-\sin\theta_c)}}{1 - \sin\theta_c} = \alpha_g^{\pm}$$

for neutron energy loss (l) and gain (g) events. $\sin\theta_c = \hbar^2/2mD$ and $E_i = \hbar^2k^2/2m$. When the terms inside the square roots go to zero the critical angle ϕ beyond which there is no spin wave scattering is reached.

The Jacobians of integration can be shown to be:

$$|J_l^{\pm}| = \left| -1 + \frac{1}{\sin\theta_c}\left(-1 + \frac{\cos\theta}{\alpha_l^{\pm}} \right) \right|^{-1}$$

$$|J_g^{\pm}| = \left| 1 + \frac{1}{\sin\theta_c}\left(-1 + \frac{\cos\theta}{\alpha_g^{\pm}} \right) \right|^{-1}$$

and the energy transfers are

$$\hbar\omega = E_i\ (1-\alpha_l^{\pm})$$
$$\hbar\omega = -E_i\ (1-\alpha_g^{\pm})$$

If the Jacobians of integration are approximated to lowest order by:

$$|J| = |J_{l/g}^{\pm}| = \left(1 - (\theta/\theta_c)^2 \right)^{1/2}$$

the population factors for neutron energy gain and loss are set

equal to their high temperature limit and k' set equal to k; then, summing over energy gain and loss:

$$\frac{d\sigma}{d\Omega} = 2\sigma_0(n^{\uparrow}-n_{\downarrow})\,\frac{4}{3}\,\frac{k_B T}{D|J|}\left[\frac{1}{q_1^2} + \frac{1}{q_2^2}\right]$$

to solve for $\left[\frac{1}{q_1^2}+\frac{1}{q_2^2}\right]$ at energy transfers $\hbar\omega/E_i \ll 1$ and angles $\theta < 5^0$ then use:

$$q^2 = k^2\left[\theta^2 + \left(\frac{\hbar\omega}{2E_i}\right)^2\right]$$

q_1 and q_2 are given by the simultaneous solution of this equation with $\hbar\omega = Dq^2$ giving

$$\frac{D^2q^4}{4E_i^2} - \frac{q^2}{k^2} + \theta^2 = 0$$

hence $$\frac{q_1^2 + q_2^2}{q_1^2 q_2^2} = \frac{1}{k^2\theta^2} = \frac{1}{q_0^2}$$

where q_0 is the magnitude of the elastic scattering wavevector. The cross-section (quasistatic) thus depends only only one parameter (D) at temperature T.

$$\frac{d\sigma}{d\Omega} = 2\sigma_0(n^{\uparrow}-n_{\downarrow})\,\frac{4}{3}\,\frac{k_B T}{D|J|}\,\frac{1}{q_0^2}$$

Appendix B

A classical derivation of the two pole damped model of spin waves. When considering damped oscillating magnetisation density fluctuations care must be taken in setting up the initial equations to be symmetric in the components $\{m_x, m_y\}$ of the vector. This is to be contrasted with the simple damped harmonic oscillator model[18] which is a scalar model. Considering the simple classical case:

Consider two variables x and y. x decays and feed into variable y and decays into the heat bath and visa a versa.

$$\frac{dx}{dt} = \omega_1 y - \gamma_1 x$$

$$\frac{dy}{dt} = -\omega_2 x - \gamma_2 y$$

from which

$$\frac{d^2x}{dt^2} = \omega_1 \frac{dy}{dt} - \gamma_1 \frac{dx}{dt}$$

$$= \omega_1(-\omega_2 x - \gamma_2 y) - \gamma_1 \frac{dx}{dt}$$

$$= -\omega_1\omega_2 x - \gamma_2(\gamma_1 + \gamma_2)\frac{dx}{dt} - \gamma_1\gamma_2 x$$

or

$$0 = \frac{d^2x}{dt^2} + (\gamma_1 + \gamma_2)\frac{dx}{dt} + (\omega_1\omega_2 + \gamma_1\gamma_2)x$$

if symmetric then $\omega_1 = \omega_2 = \omega_0$ and $\gamma_1 = \gamma_2 = \gamma$ a solution to this equation is $x = Ae^{-\gamma t}\cos(\omega_o t+\phi)$.

Creating the correlation function

$S(t) = \langle x(t)x(0)\rangle$ it can easily be shown that

$$S(t) = \frac{\langle A^2\rangle}{2} e^{-\gamma t}\cos\omega_0 t$$

and forming a one sided Laplace transform, since the Fourier transform of primary interest to neutron scattering goes to zero: $\tilde{S}(z) = \int_0^\infty dt\, e^{izt} S(t)$ and $S(\omega) = 2 \text{ Re } \tilde{S}(t)$.

if $z= \omega +i\epsilon$ then

$$\text{Re } \tilde{S}(z) = \text{constant} \left[\frac{\gamma+\epsilon}{(\omega+\omega_0)^2+(\gamma+\epsilon)^2} + \frac{\gamma+\epsilon}{(\omega-\omega_0)^2+(\gamma+\epsilon)^2} \right]$$

now $\epsilon=0$ then

$$S(\omega) = \text{constant} \left[\frac{\gamma}{(\omega+\omega_0)^2+ \gamma^2} + \frac{\gamma}{(\omega-\omega_0)^2+ \gamma^2} \right]$$

this contrasts to the damped harmonic oscillator solution

$$S(\omega) = \text{constant} \left[\frac{\gamma\omega_0^2}{(\omega^2-\omega_0^2)^2 + \omega^2\gamma^2} \right]$$

(see reference 18 appendix B).

Appendix C

If I is the peak intensity then the statistical Chi-Square and R factors are defined for observed data (obs) and predicted data (calc) by:

$$X^2 = [\sum_i w_i(I_i(obs)-I_i(calc))^2] /(N-P-C)$$

Where w_i is the weighted factor equal to $1/\sigma_i^2$ for observation i, N is the number of observations, P is the number of variables and C is the number of constraints. The R factors are defined through:

$$R = \frac{\sum_i |I_i(obs)-I_i(calc)|}{\sum_i I_i(obs)}$$

$$R_w = \left[\frac{\sum_i w_i |I_i(obs) - I_i(calc)}{\sum_i w_i I_i^2(obs)} \right]^{1/2}$$